Optical and Microwave Beamforming for Phased Array Antennas

by

Mohammad Fakharzadeh Jahromi

A thesis
presented to the University of Waterloo
in fulfillment of the
thesis requirement for the degree of
Doctor of Philosophy
in
Electrical and Computer Engineering

Waterloo, Ontario, Canada, 2008

I hereby declare that I am the sole author of this thesis. This is a true copy of the thesis, including any required final revisions, as accepted by my examiners.

I understand that my thesis may be made electronically available to the public.

Abstract

Phased array antenna has been used for a variety of military and civil applications, over the past five decades. Being structurally conformal and flexible, phased array antenna is highly suitable for mobile applications. Besides, it can form the agile or shaped beams required for interference cancellation or multifunction systems. Moreover, the spatial power combination property increases the effective radiated power of a transmitter phased array system. Similarly, in a receiver phased array, beamforming increases the signal to noise ratio by coherent integration of the desired signals.

Despite its impressive potentials and properties, phased array antenna has not become a commercial product yet. Cost and complexity of phased array antenna are beyond the scales of consumer electronics devices. Furthermore, calibration is an essential requirement of such a complex system, which is a fairly time-consuming process and requires skilled man power. Moreover, the narrow bandwidth of microwave components degrades the broadband performance of phased array system. Finally, the majority of the beamforming algorithms developed so far have preconditions, which make them unsuitable for a low-cost system.

The objective of this thesis is to provide a novel cost-effective solution to minimize the system complexity of the future intelligent antenna systems, *without* sacrificing the performance. This research demonstrates that a powerful, robust beamforming algorithm, integrated in an efficient single-receiver architecture, constitutes the essence of a low-cost phased array antenna. Thus, a novel beamforming technique, called *Zero-knowledge* algorithm is developed. It is investigated, both theoretically and experimentally, that the proposed algorithm can compensate for the hardware errors and imperfections of the low-cost components of the system.

Zero-knowledge beamforming algorithm possesses significant properties. Neither *a priori* knowledge of the incoming signal direction, nor the exact characteristics of the phase control network are required in this method. Proper adjustment of the parameters, makes this algorithm appropriate for mobile systems, particularly those installed on vehicles. The algorithm alleviates the drawbacks of analog phase shifters, such as imbalanced insertion loss and fabrication tolerances. Furthermore, this algorithm can serve as the core of a direction-of-arrival estimation technique, which senses the minor deflections of the array heading.

For broadband applications optical delay lines must be used in the phase control network of the phased array systems, which are costly. Nevertheless, employing

miniaturized delay lines can significantly reduce the device area, and consequently, the fabrication cost. Thus, in this research four types of miniaturized optical delay lines, designed in slow-wave structures, are analyzed, which can provide a large delay per length. In addition, two novel optical beamforming techniques, based upon the properties of Zero-knowledge algorithm, are developed for transmitter and receiver phased arrays.

Acknowledgements

I would like to express my profound gratitude to my supervisors Prof. S. Safavi-Naeini, and Prof. Sujeet K. Chaudhuri, for their invaluable assistance, brilliant ideas and constructive comments. My sincere thanks to Prof. Raj Mittra (Pennsylvania State University) for accepting to be the external examiner of the defence session and reading this dissertation. I am thankful to the committee members Prof. O.M. Ramahi, Prof. R.R. Mansour, and Prof. Jim Martin (Department of Physics and Astronomy).

I am especially grateful to Prof. S.H. Jamali for his great personality and the insightful discussions on beamforming. I would like to acknowledge Prof. O.M. Ramahi for his encouragements and illuminating suggestions.

Over the past 3 years, I had delightful moments with my colleagues at Intelwaves company: Dr. Pedram Mousavi (CEO), who managed the Ku-band phased array project, and Dr. Kiarash Narimani, Dr. G.R. Rafi, Mirca Hossu, and David Bitsy who helped me with the experimental set-up of this research. Furthermore, I am thankful to Prof. H.A. Abiri, who introduced the phased array concept to me for the first time when I was an undergraduate student at Shiraz University in 1999. My supervisor at Sharif University of Technology, Prof. M.M. Nayebi provided a unique opportunity for me to study phased array systems. I appreciate his support and earnest friendship. I never forget the late Prof. Kasra Barkeshli from whom I learned many things in the area of Electromagnetics and Scattering Theory, at Sharif University of Tech. I am appreciative of Dr. Laleh Behjat (University of Calgary) who helped me with the optimization toolboxes.

Special thanks to my best friends and roommates (for more than two years) Dr. Masoud Ebrahimi and Dr. Amin Mobasher. I am thankful to my former and current officemates, Dr. Daryoosh Saeedkia, Mohammad Neshat and Mehrbod Mohajer, and other members of our wonderful group at the *Intelligent Integrated Photonics and Radio Lab*, University of Waterloo.

I wish to express my love and gratitude to my beloved family: my dear wife, my kind sister and my lovely mother, the three guardian angels!

Dedication

I wish to dedicate this dissertation

to my beloved wife, *Marzieh*,

to my devoted mother,

and to the enduring memory of my father.

Contents

List of Tables

List of Figures

List of Abbreviations

ADC	Analog to Digital Convertor
AWGN	Additive White Gaussian Noise
BER	Bit Error Rate
CDMA	Code Division Multiple Access
CMOS	Complementary Metal-Oxide Semiconductor
DAC	Digital to Analog Convertor
DOA	Direction of Arrival
DRR	Double Ring Resonator
DVB	Digital Video Broadcasting
EIRP	Effective Isotropic Radiated Power
FDTD	Finite Difference Time Domain
FIR	Finite Impulse Response
HPBW	Half Power Beam-Width
IF	Intermediate Frequency
IL	Insertion Loss
LHCP	Left Hand Circular Polarization
LMS	Least Mean Square
LNA	Low Noise Amplifier
LO	Local Oscillator
LOS	Line Of Sight
MEMS	Micro-electromechanical systems
MMW	Milli-Meter Wave
NF	Noise Figure
NLOS	Non-Line Of Sight
ODL	Optical Delay Line
PAA	Phased Array Antenna
PC	Photonic Crystal
PDF	Probability Density Function
PRR	Parallel Ring Resonator
RF	Radio Frequency
RSL	Reflective Spiral Line
RTPS	Reflective-Type Phase Shifter
SNR	Signal to Noise Ratio
TO	Thermo Optic
WPAN	Wireless Personal Area Network

Chapter 1

Introduction

Make everything as simple as possible, but not simpler!
Albert Einstein

Phased array antenna has been used for a variety of military and civil applications [1]– [2], such as satellite communications [3]– [4], wireless communication [5]– [6], imaging [7], meteorology [8], radio astronomy [9], target tracking and surveillance [10]– [12], over the past five decades.

Wherever the size or rigidity of the conventional antennas constrains the performance of radio systems, phased array antenna opens a new door. For example, for mobile satellite communications, which is a suitable application for this thesis, bulky reflector (dish) antennas cannot be installed on the roof of small-size or even mid-size vehicles due to their high aerodynamic drag [13]– [14]. On the other hand, a low profile, conformal phased array antenna can be easily installed on the vehicle without violating the vehicle aerodynamic specifications. Moreover, with a phased array antenna the satellite tracking can be performed faster and the quality of reception could be higher compared to a conventional dish antenna.

when an agile or shaped antenna beam is required, phased array is the ultimate solution [2]. The performance of the current wireless networks, CDMA cellular network for example [5], is limited by interference not noise. There are numerous hardware or software solutions to null single or multiple interferers with phased array antenna or so called *smart antenna*. An efficient beamforming algorithm potentially can insert N-1 nulls in the radiation pattern of an N-element phased array. Performing multiple functions simultaneously or based on time-sharing is another significant property of phased array which has been utilized for radar and aerospace applications for a long time [15].

Recently the interest in wireless Milli-Meter Wave (MMW) networks for indoor multi-Gb/s communication has dramatically increased [16]– [21]. The 60GHz frequency band has been released and proposed for short-range wireless applications such as Wireless Personal Area Network (WPAN) [22]– [23], and wireless multimedia or High-Definition (HD) streaming. IEEE task group 3c (TG3c) is working on standardization of this frequency band for WPAN applications. Simultaneously, wireless HD Consortium is defining a wireless protocol to create a 60GHz wireless video network for consumer electronic audio and video devices [24]. However, severe path loss and shadowing loss in this frequency band is the first hurdle to overcome.

Moreover, the fundamental limits of semiconductor technology in increasing the gain and output power of amplifiers have constrained the effective radiated power of the transmitters. Consequently, the Signal to Noise Ratio (SNR) received by a single antenna topology cannot meet the Bit-Error-Rate (BER) requirements of the communication networks. Fortunately, the integration of phased array antennas at both transmit and receive nodes of a MMW network can increase the effective radiated power and antenna gain, and the possibility of non-line of sight reception in case of shadowing. So the joy of phased arrays will continue.

1.1 Drawbacks of Current Phased Arrays

Despite these impressive potentials and properties, phased array antenna is not a commercial product yet. Cost and complexity of phased array antenna have been beyond the scales of consumer electronics devices. The other challenge is calibration, which is an essential requirement of such a complex system. Calibration takes time and requires the skilled man power. Moreover, the narrow bandwidth of multiple microwave components in a phased array systems degrades the broadband performance of the system. Finally, the beamforming algorithms developed so far must be modified or revised to be compatible with a low-cost phased array.

1.1.1 Cost and Complexity

Phased array system is known to be an expensive product. In radar applications high energy losses of passive phased array antenna resulted in increasing the output power and consequently the transmitter volume and power dissipation [25]. Gradually solid-state active phase array antennas became the center of attention, for their lower weight and power dissipation, and higher output power and reliability. However in 1980's the actual cost of phased array system was far beyond the optimistic estimations [26]. Consequently, the huge fabrication cost slowed the growth in phased array technology.

Recent advances in solid-state technology and transistor scaling have made the dream of a low-cost fully integrated phased array a reality [27]. Several demonstrations of phased array on silicon have been reported [28]– [30]; however, questions regarding the antenna type, beamforming algorithm and calibration are left unanswered. Low output power and amplification gain are two major challenges of the current Complementary MetalOxide Semiconductor (CMOS) and Silicon-Germanium (SiGe) technologies at MMW-band.

1.1.2 Calibration and Fabrication Errors

Sensitivity of the beamforming algorithm and beam control unit to the system model forces a calibration process, which is a laborious and time consuming task . Particularly if the antenna is in service, calibration imposes an unacceptable overhead on the system [31].

1.1.3 Bandwidth

A major bottleneck in designing a broadband phased array system is the narrow-band characteristics of the conventional phase shifters. Hence, as the microwave carrier frequency varies, the main beam deviates from the desired direction (beam-squint see Chapter 2). As a result, designing multi-band or wide-band phased arrays requires a complex feed and distribution network. Another disadvantage of current phase shifters is their imbalanced insertion loss, which means the amplitude response of the phase shifter (and consequently the beamforming network) varies with phase-shift adjustment [32]. The ultimate solution is to use true-time delay lines to generate time-delay instead of phase shift [33]. Moreover, to steer the antenna beam, tunability of the delay line is mandatory. A continuous delay line is preferred to steer the beam to any direction within the coverage region accurately. Nevertheless, the Optical Delay Lines (ODL) developed so far are bulky, lossy and require complex switching networks [34]– [35].

1.1.4 Beamforming

An effective beamforming algorithm is necessary to exploit the phased array potentials. A substantial body of research has been devoted to phased array beamforming; however, efficient and low-complex algorithms are still needed to lower the cost of phased arrays for commercial applications. An efficient beamforming algorithm, as will be discussed in Chapter 2 and 5, is the one which compensates for the hardware inaccuracies, does not add to complexity of the system significantly, converges fast and reduces the steady state error.

When sufficient information of the source (target) and array is available there are optimum methods to find the array weights which minimize the least mean square error of the received signal [36]. Such methods are based on inverting the covariance (correlation) matrix of the received array signals. To find this matrix one must have access to all received signals (in base-band). Thus, for each element an individual receiver (mixer, IF, decoder, analog to digital converter (ADC), etc.) is required [37]. Furthermore, a reference signal is required to estimate the error.

Assuming that the received array signal and noise are jointly ergodic processes, the array covariance matrix can be estimated based on calculating the time average of the received signals, which is a time consuming process. Adaptive beamforming methods have been used for beamforming to overcome some of these challenges [38]– [39]. Nevertheless, the optimum or adaptive beamforming algorithms developed so far have at least one of the following drawbacks:

1. Measuring signal covariance matrix is costly, because N-channel receivers are required. Estimating this matrix is time consuming and sometimes inaccurate [40, 41].

2. If Direction of Arrival (DOA) of the desired signal is not known or accurately estimated, calibration errors will degrade the beamforming performance seriously [42]. DOA estimation methods such as MUSIC [43] and ESPRIT [44] are complex, lengthy, and sensitive to modeling errors [45]– [46].

3. The phase-voltage characteristics of the phase shifters are not deterministic. They are device-dependent and may change with the environmental conditions such as humidity and temperature [47] – [49]. The situation is worsened if one considers the cable and connector induced errors.

4. Platform motions affect the estimated covariance significantly. Even a small relative displacement of the source during the time required for covariance estimation causes a significant error and gain drop [50].

When one combined signal from all antennas is the only available information (single-receiver array), beamforming problem becomes even more complicated.

1.2 Objectives of This Research

In this section a brief review of the current status of the low-cost phased array systems is presented, and the main objective of this research is explained.

1.2.1 Toward Low-cost Phased Arrays

A number of techniques have been proposed to make phased arrays more affordable [51]– [56]. In [51] a simple 2-bit phase shifter has been used for beam-switching which significantly restricts the beamforming capability of the system. The two configurations proposed in [53] use lens antenna and an external horn, thus they are bulky and still costly. The low-cost array introduced in [52] is an application specific

system, which receives the Global Positioning System (GPS) satellite signals. The information provided by GPS satellite is an asset to tracking and beamforming. Moreover, the beamforming algorithm relies on accurate phase shifter characteristics. Thus, a lengthy calibration process is required. In [56] a low-cost phased array for Wireless Local Area Network (WLAN) application has been proposed. This system uses 2-bit digital phase shifters, thus sacrifices the performance. A set of pre-calculated patterns has been provided and a computer selects the pattern. Indeed, there is no actual beamforming in this system, which results in low adaptability and reliability. A modified Constant Modulus Algorithm (CMA) is proposed in [54] for beamforming of low-complex phased arrays; however, this algorithm requires *a priori* knowledge of the source location.

1.2.2 Statement of the Problem

The purpose of this dissertation is to provide a cost-effective solution to minimize the system complexity of the future intelligent antenna systems *without sacrificing* the system performance. Particularly, the focus of this research is placed on phased array systems. We will propose a novel beamforming algorithm and show, both theoretically and experimentally, that a powerful, efficient beamforming algorithm can compensate for the inaccuracies of the low-cost components used in a phased array system.

Fig. 1.1 illustrates the structure of this thesis. *Cost* and *bandwidth* are two criteria determining our different approaches in this work. Analog phase-shifting leads to a low-cost product. On the other hand, demanding a large bandwidth requires optical delay lines which are more costly than phase shifters. Nevertheless, employing miniaturized ODLs can significantly reduce the device area and consequently the fabrication cost. Regardless of which of the two approaches is chosen, a versatile and robust beamforming algorithm can compensate the side-effects of using cheap components and low-cost fabrication processes. So both roads lead to Rome!

1.3 Outline of this Research

Chapter 2 of this dissertation compares different hardware architectures for phased array antenna and explains the practical limits of analog phase shifters. The best array configuration with our criteria is the one with a single RF chain and mixer. For narrow-band applications phase shifter and for broadband or multi-band applications optical delay lines are used to combine the signals of array elements

constructively.

Chapter 3 introduces four types of miniaturized optical delay lines which can be integrated with other subsystems of a broadband phased array system. These ODLs are distinguished by their bandwidth, delay per device-size, tunability and ease of fabrication.

Chapter 4 discusses the Zero-knowledge beamforming algorithm which is an integral part of the proposed low-cost phased array architecture. The proposed algorithm does not need the knowledge of the desired signal DOA. It adjusts the control voltages of the phase shifter to maximizes the received power or SNR. The only available input in this method is a feedback form the array output power. The algorithm alleviates the hardware errors and imperfections such as the imbalanced insertion loss of the phase shifters, discussed in Chapter 2, and susceptibility to the ambient conditions. The hardware complexity of the algorithm is significantly low. Thanks to the availability of low-cost powerful processors, this beamforming algorithm can be implemented with regular processors.

Chapter 5 describes the experimental test set-up used for this research, and reports the results of several experiments highlighting the performance and properties of the Zero-knowledge beamforming algorithm. Finally, Chapter 6 concludes this research and proposes several directions for future research.

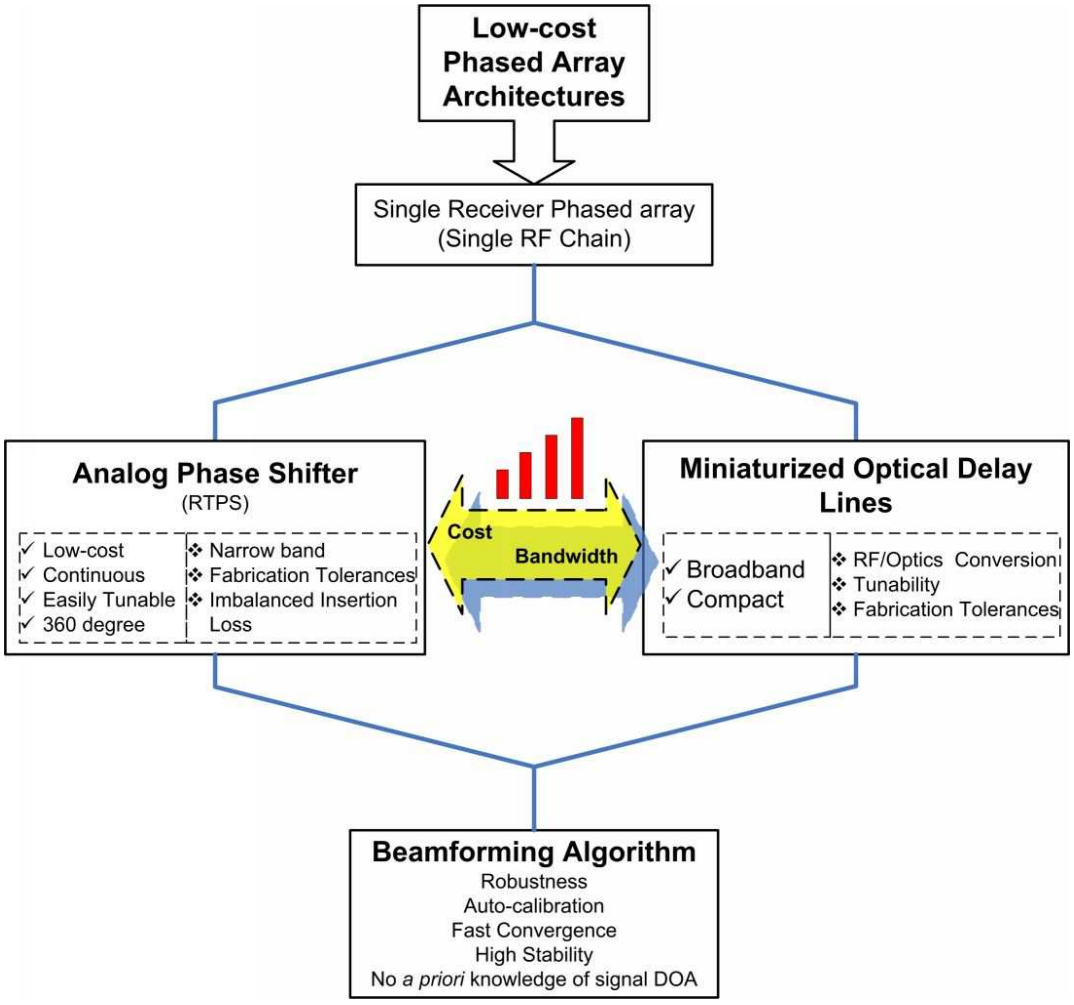

Figure 1.1: Flow of the thesis.

Chapter 2

Narrow-band Phased Array Antennas

In this chapter some theoretical aspects of phased array antenna is discussed and the low-cost hardware architectures for a PAA is described. Also practical considerations and limits of analog phase shifters, the key element of phased array system, are studied in details.

2.1 Introduction to Phased Array Antenna

The main purpose of using phased array antenna is to generate a directive (high-gain) beam which can be relocated electronically [57]. This section reviews the array antenna theorem to derive the principle of pattern multiplication. Furthermore, different configurations of PAA are compared to find a low-cost architecture. Finally, beamforming for PAA is defined as a constrained optimization problem.

2.1.1 Array Antenna Theorem

Consider N arbitrary radiating elements with the same orientation but arbitrarily distributed in the space as shown in Fig. 4.1. In general, the excitation of each element, henceforth called *weight*, is denoted by a complex number such as w_i. Let the electric field (E-field) of a reference antenna located at the origin with a unity weight be [58]

$$\mathbf{E}_0(\mathbf{R}) = \mathbf{f}_0(\theta, \phi)\frac{e^{-jk_0R}}{4\pi R} \tag{2.1}$$

where $\mathbf{f}_0(\theta, \phi)$ is the E-field radiation pattern of the reference element, $\mathbf{R}$ is the distance vector from the element (located at origin), and $k_0 = 2\pi/\lambda$ denotes the wave constant. The distance from the *ith* antenna to the desired far field point (P in Fig. 4.1), i.e. $\mathbf{R}_i$, is given by

$$\mathbf{R}_i \;=\; \mathbf{R} - \hat{\mathbf{r}}.\mathbf{r}_i \tag{2.2}$$

where $\hat{\mathbf{r}}$ is the unit vector along $\mathbf{R}$. At far field where $|\mathbf{R}| \gg |\mathbf{r}_i|,\ \forall i$, the magnitude of $\mathbf{R}_i$ is approximated with $|\mathbf{R}|$. Based on Superposition principle the total E-field caused by all antennas at point P is the sum of the individual electric fields, thus one can show [57]

$$\mathbf{E}_r(\mathbf{r}) = \frac{e^{-jk_0R}}{4\pi R}\sum_{i=1}^{N} w_i\mathbf{f}_i(\theta, \phi)e^{jk_0\hat{\mathbf{r}}.\mathbf{r}_i} \tag{2.3}$$

If *identical* elements are used in the array, then

$$\mathbf{E}_r(\mathbf{r}) = \left[\frac{e^{-jk_0R}}{4\pi R}\mathbf{f}(\theta, \phi)\right]\left[\sum_{i=1}^{N} w_i e^{jk_0\hat{\mathbf{r}}.\mathbf{r}_i}\right] \tag{2.4}$$

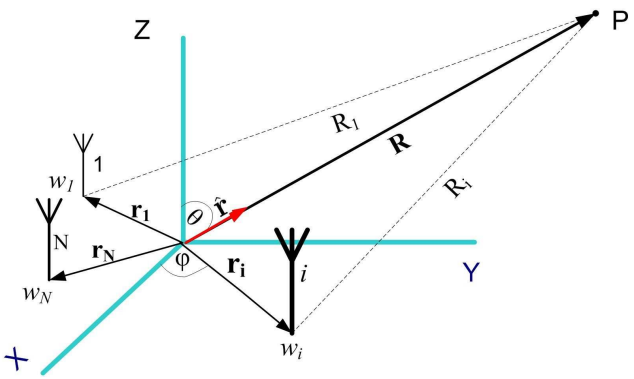

Figure 2.1: Generalized array antenna configuration.

Equation (2.4), known as the *Principle of Pattern Multiplication*, constitutes of the product of two terms: the element pattern given in (2.1) and a summation called *array factor*, and equal to

$$\mathbf{AF}(\theta, \phi) = \sum_{i=1}^{N} w_i e^{jk_0 \hat{\mathbf{r}}.\mathbf{r}_i} \tag{2.5}$$

Here, the joy of phased array antenna begins. Array factor in (2.5) depends on the geometry of the array and the excitation weights. For a fixed array constellation the total radiation pattern can be steered by changing the excitation phases. This property is known as electronically scanning or beam-steering. The array antenna capable of changing the excitation phases is called *phased array antenna*. Phase shifters or delay lines are used to adjust such weights. A beamforming algorithm calculates the required weights (phases or time-delays) to shape or steer the beam. Beamforming algorithm affects the phased array architecture, and vice versa. Implementation of some beamforming algorithms requires complex, bulky or expensive microwave or optical subsystems, while the focus of his thesis is on low-cost PAA. Hence, before discussing the idea of beamforming an affordable architecture for phased array antenna must be determined.

2.1.2 Phased Array Architectures

To steer the main beam of PAA, phase shifters (often delay lines) can be incorporated in different stages of a receiver or transmitter. Thus, four phased array configurations can be obtained. These configurations, shown in Fig. 2.2, are known as RF phase-shifting (single receiver) [57], Local Oscillator (LO) phase-shifting [27], IF phase-shifting [59] and digital beamforming phased arrays [37].

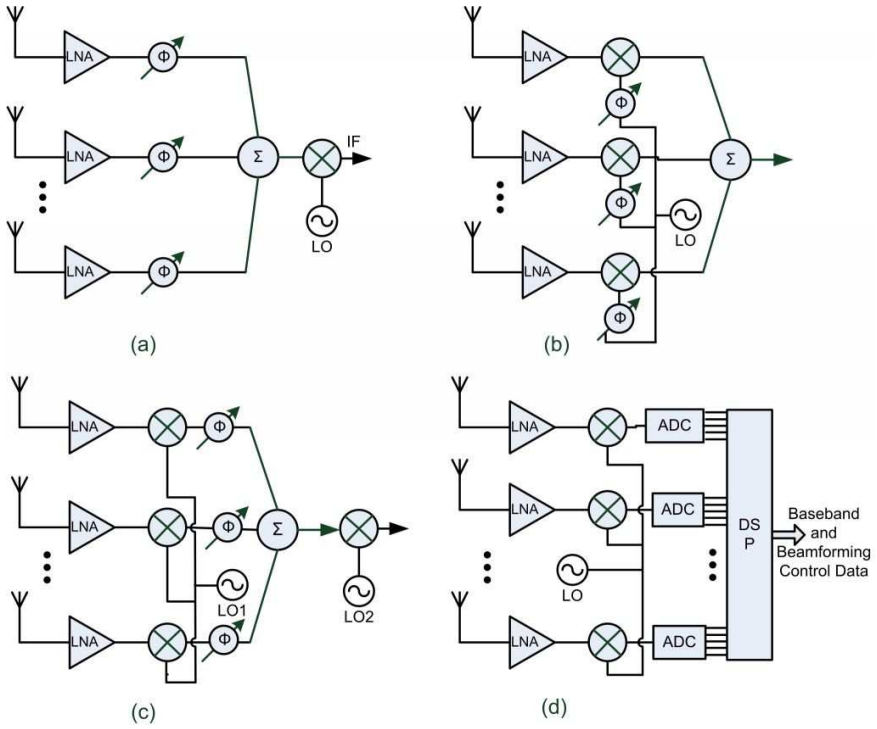

Figure 2.2: Different phased array configurations (a) RF phase shifting, (b) LO phase shifting (c) IF phase shifting, and (d) digital beamforming array.

In the RF phase shifting architecture, (Fig. 2.2(a)), different RF paths are amplified by Low Noise Amplifiers (LNAs), phase-shifted and combined at RF frequency. The combined signal is then down-converted to the IF or baseband. In this architecture the spatial filtering of the strong undesired signals is performed at the combination point, prior to the mixer. Hence, the upper dynamic range requirement of the mixer is relaxed, and the undesired in-band intermodulations after mixer decrease. The design of the RF phase shifter, however, remains a challenge. For example, the insertion loss variation versus phase-shift must be small; otherwise, the beamforming gain is deteriorated [32].

LO phase shifting architecture is displayed in Fig. 2.2(b). The main advantage of this architecture over the previous one is that the loss, non-linearity and noise performance of the phase shifters do not directly affect the receiver performance. However, the number of components is more than that of the RF phase shifting configuration. This leads to more silicon chip area and therefore higher cost for a fully integrated phased array. Besides, since the power combination and beamforming are performed after mixers, in-band intermodulations are stronger. Also the upper dynamic range of the mixer must be high enough to stand the strong

interference signals.

Fig. 2.2(c) shows the IF phase shifting architecture. The phase shifters are placed at the first IF stage and the phase shifted IF signals are combined before the downconversion to baseband. As compared to the RF phase shifting array, some of the challenges in the phase shifter design are relaxed. However, since it needs multiple mixers, this architecture is not a proper option for a low cost and low power phased array transceiver. Fig. 2.2 (d) illustrates the digital array architecture. Down-converted to a suitable IF frequency, each RF path is digitized by an Analog-to-Digital Converter (ADC) and all outputs are passed to a Digital Signal Processing (DSP) unit , which executes all tasks of beamforming and recovering of the desired signal from the undesired interferences. The dynamic range of mixers and ADCs must be high enough to withstand the probable strong interferences. For broadband applications such as WPAN, where the data rate exceeds 1Gbps [60], very high-speed ADC's are required. Moreover, to accommodate the required dynamic range each ADC must have a large number of bits increasing the ADC cost and power consumption extensively.

Table 2.1 compares different phased array architectures in terms of power consumption, chip area and design challenges. The most appropriate configuration to achieve a practical low-cost, low-power and compact phased array is the RF phase shifting architecture. However, designing an efficient front-end as well as developing an efficient and novel beamforming algorithm are the keys to overcome the phase shifter irregularities and challenges in RF path. In the rest of this work the algorithms and equations are developed for an RF phase shifting configuration. For the receiver application, we will refer to this configuration as the single receiver phased array antenna. Appendix A calculates Noise Figure and the expected SNR of this configuration.

2.1.3 Beamforming as an Optimization Problem

As discussed in Section 2.1.1 an efficient beamforming algorithm can exploit the phased array potentials. To state the beamforming problem for a single receiver PAA clearly, we need to find a relation between array weights and received power or SNR.
Let $\mathbf{x}(t) = [x_1(t)\ x_2(t) \cdots x_N(t)]$ denote the received signals by all elements of a single receiver phased array antenna. Then the array output is

$$y(t) \ = \ \mathbf{w}^H \mathbf{x}(t) \tag{2.6}$$

Table 2.1: Overall comparison of different phased array architectures

Architecture	Power Consumption	Chip Area/Cost	Design Challenge
RF Phase Shifting	Low	Low	Efficient front-end Phase Shifter Beamforming Algorithm
LO-Phase Shifting	High	High	Linearity LO distribution, Coupling
IF-Phase Shifting	High	High	Linearity/LO distribution
Digital Array	High	High	Linearity High dynamic range A/D

where $\mathbf{w} = [w_1\ w_2\ ...w_N]^T$ denotes a vector containing the array weights, and ^{H} is the Hermitian operator. Thus, the received power by the phased array is given by:

$$P \ = \ \mathbf{w}^H \mathbf{R} \mathbf{w} \tag{2.7}$$

where $\mathbf{R} = E\{\mathbf{x}(t)\mathbf{x}^H(t)\}$ is the correlation matrix of the received signals $\mathbf{x}(t)$, sometimes known as *array correlation matrix*. The received signal vector $\mathbf{x}$(t) consists of three components: source signal $\mathbf{x}_S(t)$, interference $\mathbf{x}_I(t)$, and background noise $\mathbf{n}(t)$,

$$\mathbf{x}(t) = \mathbf{x}_S(t) + \mathbf{x}_I(t) + \mathbf{n}(t) \tag{2.8}$$

The background noise is assumed to be spatially white with zero mean and average power of σ_n^2 [61]. Assuming $\mathbf{x}_S(t)$ and $\mathbf{x}_I(t)$ are statistically independent, the correlation matrix $\mathbf{R}$ can be evaluated as the sum of three matrices

$$\mathbf{R} = \mathbf{R}_S + \mathbf{R}_i + \sigma_n^2 \mathbf{I}_N \tag{2.9}$$

where $\mathbf{R}_S = E\{\mathbf{x}_S(t)\mathbf{x}_S^H(t)\}$, $\mathbf{R}_i$, and $\mathbf{I}_N$ are the correlation matrix of the source signal, the interference correlation, and the identity matrices, respectively. For the interference-free problems ($\mathbf{R}_i = 0$), signal to noise ratio is given by

$$\rho = \sigma_n^{-2} \frac{\mathbf{w}^H \mathbf{R}_S \mathbf{w}}{\mathbf{w}^H \mathbf{w}} \tag{2.10}$$

Several algorithms have been proposed to find the optimum array weights that maximize the received SNR given in (2.10). Some of these methods, such as Wiener Filter or Maximum Likelihood (ML) beamformer, require either the full knowledge of the array correlation matrix or the direction of the desired signal [39]. The direction of the desired signal is usually referred to as the array *steering vector*, $\mathbf{s}_0$.

Steering vector gives the array weights required to point the beam to the desired source. So, to find it the source direction and phase shifter characteristics must be known precisely. If $\mathbf{R}$ and $\mathbf{s}_0$ are known the well-known Sample Matrix Inversion method (SMI) gives the following optimal weights:

$$\mathbf{w}_{opt} = \frac{\mathbf{R}^{-1}\mathbf{s}_0}{\mathbf{s}_0^H \mathbf{R}^{-1}\mathbf{s}_0} \ . \tag{2.11}$$

Matrix $\mathbf{R}$ can be expressed in terms of a unitary matrix of eigenvectors $\mathbf{U}$ and a diagonal matrix of eigenvalues Λ,

$$\mathbf{R} \ = \ \mathbf{U} \ \Lambda \ \mathbf{U}^H \tag{2.12}$$

hence the inverse matrix is easily calculated,

$$\mathbf{R}^{-1} \ = \ \mathbf{U} \ \Lambda^{-1} \ \mathbf{U}^H$$

Equation (2.10) can be simplified further for a linear equispaced array with identical elements. In this case the received signal from the source, $\mathbf{x}_S$, is expressed as

$$\mathbf{x}_S(t) = s(t) \left[1 \ e^{ju} \cdots e^{j(N-1)u}\right]^T \tag{2.13}$$

where $s(t)$ is the source waveform and the incremental phase shift, u, is related to the angle of arrival, θ, the array spacing d and the received signal's wavelength λ by

$$u = \frac{2\pi d}{\lambda} \sin(\theta) \ . \tag{2.14}$$

Assuming $|s(t)|^2 = 1$, the correlation matrix $\mathbf{R}_S$ is given by

$$\mathbf{R}_S = \begin{bmatrix} 1 & e^{ju} & \cdots & e^{j(N-1)u} \\ e^{-ju} & 1 & \cdots & e^{j(N-2)u} \\ \vdots & \vdots & & \vdots \\ e^{-j(N-1)u} & e^{j(N-2)u} & \cdots & 1 \end{bmatrix} \tag{2.15}$$

which is a positive definite Hermitian matrix. The received SNR for a uniform linear array is then

$$\rho = \frac{\sum_{k=1}^{N} \sum_{l=1}^{N} w_l w_k^* e^{j(l-k)u}}{\sigma_n^2 \sum_{k=1}^{N} |w_k|^2} \tag{2.16}$$

The unconstrained solution which maximizes (2.16), known as *phase-conjugate* relation, is

$$w_k^* = g_0 e^{jku} \quad \forall k \tag{2.17}$$

where g_0 is a constant. In general, *maximum array gain theorem* states that the array gain reaches its maximum value when each weight (w_i) is proportional to the

complex conjugate of the element gain [62]. Element gain is a complex number whose phase is identical to that of the received signal.

Despite optimum beamformer, adaptive beamforming method estimate the array correlation matrix [63] [64]. Comparison of the different adaptive algorithms is beyond the scope of this work. However many of these methods are intended to cancel the interference, thus they need a reference signal. One way to provide such a reference is to use another (array) antenna. There other adaptive methods which estimate the correlation matrix. These methods either need N channel receivers (similar to Fig. 2.2(d)), or use inaccurate perturbation methods to estimate $\mathbf{R}$.

In section 2.3 and 4.1 we will show that in practice some of the assumptions made to find the optimum weights, i.e. full knowledge of $\mathbf{R}$ and $\mathbf{s}_0$ and phase shifter parameters, are not realizable with a low-cost phased array architecture. In Chapter 4, we introduce Zero-knowledge beamforming which does not depend on these assumptions.

2.2 Analog Phase Shifting

In this section different analog and digital phase shifters are compared and the characteristics of a low-cost analog phase shifter is discussed.

2.2.1 Analog and Digital Phase shifters

Phase shifter is the key element in the beamforming network of phased array antenna. Some of the challenges in phase shifter design for a low cost PAA are:

1. Phase linearity, which is a complicated task at higher frequencies
2. Minimum insertion loss
3. Low complexity of phase control: minimum control complexity with very few number of control voltages is required to reduce the number of digital/analog controlling parameters.

Phase shifters are classified into digital and analog types. In the first class (digital phase shifters) multi stages (bits) with constant phase shifts are cascaded and either utilized or by passed by switches. Fig. 2.3(a) shows one bit of a digital phase shifter known as switched line phase shifter. PIN diode or MOSFET switches are

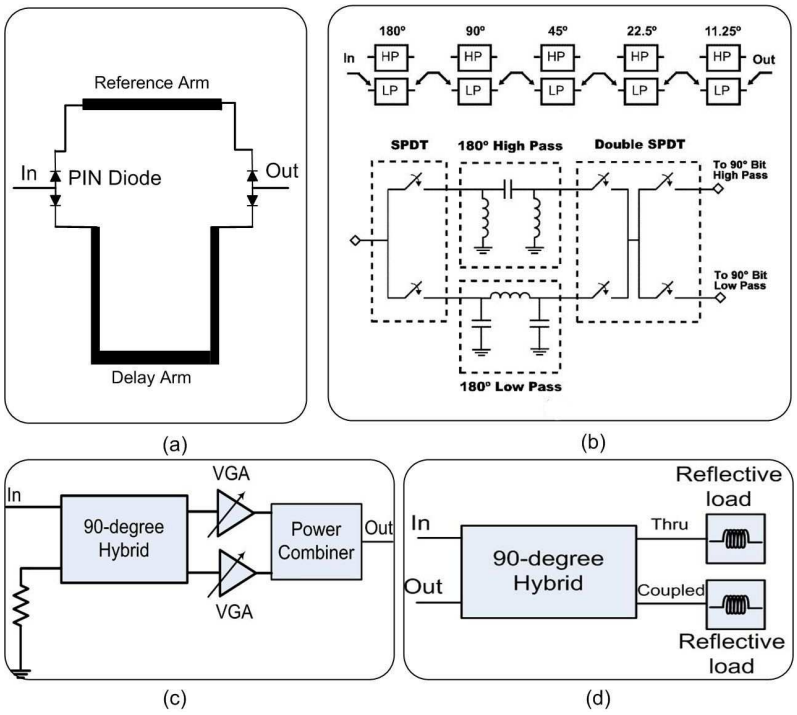

Figure 2.3: Digital and analog phase shifters. (a) Digital switched line phase shifter. (b) Digital high-pass low-pass phase shifter. (c) Analog vector summing phase shifter. (d) Analog reflective-type phase shifter.

used to select the reference or delay (phase shift) arm. The obtained phase shift increases with the length of the delay arm. The same structure has been widely used for optical delay lines. The high-pass/low-pass phase shifter shown in Fig. 2.3(b) takes the difference between the phase from the high-pass filter path and the low-pass filter path of a particular bit [30, 65, 66]. The main challenges of digital phase shifters are the loss associated with the switches [67, 68] and the complexity of switching network. For an N-bit digital phase shifter at least 2N switches must be enabled/disables each time. Moreover, they do not provide continuous phase shifting which results in a high side-lobe level in the radiation pattern of PAA. Also the beam pointing accuracy is degraded. In contrast, analog phase shifters shift the phase continuously.

Two well-known analog structures are vector summing and reflective-type phase shifters (RTPS) depicted in Fig. 2.3(c) and (d) respectively. The linearity performance of the vector summing phase shifters is poor due to the active phase shifting and also the power consumption required to achieve a high dynamic range is large [30, 66]. In the remainder of this Chapter, RTPS is used to provide continuous 360° phase shift.

2.2.2 RTPS Function

RTPS structure employs a 4-port 90°-hybrid and two similar purely imaginary (reflective) loads. The through and coupled ports of the hybrid are terminated with the reflective terminations and the isolated port is used as the output.

The incident signal at the input reaches the output after reflection back from the imaginary loads. The reflective loads can be altered electronically, mechanically or magnetically; hence, the phase of the reflection coefficient at the through and coupled ports changes. This results in the phase shift of the output signal. The amount of phase shift depends on the load type. Several passive terminations are proposed for the reflective loads. A single varactor cannot provide phase shift more than 75° in practice. Adding a series inductor can increase the phase shift up to 180°. To achieve a complete 360° phase shift one should use dual resonated loads.

2.2.3 Measured Characteristics

More than 20 Ku-band (12.2–12.7GHz) RTPS were fabricated using Microwave Integrated Circuits (MIC) technology. Fig. 2.4 depicts the properties of the best fabricated sample at the center frequency of 12.45GHz,. The normalized insertion loss ($|S_{12}|$) and the insertion phase ($\angle S_{12}$) of this phase shifter were measured using HP–8722ES network analyzer. Here, normalization means that all constant losses such as copper loss have been neglected. The details of the phase shifter design are given in [13]. Insertion phase in Fig. 2.4(c) varies almost linearly versus the bias voltage, but insertion loss in Fig. 2.4(b) shows a non-uniform and nonlinear behavior versus voltage. We refer to this phenomenon as the *imbalanced* insertion loss, which impairs the beamforming performance of PAAs as will be shown in the following section.

2.3 Practical Considerations of Analog Phase Shifters

In this section three practical drawbacks of analog phase shifters namely imbalanced insertion loss, fabrication errors and narrow-band performance are discussed and measured data for each case is presented. It is shown that the imbalanced insertion loss of phase shifters significantly affects coherent beamforming gain.

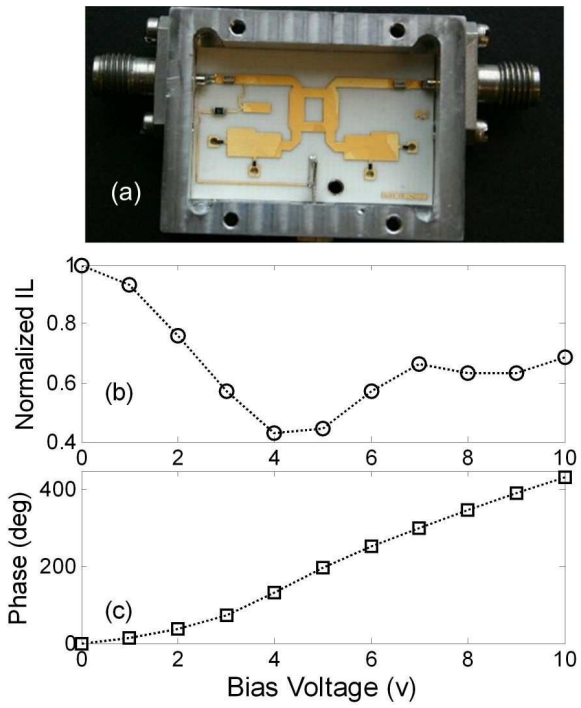

Figure 2.4: Reflective-type phase-shifter with 90° hybrid coupler. Measured characteristics at $f = 12.45GHz$ using network analyzer (HP 8722ES). The dashed lines show the fitted polynomials. (a) Fabricated device. (b) Phase-shift versus voltage, (c) insertion loss versus voltage.

2.3.1 Imbalanced Insertion Loss

Analog IC designers have mostly focused on achieving linear phase shift; hence, the effect of Insertion Loss (IL) on the beamforming -the main purpose of using phase shifters- has been neglected. An increase in the receiver Noise Figure due to the unequal values of IL has been addressed earlier [69]; however, most of such analyses assume that IL is constant over the control voltage range, and the strongest signal can be achieved through coherent beamforming.

Background

Different types of analog phase shifters have been developed so far [70]– [75] and the key element of most of them is a voltage variable capacitor (varactor). As the reverse bias voltage of the varactor varies, the capacitance and the phase of the total impedance change. Although this mechanism provides a linear or quasi-linear phase shift (versus bias voltage), it causes two major problems. First, the insertion loss is not constant for all desired phase shifts, and second, it is not a linear function of the required phase shift (see Fig. 12 in [70] and Fig. 14 in [71]). In [72] a Ku-band ferroelectric phase shifter on Silicon was introduced whose IL changed from

0.4 to 2.6dB at 15GHz. In [73] an optimally loaded phase shifter with continuous phase shift from 0° to 360° at 20GHz was reported. Its IL varied from 1.7dB to 4.2 dB for the bias voltages ranging from 0 to -10v (see Fig. 7 in [73]). As the authors correctly mentioned the majority of the circuit loss was due to the varactor diodes. In [74] a Ku-band Monolithic Microwave Integrated Circuit (MMIC) analog phase shifter (12-14GHz) was presented with a phase shift of more than 180° and an IL of 3.6 ± 1.1dB. Finally, a tunable phase shifter implemented with 0.18-μm CMOS technology was presented in [75], where the average IL of the phase shifter was 0.3dB with a variation of $\pm$0.8dB. Despite different implementation methods and operational frequencies, all of these phase shifters suffer from imbalanced IL [70]–[75].

Coherent Beamforming Gain

Fig. 2.5 shows a linear array of N *identical* omni-directional elements separated by a distance d. A source radiates at angle θ relative to the array normal. Let ϕ_m denote the phase of the received signal by element m. From (2.14) one can show that the phase-lag between elements 1 and m is given by

$$\Delta\phi_m = \phi_m - \phi_1 = 2\pi(m-1)\frac{d\sin\theta}{\lambda} \tag{2.18}$$

The received signals pass through phase shifters, represented by weights w_1, w_2, ..., w_N, and combine by the power-combiner, denoted by Σ. Each weight can be represented by a complex number with magnitude of f_m and phase of ψ_m, i.e.

$$w_m \;=\; f_m \; exp(j\psi_m) \; . \tag{2.19}$$

Assuming the received power by each element is equal to unity, the total received signal by the combiner (array output in (2.6)) will be

$$\begin{aligned} Y(\psi_1, \cdots, \psi_N) \;&=\; \sum_{m=1}^{N} w_m \exp(-j\phi_m) \\ &= \sum_{m=1}^{N} [f_m \exp(j\psi_m)] \exp(-j\phi_m) \end{aligned} \tag{2.20}$$

The goal of beamforming is to maximize the array output. The maximum array gain theorem proposes that each phase shifter must be adjusted to the phase-conjugate of the corresponding received signal. So, regarding the sign convention in (2.20), the phase-shift generated by each phase shifter must be

$$\psi_m = \phi_m \qquad 1 \;\leq\; m \;\leq\; N \; . \tag{2.21}$$

Hence, all exponential terms in (2.20) vanish, thus the received signals become *coherent* at power combiner. The total coherent received signal, Y_{Coh}, is the sum of the individual magnitudes in (2.20)

$$Y_{Coh} = S(\phi_1, \cdots, \phi_N) = \sum_{m=1}^{N} [f_m] \tag{2.22}$$

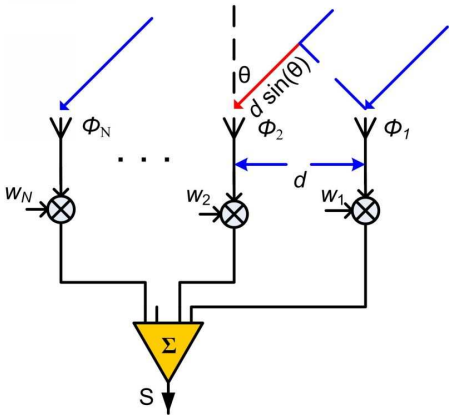

Figure 2.5: Simplified block diagram of a linear array of N identical elements.

The maximum array gain theorem is valid if the amplitude of w_m, i.e. f_m, is a constant, independent of its phase (ψ_m). However, as discussed earlier, this assumption is not valid for practical analog phase shifters, because f_m varies with the control voltage [70]– [75]. Fig. 2.4 illustrates that phase shift is a monotonic function of bias voltage, hence the insertion loss of each phase shifter, f_m can be expressed as a function of its phase

$$f_m \;=\; f(\psi_m) \;=\; f(\phi_1 + \Delta\phi_m). \tag{2.23}$$

Thus the coherent received signal in (2.22) can be expressed as

$$Y_{Coh} = S(\phi_1, \cdots, \phi_N) = \sum_{m=1}^{N} [f(\phi_1 + \Delta\phi_m)] \tag{2.24}$$

If IL were constant versus the bias voltage, $f(\psi) = f_0$, for all values of ψ , Y_{Coh} would have been a constant equal to Nf_0.

Phase-Added Coherent Beamforming

By adding a constant phase ($\delta\psi$) to all phase shifters, clearly phase differences between elements do not change. However, when IL varies as in Fig. 2.4(b), where

$f(\phi_m + \delta\psi) \neq f(\phi_m)$, the amplitude of the total received signal will change. Thus, it might be possible to find a proper $\delta\psi$ that provides a stronger sum, such that

$$Y_{Coh} \leq Y(\phi_1 + \delta\psi, \cdots, \phi_N + \delta\psi) \tag{2.25}$$

The right side of (2.25) can be expressed as

$$S(\phi_1 + \delta\psi, \cdots, \phi_N + \delta\psi) = \sum_{m=1}^{N} [f(\phi_1 + \delta\psi + \Delta\phi_m)] \tag{2.26}$$

To illustrate the advantage of adding a constant phase, consider an array of two elements, N=2, with half-wavelength spacing. The source direction (θ in Fig. 2.5), varies from 0-180°. Fig. 2.6(a) compares the coherent array gain, Y_{Coh}, and the added-phase gain, i.e. $S(\phi_1+\delta\psi, \cdots, \phi_N+\delta\psi)$, for the best value of $\delta\psi$ which gives the highest array gain. The best $\delta\psi$ depends on the source direction. Fig. 2.6(b) shows the improvement in the array gain achieved by adding a constant phase, which varies from 0 to 0.33dB, and its maximum occurs at $\theta = 24°$. So when IL varies with voltage, the coherent beamforming ($\delta\psi = 0°$) does not necessarily bring about the maximum gain. Moreover, it is seen that the imbalanced insertion loss reduces the array gain by 44%. Hence the imbalanced loss of the phase shifters has a serious effect on array output. It is necessary to look for a beamforming algorithm which maximized the array output instead of only compensating the received phase shifts. In section 4.4 we show how the proposed beamforming algorithm can compensate the imbalance loss of phase shifters to a large extent.

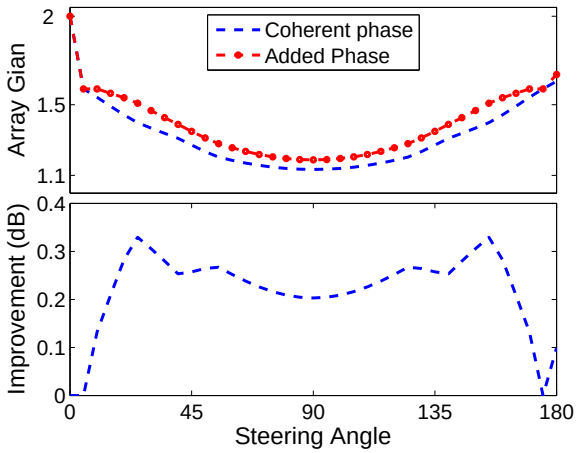

Figure 2.6: Coherent beamforming for a 2-element array.

2.3.2 Fabrication and Design Tolerances

In addition to the imbalanced insertion loss, phase shifters suffer from fabrication and design tolerances similar to other microwave devices. Fig. 2.7 shows the phase–voltage graphs of 17 RTPS devices fabricated using MIC technology to be utilized in the Ku-band PAA, which will be described in Chapter 5. In these measurements, each phase shifter was connected to an LNA via a piece of cable identical to the one used in the Ku-band PAA. The slopes of phase–voltage curves in Fig. 2.7 are different, so are their starting points. Thus, it is impossible to find one single relation to describe or model all phase shifters. Practically, the phase shifter characteristics

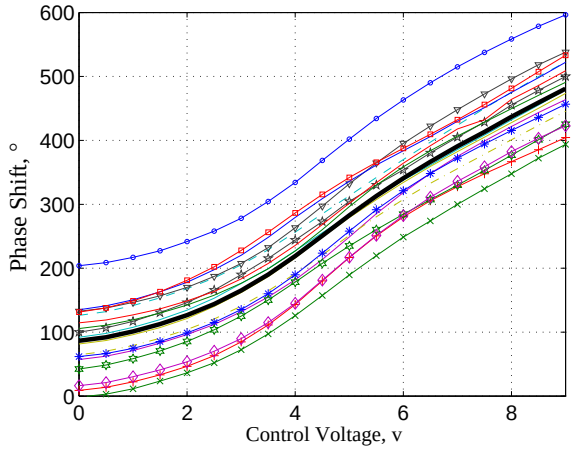

Figure 2.7: Phase-voltages characteristics of 17 analog phase-shifters connected to 17 similar LNAs via cables. The dark solid line shows the average of all curves.

depend on the environmental parameters, such as temperature and humidity, which may change from one day to another day [48]. An efficient beamforming algorithm cannot depend on a constant phase-voltage relation. It must be insensitive to the device tolerances. Most of the RF beamforming algorithms only find or estimate the required phase shift for each element assuming the phase-voltage relation is known. For example, they assume there is a permanent look-up table to find the control voltage for a desired phase shift. In the Zero-knowledge beamforming algorithm introduced in this thesis (Chapter 4) the phase shifter is treated as a black-box. A monotonic relation between phase and voltage is the only assumption made in dealing with phase shifters.

2.3.3 Narrow-band Performance of RTPS

Fig. 2.8 shows the characteristics of the fabricated RTPS (with LNA and connecting cables) over frequency (f_0=12–13GHz). It is seen that for a constant control voltage

as the frequency is swept for 1GHz, almost 8%, the phase shift and the insertion loss vary up to 350° and 2.5dB respectively. It shows the narrow-band performance of this type of phase shifters. More or less, other analog phase shifters have the similar performance and are not suitable for broadband applications. The drawback of using narrow-band components in a PAA system is known as the *Beam Squint*.

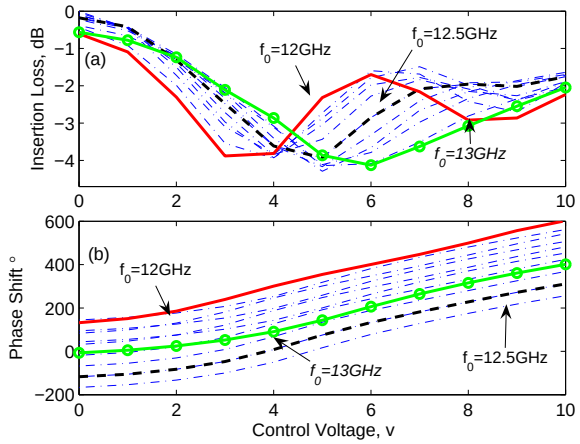

Figure 2.8: Measured characteristics of RTPS versus frequency.

Beam Squint

Suppose phase shifters are adjusted to cancel phases of the received signals at a frequency of f_0. The required phase shift between two adjacent elements of a phased array increases with frequency

$$\Delta\phi(f) \;=\; \phi_m(f) - \phi_{m-1}(f_0) = \frac{2\pi d \sin\theta}{c}(f - f_0) + \Delta\phi(f_0) \qquad (2.27)$$

In a practical system, as the measurements in Fig. 2.8(b) show, it does not necessarily happen. In fact, sometimes the reverse case is observed (compare 12GHz and 12.5GHz curves). Thus as the frequency varies, the main array beam deflects to a direction different from that of the desired source. This drawback of the narrow-band microwave components is known as beam-squint (see Ch.1 in [57] and Ch.20 in [76] [1]). Practically beam squint broadens the antenna beam or lowers the effective radiation gain. Although the beamforming algorithm described in Chapter 4 is able to alleviate this effect [77], the ultimate solution is to use true-time delay lines to generate time-delay instead of phase shift. The required time-delay between two adjacent elements of a linear equispaced array is

$$\Delta\tau \;=\; \frac{d \sin\theta}{c} \qquad (2.28)$$

[1] In their analysis they assume the output phase shift of the phase shifter is constant over the frequency range which is nat a valid assumption.

which is independent of the carrier frequency. Optical delay lines (ODL) possess the highest bandwidth amongst all delay lines and have been used in the wideband phased array systems over the past three decades [34]– [35].

2.4 Conclusion

Single receiver PAA is *the* low-cost architecture. Analog phase shifter is the key element of this architecture. Low-cost analog phase shifters such as RTPS with satisfactory phase linearity and simple control mechanism can be fabricated. However analog RF phase shifters come with a few drawbacks. The first problem is the imbalanced loss of the phase shifters which for example reduces the array efficiency of a 2-element array up to 44%. One of the contributions of this thesis is investigating the effect of the imbalanced loss on beamforming gain [32, 77].

Narrow-band behavior and fabrication errors are other drawbacks of analog phase shifters and other microwave components in a PAA. Use of optical delay lines in the beamforming network of PAA can combat the beam squint effect caused by narrow-band microwave elements. Thus, four types of miniaturized optical delay lines will be studied in next chapter.

In Chapter 4 we will show how an efficient beamforming algorithm can overcome the drawbacks of analog phase shifters resulting in a low-cost PAA.

Chapter 3

Miniaturized Optical Delay Lines

3.1 Introduction

In Chapter 2 it was shown that the combination of LNA, analog phase shifter and connecting cables makes a narrow-band microwave system, which is inappropriate for broadband or multi-band applications. In this chapter we analyze four types of miniaturized Optical Delay Line (ODL), which can be integrated with other optical subsystems to constitute a broadband PAA. Over the past three decades, bulky ODLs have been used in the beamforming network of broadband phased array systems [34]– [35]. Nevertheless, ODL is the key element for a variety of applications, such as optical division multiplexing [78], filter design [79], and optical signal processing [80]. Several types of ODLs have been developed so far, such as optical fiber [81], fiber Bragg grating [82]- [83] and Coupled Resonator Optical Waveguides (CROW) delay lines [84].

Fiber is a low loss medium. It supports the propagation of large bandwidth signals; however optical fibre delay lines are bulky, so the integration of such delay lines with other optical subsystems is not practical. For example, Chang et al. [85] used a 940m graded index multimode fiber as a delay line to generate $4.99\mu s/km$ delay. A solution to achieve more compact delay lines, which appeared in the early 90's, was the use of fiber Bragg grating instead of regular single mode fibers. For example, Ortega et al. [86] fabricated an ODL with a maximum delay of $330ps$ for a $5cm$ uniform grating. The performance of such delay lines is only two times better than free space in terms of the required propagation length, so still the packaging and integration problems exist. Furthermore, most of the variable ODLs developed so far are switched delay lines, which cause high sidelobe levels in the radiation pattern of the antenna array [87], and need a complex switching network. In this chapter we introduce two solutions to obtain compact and continuous delay elements: Photonic Crystal (PC) and coupled ring resonator delay lines.

Use of PC structures is a promising solution to reduce the size of the delay elements [88]. A very small group velocity can be achieved at the band edges of PCs [89]. Nonetheless, the bandgap mechanism itself decelerates the propagation of light. Moreover, light in PC can be confined around sharp bends, in lower-index media, and within the wavelength-scale cavities. The other important advantage of PC is that it can be integrated with Silicon-on-Insulator (SOI) and CMOS devices to achieve a low-cost product. Recently, several works have been reported on the design and fabrication of photonic crystal devices, particularly delay lines [90] - [95]. However, all of these works, use *straight* line structures, so to achieve a longer time delay, the device size must be scaled linearly. In the first half of this chapter our focus is on two different structures for ODLs in photonic crystals:

- Waveguide-based Delay Lines [88, 96, 97], discussed in Section 3.2

- Coupled Cavity (Defect) Delay Lines [97, 98], discussed in Section 3.3

In [99] we have shown that the amount of delay generated by PC delay lines is adequate for the beam-steering of a 5-element wide-band PAA.

In addition to photonic crystals, slow wave structures can potentially manipulate group velocity of light [100]. Their small dimension has opened the way to the integrated ODLs. Such structures are either *enhanced dispersive* or *resonant* media. The dispersion-length product of the dispersive structures determines the absolute time-delay. Increasing the dispersion narrows the effective bandwidth, while increasing the length obviously increases the device size. The dispersive delay lines are lossy and if used in the beamforming network of phased array as the light wavelength changes to tune the delay, the side-lobes level of the array pattern grow dramatically, *e.g.* -5dB in [101]. Coupled optical ring resonators form an important and versatile class of slow light structures, and have have been recently proposed for wideband beamforming [102]- [103].

For the purpose of beam-steering, tunability of the delay line is crucial. A continuous delay line is necessary to steer the beam accurately to any direction within the coverage region and avoid complex lossy and bulky switching circuits. Fortunately, there are several methods to tune the time delay of coupled optical ring resonators by adjusting the coupling factors, such as the Electro-Optic (EO) or Thermo-Optic (TO) effect or changing the resonance wavelength. The change in refractive index due to temperature, known as the Thermo-Optic (TO) effect, can be significantly large for certain optical material [104]. Thus a wide tuning range for TO-controlled ring resonators can be obtained. However the currently developed coupled ring ODLs suffer form two major drawbacks: 1) the reported rise time for TO phase shifters is not better than $1ms$ [105], and 2) the coupling factors are adjusted manually [103]. Hence if coupled ring ODLs are to be used in PAA, an automatic fast method to adjust the coupling factors is necessary. In Section 4.7 we will propose a solution for this purpose.

In the second half of this chapter the focus is on coupled ring resonators. Two general configurations for realizing an optical delay line with ring resonators are discussed. In the first configuration multiple rings are coupled to a waveguide (bus), while there is no mutual coupling between them. This structure known as Parallel Ring Resonator (PRR) or allpass filter will be studied in Section 3.4. In the second structure the adjacent rings are mutually coupled. This configuration known as cascaded ring resonator will be discussed in Section 3.5.

3.2 Meandering Delay Line in Photonic Crystal

In this section general characteristics of photonic crystals are described. Furthermore, a novel meandering structure for delay generation is introduced.

3.2.1 Photonic Crystals

Photonic crystal, also known as Photonic Bandgap (PBG) material, is a structure with a periodically modulated dielectric constant. If the depth of the refractive index modulation is adequate, a frequency range will exist, where certain optical modes are forbidden to propagate. This frequency range is known as *bandgap*. Fig. 3.1 demonstrates two well-known PC structures consisting of cylindrical holes/rods surrounded by another material. These structures are characterized by the distance between rods/holes known as the *lattice constant*, denoted by a, the radius of the rods/holes, denoted by R_0, and the refractive indices of the constituting material.

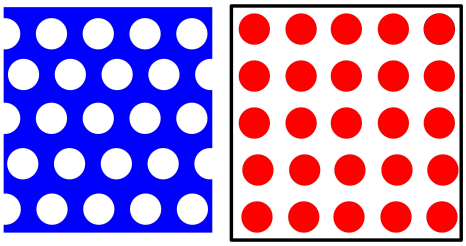

Figure 3.1: Top view of two conventional structures for 2D photonic crystals. Left: triangular lattice. Right: square lattice.

Existence of bandgap and the width of bandgap both depend on the ratio of rod radius to lattice constant, R_0/a. Consider a square lattice of Silicon rods surrounded by air (Si/Air lattice). Using the plane-wave expansion method [106], we find the bandgap(s) for each value of R_0/a swept from $0.05a$ to $0.40a$ in steps of $0.005a$. Eventually, a graph like Fig. 3.2, called *gap-map*, is achieved, which conveys important information for design of PBG devices. Fig. 3.2 shows that the maximum bandgap for Si/Air square lattice occurs for $R_0 = 0.18a$. As illustrated in Fig. 3.3, the first and largest bandgap for $R_0 = 0.18a$ ranges from $0.3\ a/\lambda$ to $0.44a/\lambda$. Having the widest bandgap is an appropriate criterion for setting lattice parameters, because it compensates for the fabrication errors and uncertainties in designing wide-band PC devices.

In practice, dimensions of a PC structure are limited and the periodicity terminates at some point. Therefore photonic crystal slabs are used to realize optical devices. PC slabs are 2D periodic dielectric structures of finite height with a band gap for propagation in the plane of periodicity. The index-confinement is used for

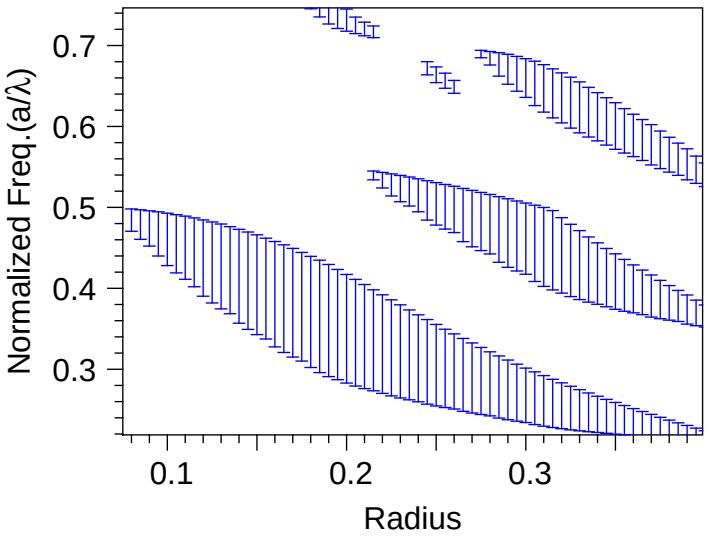

Figure 3.2: Gap-map for the square lattice of silicon rods in air derived using the plane-wave expansion method.

guiding light in the third dimension. PC slabs are also called quasi-two-dimensional (2D) PCs because their structure and properties imitates those of 2D PCs [107]. Since the fullwave analysis of 3D structures is time-consuming and needs significant amount of memory, usually 2D simulation is used to study the general properties of the PC device.

3.2.2 Meandering Delay Lines

Meandering lines consist of parallel waveguide sections connected with crossed interconnections. Two conventional arrangements for this category of delay lines, used at the microwave frequencies, are serpentine (meander) and double spiral shown in Fig. 3.4. Despite optical fibers, low-loss sharp bends are realizable in PC [108]. Furthermore, from the transmission line theory, we know that an open-circuit termination causes total reflection (just similar to a mirror or reflector). So the forward traveling wave returns back to the input terminal. In a well-designed photonic crystal waveguide the walls around the channel behave like mirrors reflecting lightwave [109]; so, if one puts a mirror at the end of the waveguide, the traveling lightwave will return. This can be realized by removing a certain number of cells in a PBG lattice to open a channel and stopping at some point adequately far from the boundaries. The closed end of the channel behaves like a mirror for the wavelengths inside the bandgap, with a reflection coefficient close to 1 [97]– [96]. Fig. 3.5 shows the implementation of this idea in PC. The detailed design steps of this *novel* structure, henceforth called *Reflective Spiral Line* (RSL), have been

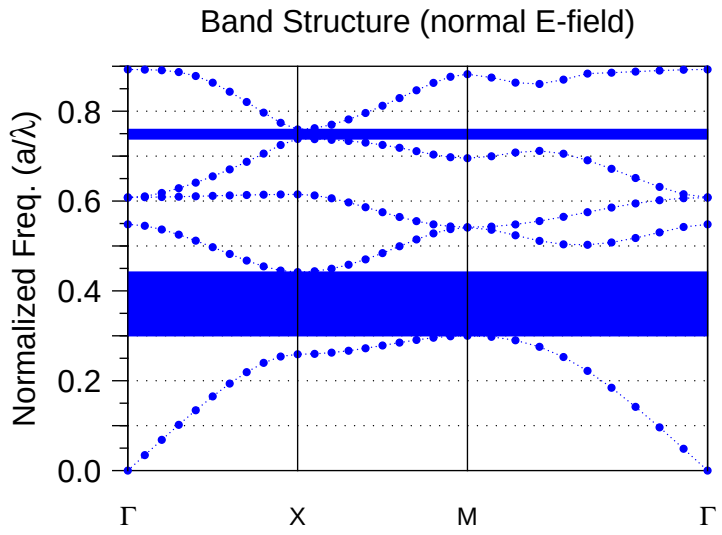

Figure 3.3: Bandgap diagram of the E-field component normal to the plane of propagation for $R_0 = 0.18a$.

described in [97,98]. Fig. 3.6 shows the front panel of a Garland sarcophagus (Roman A.D. 140–170). Several ancient designs can be seen on this panel including a meander pattern similar to the proposed delay line.

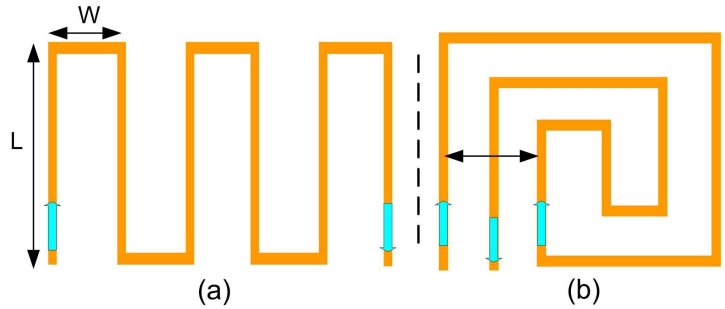

Figure 3.4: Two types of meandering line structures. (a) Serpentine, (b) Double spiral.

RSL structure shown in Fig. 3.5 consists of Si pillars $n = 3.46$ surrounded by air. The PC parameters are optimized for $\lambda = 1.55\mu m$. Therefore the lattice constant and and the rod radius are fixed at $a = 574nm$, and $R_0 = 103nm$ respectively. To reduce the crosstalk of the delay line, the channel spacing, N_R, is fixed at 5 and channel lengths are limited to $21\mu m$. All corners have been mitered to reduce the bending loss [98]. Since RSL is a one port device, an optical circulator is required to separate the input and output signals. In [110] an optical circulator formed by inserting magneto-optical cavity in a 2D PC is proposed.

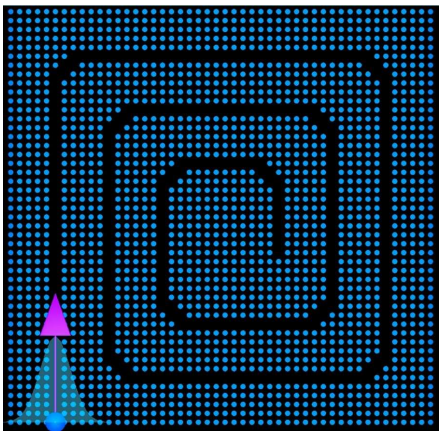

Figure 3.5: Top view of Reflective Spiral Line (RSL) carved in a square lattice photonic crystal.

Figure 3.6: Front panel of a Garland sarcophagus (Roman A.D. 140–170), available at Getty museum L.A., CA, USA.

3.2.3 FDTD Analysis of RSL Delay Line

Fig. 3.7 shows the envelope of the monitored E-field (normal to the plane) at the input/output of the RSL. Here, *delay* is defined as the time difference between the maximum of the input pulse envelope, centered at $t = 0$, and the maximum of the reflected pulse recorded at the output terminal. *Loss* is defined as the square of the input and reflected E-field ratio. These are two qualitative criteria to facilitate the comparison of different structures. The FDTD analysis reveals that the time-delay of this structure is close to $2ps$ and the loss is less than 0.3dB. The largest device size, including the margins, is $L = 27\mu m$.

To provide a meaningful comparison of the time delay relative to the device size, a figure of merit is defined as: $F_d = c\tau_d/L$, where τ_d is the obtained time delay. This figure of merit simply states how many times light can be slowed down in this structure compared to free space. The effect of the meandering shape is included in the definition of F_d. Using Fig. 3.7 F_d for the designed RSL is calculated to be 22.2. In [97] we have compared RSL structure with conventional structures for

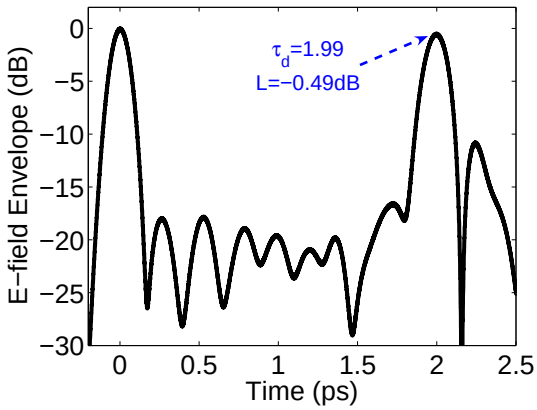

Figure 3.7: Envelope of the E-field detected at the input/output of the Si/Air Reflective Spiral delay line

delay lines, i.e. meandering line and double spiral line shown in Fig. 3.4. The performance of RSL in terms of the propagation delay, loss and cross talk is at least two times better than other structures with the same device size.

3.2.4 Tunability of the Time-delay

Further FDTD analysis shows that the generated delay in RSL increases with the optical carrier wavelength (Fig. 3.8). If wavelength varies from $1.49\mu m$ to $1.61\mu m$, almost by %8, the time delay increases by %25. The propagation loss drops as the wavelength approaches the center wavelength ($1.55\mu m$) and after that it grows.

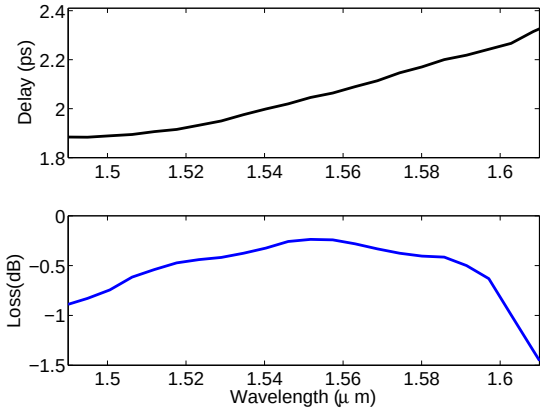

Figure 3.8: Delay and Loss versus wavelength for Reflective Spiral delay line.

To implement the same structure with other material such as Si/SiO_2, the lattice characteristics must change. For this case the maximum bandgap occurs for

$R_0 = 0.226a$ and is centered at $a/\lambda = 0.284$, thus for $\lambda_0 = 1.55\mu m$, a and R_0 must be set to $440nm$ and $100nm$ respectively.

Fig. 3.9 displays the envelope of the monitored E-field at the input/output of the Si/SiO_2 RSL, where both delay and loss have increased to $2.21ps$ and 3.3dB; however, the device size has shrunk to $20.7\mu m$. Therefore, $F_d = 32.05$ for Si/SiO_2 RSL delay line, which implies that the propagation of light in Si/SiO_2 PC delay line is 1.45 times slower than Si/Air configurations.

In [96] we have shown that RSL structure can be modified to generate two time delays. The larger time delay is twice of the smaller time delay.

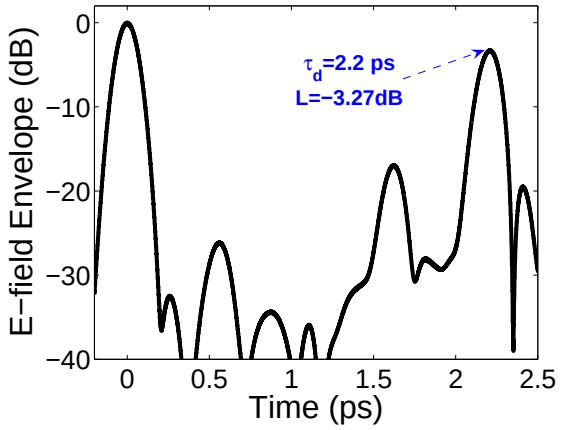

Figure 3.9: Envelope of the E-field detected at the input/output of the Si/SiO_2 Reflective Spiral delay line.

3.3 Coupled Cavity Delay Lines in Photonic Crystal

A defect is a modified cell in a periodic lattice. For example, changing the radius of any rod/hole in Fig. 3.1 from the default value, or even removing one rod/hole, makes a local defect, which behaves like a micro-cavity [111]– [112]. Micro-cavities are designed such that their resonant frequency falls within the bandgap of the surrounding PC. Moreover, periodic defects in PC function as a low-loss waveguide. The infinitesimal size of such structures is the key to obtain the ultra-miniaturized delay lines. The size of delay line depends on group velocity. Group velocity of light, propagated in the periodic defects, is inversely proportional to the coupling

strength between the adjacent cavities [113]. However an estimate of group velocity is necessary to find the delay line configuration.

3.3.1 An Approximate Method to Find the Group Velocity

Fig. 3.10 shows a narrow section of a PC lattice which contains two coupled cavities made by removing two rods. A chain of such defects makes a slow-wave medium suitable for designing delay lines. In this figure, D represents the number of rods between two cavities. To find the effect of the inter-defect spacing on group velocity, the left cavity is excited with a wideband Gaussian modulated pulse and the amplitude of the E-field at the center of the second cavity is monitored. Fig. 3.11 shows the amplitude and the spectrum of the source signal used to excite the left cavity. The input pulse spectrum is centered at the resonance wavelength of a single isolated cavity derived from the spectral analysis of the FDTD results. This procedure is repeated for D varying from 1 to 6. After exciting the first cavity, the resonant E-field builds up immediately. The E-field amplitude decreases gradually, because energy is coupling from the first cavity to the second one. Consequently the E-field amplitude in the second cavity grows. This process continues until the E-field in the first cavity reaches its minimum value. Simultaneously, the E-field in the second cavity peaks. As time passes, the E-field shows a periodic behavior without any significant drop in its peak amplitude. Fig. 3.12 demonstrates the E-field at some point close to the middle of the second cavity versus time, for $D = 1$ to 4.

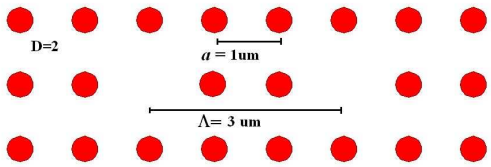

Figure 3.10: Demonstration of two coupled cavities with $D = 2$.

To find group velocity, first we define the *coupling period*, T_κ, as the time required for a complete transfer of energy from the first cavity to the second one. The coupling period increases with the defect spacing, which means energy needs a longer time to transfer. Fig.3.10 clarifies that the center to center distance of two cavities, Λ, is

$$\Lambda = (D + 1).a \ . \tag{3.1}$$

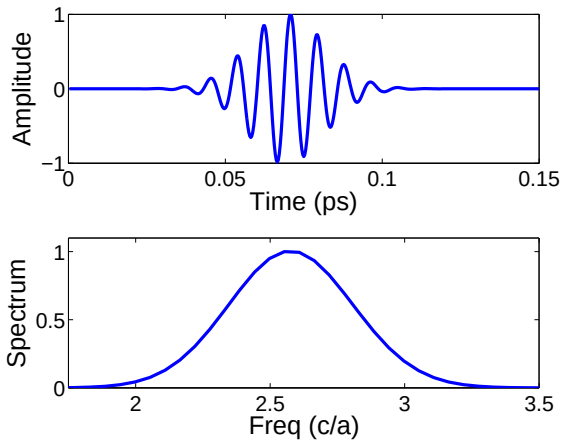

Figure 3.11: Amplitude and spectrum of the source signal

The *effective group velocity* for energy transfer between the two cavities, v_{ge}, is defined as

$$v_{ge} = \frac{\Lambda}{T_\kappa} \quad . \tag{3.2}$$

To compare the calculated effective group velocities with c, the speed of light, the

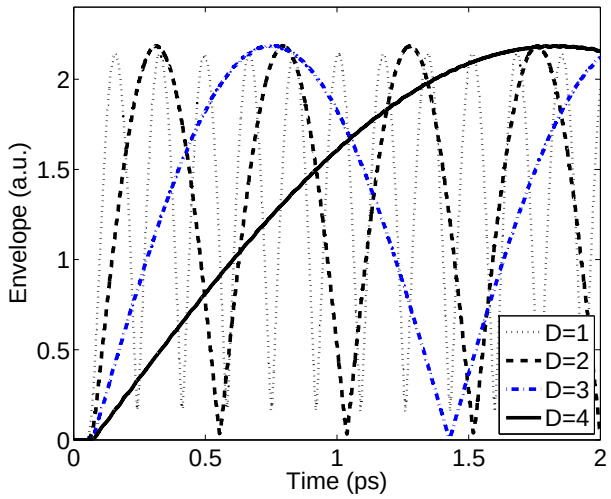

Figure 3.12: Envelope of the E-field in the second cavity for $D = 1, 2, 3$ and 4.

Slowing Factor, SF, is defined as c/v_{ge}. Fig. 3.13 shows the calculated values of SF with this approximate method. The following exponential relation can be fit to the calculated values for SF

$$SF = 12.75\ e^{[0.73(D-1)]} \quad . \tag{3.3}$$

Numerical analysis of the large delay lines with large inter-defect spacings is too time-consuming. Nevertheless, we can analyze a small section of the larger delay

line to find its effective group velocity, using the above method. Then we can predict the time delay of whole delay line.

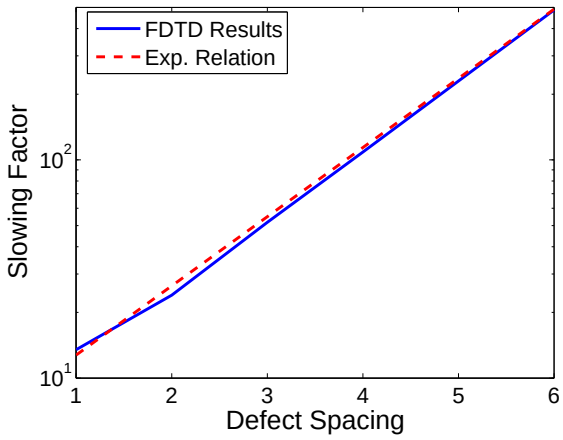

Figure 3.13: The Slowing Factor calculated using FDTD method. The vertical axis is in Log-scale.

3.3.2 Performance of Coupled Defect Delay Lines

Reflective Spiral delay line is the best option among other meandering line structures to obtain a longer delay. however the size–crosstalk considerations restrict the maximum achievable time delay, unless we can make the propagation of light slower. Fortunately the effective group velocity of light in PC coupled cavities is much slower than free space or Si, so by replacing waveguide channels in Fig.3.5 with coupled defects (see Fig. 3.14), a significant increase in the delay is expected. To prevent the fast coupling between parallel branches, the inter-branch spacing must be at least $2 \times \Lambda$. FDTD simulations show that energy can easily couple between the defects making 90° corner, and no further corner mitering is required.

For $D = 2$, 71 defects, arranged as an RSL configuration, can be inserted in a $27\mu m \times 27\mu m$ PC lattice. Fig. 3.15 demonstrates the envelope of the input and reflected E-fields monitored at the first cavity of this structure in Si/Air PC lattice. It shows that the time delay has increased to $8.97ps$. Nonetheless, the more impressive result is the reduction of loss to 0.1dB. So, the other important feature of this delay line is its negligible loss.

For this coupled defect delay line the defined figure of merit is calculated to be $F_d = 100$, which indicates this structure decelerates light 100 times compared to free space. The performance of this delay line is 4.5 times better than the RSL delay line in Fig. 3.5. Considering the results of the approximate method for finding the

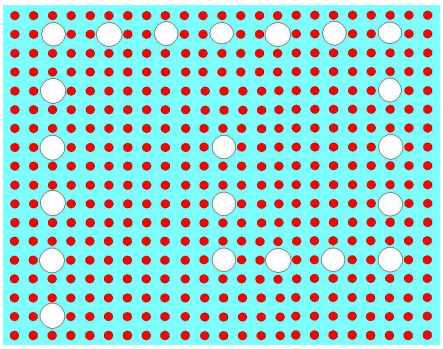

Figure 3.14: A section of RSL made by coupled defect with D=2. Each white circle represents a missing rod.

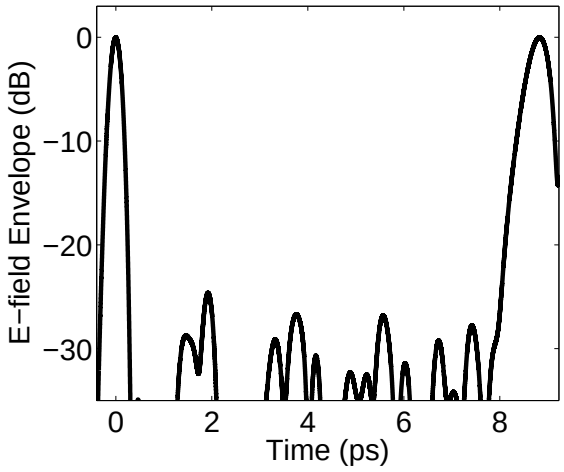

Figure 3.15: Envelope of the E-field recorded at the first cavity of a coupled defect Si/Air Reflective Spiral delay line with $D = 2$.

effective group velocity, if the inter-defect spacing is increased to 3, the time delay will increase 2.14 times.

3.4 Parallel Coupled Rings

Fig. 3.16 demonstrates a two-port structure named Parallel Ring Resonator (PRR). In this configuration, ring resonators are coupled only to the waveguide and have no mutual coupling. The ports are called input port and through port. In following we derive an expression for group delay of PRR and analyze its transient response. TO phase shifters are used to adjust coupling. The temperature of each TO phase shifter is controlled by the DC bias voltage.

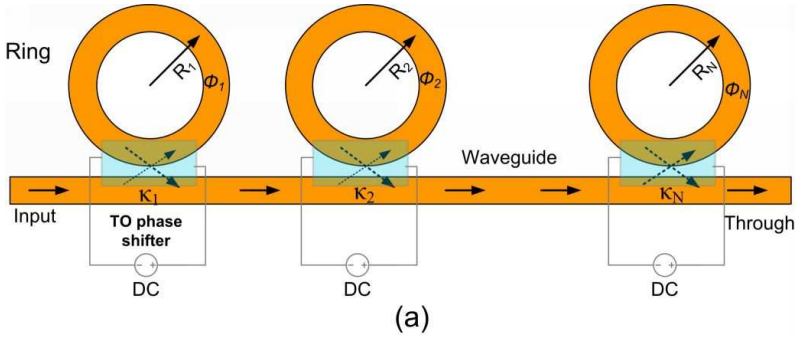

Figure 3.16: Multiple ring resonators coupled to a waveguide. TO phase shifters adjust the coupling factors.

3.4.1 Group Delay of Parallel Coupled Rings

Transmittance of PRR is defined as the ratio of the E-field at the through port to the input E-field. Transfer matrix method is used to find the transmittance of a single ring with one coupling point [114]:

$$H(\omega) = \frac{E_T}{E_I} = \frac{\sqrt{1-\kappa} - e^{-(\alpha+j\beta)L}}{1-\sqrt{1-\kappa}e^{-(\alpha+j\beta)L}} \tag{3.4}$$

where κ is the power coupling coefficient between ring and waveguide, α represents the propagation loss, β is the propagation constant, and $L = 2\pi R$ is the ring circumference. Group delay by definition is the derivative of the phase of the transmittance function with respect to angular frequency

$$\tau_{gd}(\omega) \;=\; -\frac{\partial \angle H(\omega)}{\partial \omega} \tag{3.5}$$

In the absence of loss ($\alpha = 0$) and nonlinear dispersion, the group delay of a single ring is given by

$$\tau_1(\omega) = T_r \frac{\kappa}{(2-\kappa) - 2\sqrt{1-\kappa}\cos(\beta L)} \tag{3.6}$$

where T_r, the round trip delay of the ring, is determined by the effective refractive index of the waveguide n_{eff} and L, i.e. $T_r = n_{eff}\ L/c$. Delay in (3.6), τ_1, is a function of coupling factor and ring size. Maximum time delay which occurs at the resonant frequencies, when $\beta L = \ 0,\ 2\pi, \cdots$, increases dramatically as the coupling factor decreases to very small values. In contrast, bandwidth decreases such that the delay-bandwidth product remains almost constant. Fig. 3.17 illustrates the impact of coupling factor κ on the transmittance of a single ring versus κ. The maximum delay could be more than 200 times of the ring round-trip delay with the price of a negligible bandwidth.

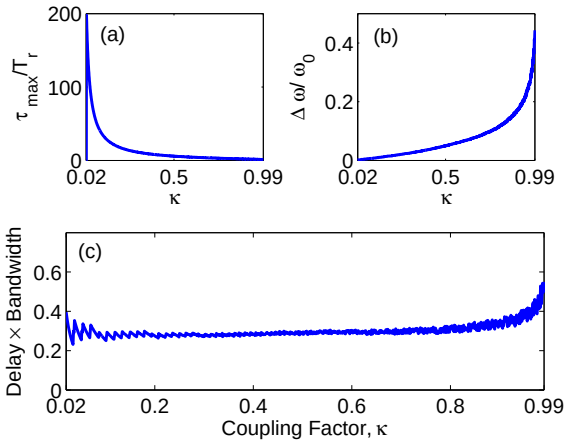

Figure 3.17: Impact of coupling factor on Transmittance of a single ring. (a) Normalized time delay at resonance frequency, (b) Fractional Bandwidth, (c) Delay–bandwidth product.

To achieve longer time delays for a *certain bandwidth*, more rings must be used, similar to Fig. 3.16. The distance between the adjacent rings must be adequately large to prevent any mutual coupling. Hence, the total delay is equal to the sum of the time delays of all rings plus a constant delay (T_W) resulting from propagation of light in the waveguide sections between rings,

$$\tau_M = T_W + \sum_{n=1}^{M} T_n \frac{\kappa_n}{(2-\kappa_n) - 2\sqrt{1-\kappa_n}\cos(\beta L_n)} \tag{3.7}$$

where κ_n, T_n, and L_n respectively denote the coupling factor, round trip delay, and circumference of each ring. To obtain the largest bandwidth for a certain time delay all coupling factors must be equal, provided that all rings are identical.

3.4.2 Full-wave Analysis of Single Ring Delay Line

Transfer matrix method, discussed in the previous section, is a frequency domain method and only predicts the steady-state response of the delay line. However in designing an optical subsystem, the transient analysis may be crucial if, for example, there are high overshoots or undesired spectral components that must be prevented. Moreover, the simple formulation presented earlier, which is based on weak-coupling assumption and a unitary and unimodular coupling matrix [115], ignores several practical issues such as dispersion effects, the phase of coupling, and bending loss. (Some modifications have been suggested in [116].) Nonetheless, full-wave analysis is based on direct implementation of Maxwell's equations, hence

it precisely considers the complex nature of evanescent mode coupling in coupled ring resonators and illuminates the transient time-response of the structure. In the following, the effects of wavelength, gap-size and loss on the time delay and transient behavior will be discussed using the FDTD analysis.

FDTD Modeling of Single Ring Delay Line

Fig. 3.18 shows a single ring ($n_{eff} = 3$) coupled to a waveguide. The average radius of the ring is $R = 3.4\mu m$ and the width of the waveguide and ring is $w = 0.2\mu m$. Also the gap-size between ring and waveguide is $240nm$. This figure shows a snap-shot of the resonant E-field during the transient phase when the incoming light has been captured in the ring and only a negligible part of it travels to the through port.

The FDTD method is used to model the resonant structure and find the behavior of the electromagnetic fields. Initially the resonant frequencies of the side-coupled ring resonator must be found. Therefore, the input port is excited by a wide-band Gaussian-shaped E-field pulse with its field perpendicular to the plane made by ring and waveguide (along y direction Fig. 3.18). The 10dB bandwidth of the Gaussian pulse centered at $\lambda_0 = 1.47\mu m$ covers wavelengths from $1.1\mu m$ to $2.2\mu m$. The grid size is $10nm$ and the time-step is set to $\Delta t \simeq 2 \times 10^{-17}s$ to satisfy the Courant criterion for 2D FDTD ($\Delta t \leq \Delta x/c\sqrt{2}$) [117]. The computational domain includes 780×820 cells and the simulation time is $1.25ps$, equal to 2^{16} time-steps. The PML boundary condition is applied to all boundaries. To find the resonant frequencies, the time evolution of the normal E-field, E_y is monitored at 3 points: A) waveguide entry, B) waveguide output, and C) the far right side of the ring. After applying Fourier Transform to the monitored electric field, the resonant frequencies are found by searching for local maximum points in the spectrum. At these frequencies the slow light propagation is expected. Some of the resonant frequencies of this structure (R=$3.4\mu m$) are found to be: $1.28\mu m$, $1.52\mu m$, $1.73\mu m$, $1.87\mu m$ and $2.05\mu m$.

Transient Response versus Wavelength

Coupling between ring and waveguide depends on the gap-size to wavelength ratio. The smaller the ratio, the stronger the coupling. To study the early transient response for different coupling situations,the input port was excited by a CW E-field. The gap-width was fixed at $240nm$ while the optical wavelength was selected from the list of resonant frequencies. Fig. 3.19 demonstrates the envelope of the electric-field.

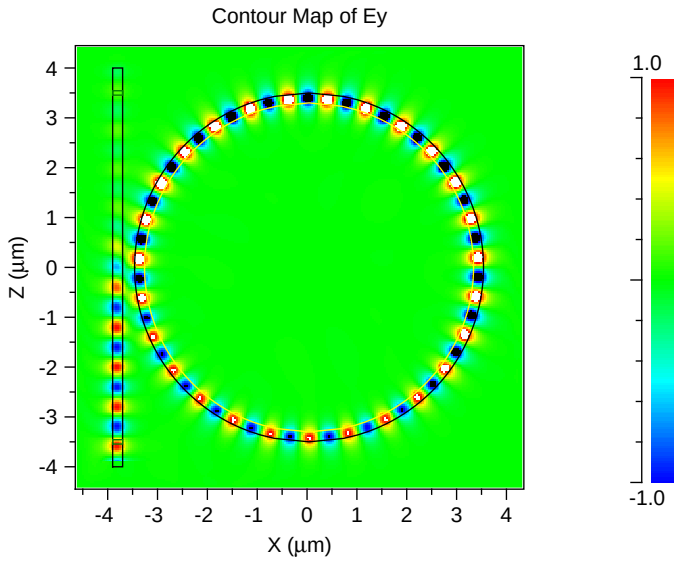

Figure 3.18: A snapshot of the E-field of a single coupled ring resonator using FDTD.

The transient responses show a *descending staircase* behavior. The hight and width of the first step decrease as the coupling becomes stronger. Based on modal analysis, the effective refractive indices of the waveguide sections for each wavelength are respectively $2.39, 2.27, 2.175, 2.106$ and 2.029. Reduction of the refractive index justifies the slight reduction in the width of the steps in the transient response. The width of each step is approximately:

$$T_S = n_{eff}\frac{2\pi R \ + \ 2w_{gap}}{c} \tag{3.8}$$

where w_{gap} denotes the gap-size. For weak coupling situations a large fraction of the input signal travels directly to the output port and bypasses the ring, so a high peak in the transient response is observed.

Delay versus Coupling

Fig. 3.20 depicts the envelope of the E-field at through port for 3 different gap-sizes, namely 100, 160 and $240nm$. These gap-sizes correspond to strong, moderate and weak couplings, respectively. The optical wavelength in this analysis was fixed at $1.52\mu m$. For weak and moderate coupling cases, first a descending-staircase behavior is observed which is in agreement with the previous discussion. For moderate coupling the transient response takes one cycle but for the weak coupling it takes six cycles to reach the minimum value. After the transient phase, both curves follow an ascending-staircase pattern until they reach the steady state, where the amplitude of the E-field is 95% of the input E-field. For strong coupling situation

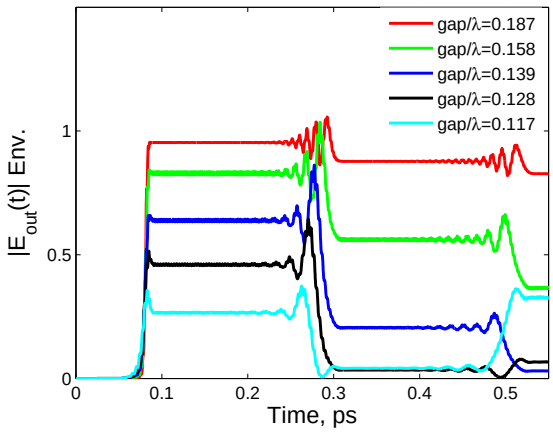

Figure 3.19: Transient response of a single ring PRR for different gap-size to wavelength ratios.

no descending-staircase pattern is observed. The ascending pattern starts immediately and after 2 cycles exceeds the steady state level (95%). It takes three more cycles to reach the steady state. This behavior can be described as an overshoot. Interestingly, these three curves behave similar to the three cases of the transient response of a second order linear system, namely under-damped, critically damped and over-damped responses. In some applications such as high-speed buffering the under-damped response must be prevented because of the overshoots which may change the states.

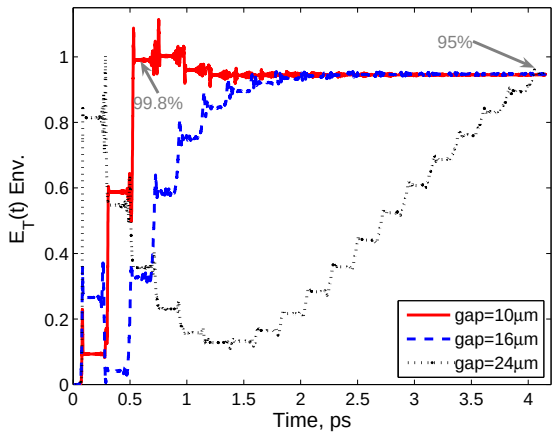

Figure 3.20: Step response of the single ring coupled resonator.

Effect of Loss

Fig. 3.20 compares the envelope of the E-field for lossless and moderate lossy waveguide sections. For the lossy waveguide α in (3.4) is set to $10^{-3}\mu m^{-1}$. Loss affects

the long term response more than the transient response, because the interaction-time between light and ring increases. In fact (3.4) can be expanded as a geometric series representing the iterated transmissions through the ring [118]. As the ring loss increases the ratio between the successive terms decreases, so does the sum. Hence, weak coupling in a lossy medium decreases the steady state level.

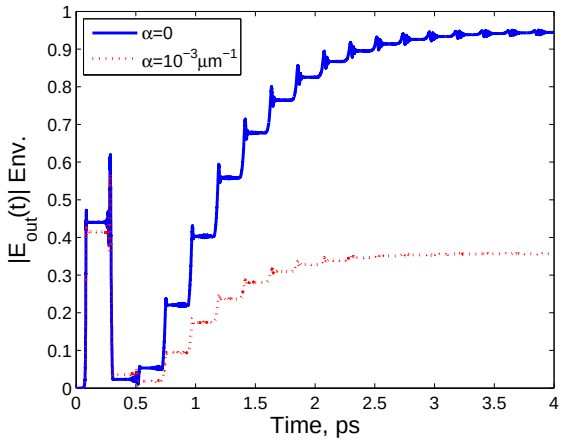

Figure 3.21: Transient responses of loss-less and lossy ring resonators.

3.5 Cascaded Coupled Ring Resonator

Cascaded coupled ring resonator structure consists of mutually side-coupled rings resonators similar to Fig. 3.22, which shows a Double Ring Resonator (DRR). With a proper design the input and output (drop port in Fig. 3.22) ports become isolated; hence, cascaded rings have been widely used for filter synthesis [119] and guiding lightwave [84]. In this section, group delay equations are derived for a DRR, however the results are extendible to multiple ring resonators. In [120] it is shown that as the number of rings increases the product of delay and coupling coefficient increases linearly.

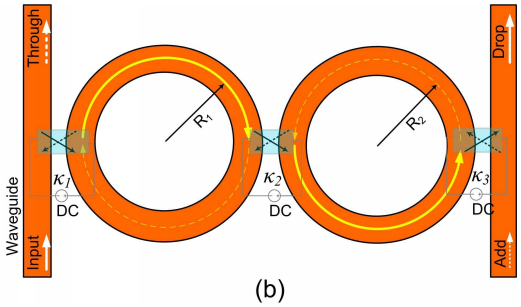

Figure 3.22: Configuration of a double ring resonator.

3.5.1 Group Delay of DRR

Several analytical models can describe cascaded ring resonators behavior such as the LC ladder network, which is more appropriate for filter synthesis [121], or a chain of symmetrical directional couplers connected by transmission lines [122]. In the latter model the input and output fields of each coupler are related through a coupling matrix

$$C = \frac{j}{\sqrt{\kappa}} \begin{bmatrix} -\sqrt{t} & 1 \\ -1 & \sqrt{t} \end{bmatrix} , \tag{3.9}$$

where $t = 1 - \kappa$ is the power transmittance factor. Each transmission line section is represented by a propagation matrix given by

$$P = \begin{bmatrix} \exp(\alpha + j\beta L) & 0 \\ 0 & \exp(-\alpha - j\beta L) \end{bmatrix} . \tag{3.10}$$

A DRR shown in Fig. 3.22 is characterized by 5 parameters: R_1 and R_2 the radii of the rings, κ_1 and κ_3 the coupling factor between the waveguides (bus) and the rings, and finally κ_2 the coupling factor between the rings. For a symmetric DRR we define the bus and ring power coupling factors as $\kappa_b = \kappa_1 = \kappa_3$ and $\kappa_r = \kappa_2$. Thus the power transmittance factors are calculated as $t_b = 1 - \kappa_b$ and $t_r = 1 - \kappa_r$. Thus, the transfer functions from the input port to the through and drop ports, E_T/E_I and E_D/E_I, are given by [123]

$$\frac{E_T}{E_I} = \frac{a\sqrt{t_b}e^{-2j\beta L} - \sqrt{a}(1 + t_b)\sqrt{t_r}e^{-j\beta L} + \sqrt{t_b}}{at_b e^{-2j\beta L} - 2\sqrt{at_b t_r}e^{-j\beta L} + 1} \tag{3.11}$$

$$\frac{E_D}{E_I} = \frac{\sqrt{a}(1 - t_b)\sqrt{1 - t_r}e^{-j\beta L}}{at_b e^{-2j\beta L} - 2\sqrt{at_b t_r}e^{-j\beta L} + 1} \tag{3.12}$$

where $a = \exp(2\alpha L)$ denotes the power transmittance per ring and equals 1 for lossless transmission. Let Φ denote the phase of the drop channel transfer function, which can be calculated as

$$\Phi = -\beta L - \tan^{-1}\left[\frac{at_b \sin(2\beta L) - 2\sqrt{at_b t_r}\sin(\beta L)}{at_b \cos(2\beta L) - 2\sqrt{at_b t_r}\cos(\beta L) + 1}\right] \tag{3.13}$$

Using chain rule the group delay defined in (3.5) can be expressed as:

$$\tau_{gd}(\omega) \ = \frac{n_{eff}}{c} \ \tau_{gd}(\beta) \tag{3.14}$$

Differentiating (3.13) with respect to β, yields $\tau_{gd}(\beta)$

$$\tau_{gd}(\beta) \ = \ L \ + \ L \ \frac{A_0 + A_1\cos(\beta L) + A_2\cos(2\beta L)}{B_0 + B_1\cos(\beta L) + B_2\cos(2\beta L} \tag{3.15}$$

where

$$\begin{aligned} A_0 &= 2a^2t_b^2 + 4at_rt_b \\ B_0 &= a^2t_b^2 + 4at_rt_b + 1 \\ A_1 &= -2\sqrt{at_rt_b}(3at_b+1) \\ B_1 &= -4\sqrt{at_rt_b}(at_b+1) \\ A_2 &= B_2 = 2at_b \end{aligned}$$

Fig. 3.23 shows the drop and through channel responses and the group delay of the drop channel for different values of κ_r, when $a = 1$, $\kappa_b = 0.5$, $R = 134\mu m$ and $n_{eff} = 3.46$. As κ_r decreases from 0.15 to 0.02, the time delay increases from $144ps$ to $305ps$. For larger values of κ_r, the group delay around resonant frequency is not flat and has two separate peaks. For wideband phased arrays the squint-free beamforming requires a constant time-delay for all microwave frequencies. Thus, the appropriate values for coupling coefficients, which provide a *flat* group delay, must be found.

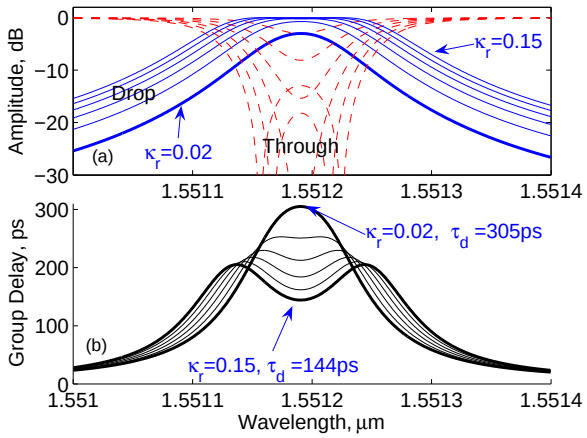

Figure 3.23: DRR response when $\kappa_b = 0.5$ and κ_r is changing. (a) Drop channel and Through channel responses. (b) Group delay versus optical wavelength.

3.5.2 Maximally Flat Group Delay Condition

To find the condition to obtain a maximally flat group delay, one can zero the second derivative of the group delay in (3.14) w.r.t. ω at the resonant frequency. Hence, a relation between the coupling/transmittance coefficients will be found,

$$(2at_b\sqrt{at_bt_r} - 8at_b + 4at_bt_r + 2\sqrt{at_bt_r})(at_b - 2\sqrt{at_bt_r} + 1)^3 = 0 \qquad (3.16)$$

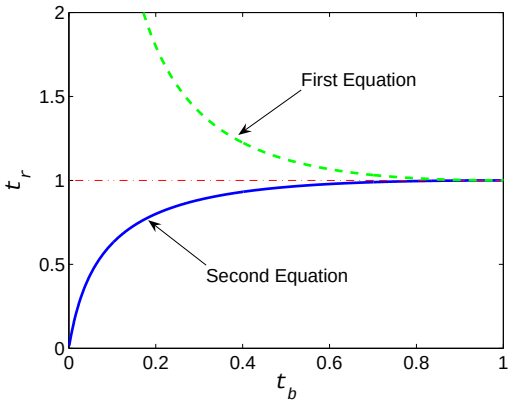

Figure 3.24: Finding transmittance coefficients for maximally flat group delay.

which gives the following two solutions for $a = 1$:

$$t_r = \frac{(1 + t_b)^2}{4t_b} \tag{3.17}$$

$$t_r = \frac{-(1 + t_b) + \sqrt{1 + 34t_b + t_b^2}}{4\sqrt{t_b}} \tag{3.18}$$

Fig. 3.24 shows the solutions of (3.17) and (3.18). The solutions of (3.17) are unacceptable for a passive DRR. Fig. 3.25 illustrates the transfer function and the group delay versus wavelength for $0.05 \leq t_b \leq 0.35$ when t_r satisfies the condition given in (3.18). The group delay is maximally flat and changes almost linearly from $65ps$ to $118ps$. Through channel behaves like an all pass filter except around the resonant region. Drop channel has less than 2dB loss at the resonant frequency. This loss decreases as t_b and t_r increase. In Fig. 3.25 there are two regions, around $1550.17nm$ and $1550.56nm$, where the group delay versus wavelengths remains constant. Optical beamforming when the carrier is within these regions results in a normal array beam which does not deflect by updating coupling coefficients.

The number of coupling factors increases with the number of rings Hence, zeroing the second derivative of the group delay at several frequencies around the resonance provides the extra equations to find coupling factors of multiple ring resonators.

3.5.3 Sensitivity Analysis of DRR

In a practical system there are several sources of error. A high sensitivity to error makes the system unreliable. Sensitivity of the group delay, $\delta\tau_{gd}$, to the errors in

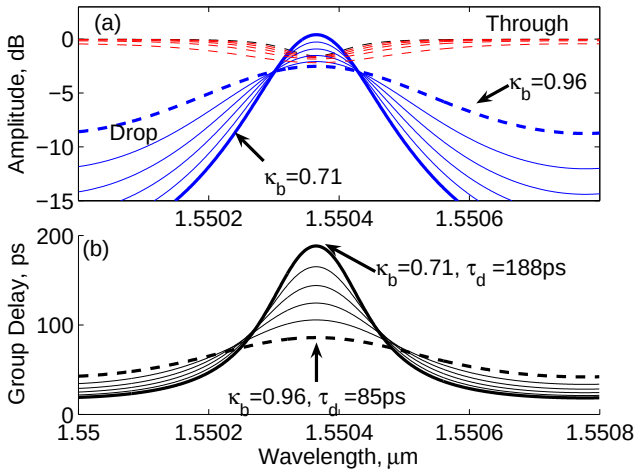

Figure 3.25: DRR response when maximally flat group delay is applied. Comparing this figure with Fig. 3.23 (scales are different) the improvement in the flatness of the group delay is seen.

transmittance coefficients, δt_b , δt_r is given by

$$\delta\tau_{gd} \;=\; \frac{\partial\tau_{gd}}{\partial t_b}\delta t_b \;+\; \frac{\partial\tau_{gd}}{\partial t_r}\delta t_r \;. \tag{3.19}$$

Fig. 3.26 shows the gradient of the group delay w.r.t. the transmittance factors at the resonant frequency for $a = 1$ and $0 < t_r, t_b < 0.95$ (the detailed equations are too lengthy to be presented here). The behavior of $\partial\tau_{gd}/\partial t_b$ significantly differs from that of $\partial\tau_{gd}/\partial t_r$. In Fig. 3.26(a), as both transmittance coefficients approach the maximum value, 0.95, the gradient increases dramatically. For the small values of t_r, the gradient is negative and as t_b increases $\partial\tau_{gd}/\partial t_b$ approaches smaller values ($e.g.\ \partial\tau_{gd}/\partial t_b = -9.3 : t_b = 0.95, t_r = 0.014$). There is a line on this surface where $|\partial\tau_{gd}/\partial t_b| \simeq 0$. In Fig. 3.26(b) $\partial\tau_{gd}/\partial t_r$ is always negative. For small values of t_b and large values of t_r, the gradient is close to zero ($e.g.\ \partial\tau_{gd}/\partial t_r = -0.066 : t_b = 0.11, t_r = 0.95$), however as t_r grows the gradient reaches large negative values. The chain of circles in Fig. 3.26(b) shows the gradient for the maximally flat coefficients found from (3.18). It indicates that for larger values of t_b, which yield larger group delays, sensitivity of group delay changes dramatically. Thus, considering an upper-bound for t_b or similarly a lower-band for κ_r, is mandatory, i.e. $\kappa_{min} \;\leq\; \kappa_r$.

Assume there is 1.5% error in adjusting transmittance coefficients of the DRR ($R = 134\mu m$, $n_{eff} = 3.46$). Using (3.19) and Fig. 3.26 one can show that for $t_r, t_b \leq 0.95$ the error in group delay changes from $-8ps$ to $0.76ps$. If the upper limit of t_r and t_b increases to 0.98 then $min[\delta\tau_{gd}] = -34.3ps$ and $max[\delta\tau_{gd}] = 1.95ps$. Therefore the upper bound must be chosen carefully.

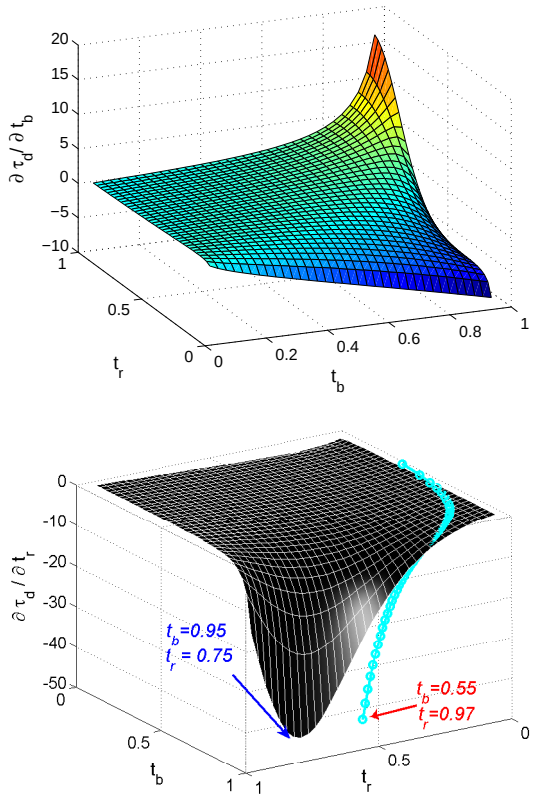

Figure 3.26: Sensitivity of the group delay for $0.015 < t_b, t_r < 0.945$. (a) w.r.t. t_b, (b) w.r.t. t_r, when $0.015 < t_b, t_r < 0.945$.

3.5.4 Time Domain Analysis

Similar to the discussions in section 3.4.2 the FDTD method was used to analyze the transient behavior of the DRR delay line. Fig. 3.27(a) displays a snapshot of the field intensity of a DRR when the full coupling from the input to the drop port has occurred. The radius of the rings and the width of the waveguide sections are ($R = 3.4\mu m$ and $w = 0.2\mu m$). The gap between the waveguide and rings is fixed at $0.25\mu m$. The resonant frequencies are calculated using the method described in Section 3.4.2. To study the transient response versus coupling, the coupling between rings was varied by changing the gap-size from $0.23\mu m$ to $0.36\mu m$. Fig. 3.27(b) illustrates the transient response of the drop channel for different coupling between rings. Ascending staircase patterns are observed and the hight of each step depends on coupling. The width of flat section of each step is given by:

$$T_S = n_{eff}\frac{2\pi R \ + \ 2w_b + \ w_r}{c} \tag{3.20}$$

Despite parallel ring resonators, in cascaded ring resonators the input and output ports are decoupled (separated), so no overshoot is observed in the early transient response.

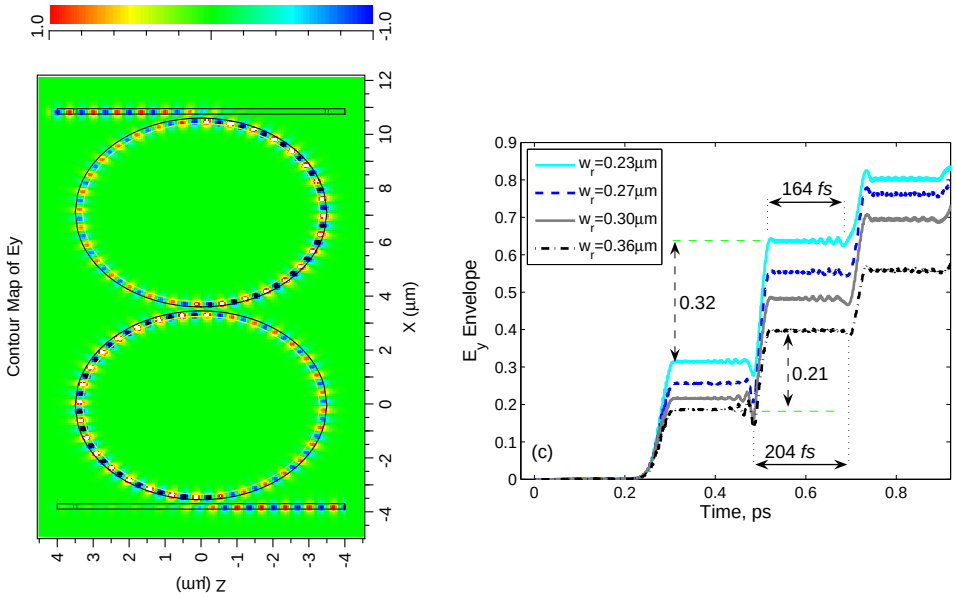

Figure 3.27: The FDTD analysis of a symmetrical DRR with $R = 3.4\mu m$. Left: a snapshot of the electric field intensity when the input CW field has been completely coupled to the drop channel. Right: the DRR transient response for different gap-sizes between rings.

3.6 Conclusion

In this chapter four types of miniaturized optical delay lines were discussed and their temporal and spectral characteristics were studied. All these ODLs can be integrated with other optical subsystems providing multiple options for optical system designers. A significant reduction in the device size makes any of these ODLs an appropriate choice for the future broadband, portable communication systems. Table 3.1 compares the delay lines discussed in this chapter.

Design and analysis of meandering delay lines in PC is one of the contributions of this thesis. It was shown that a slowing factor larger than 100 is achievable with coupled PC cavity structures. Furthermore, maximally flat group delay condition and sensitivity analysis for cascaded ring resonators presented in this chapter are useful tools to design wide-band, stable delay lines.

Fabrication of PC delay lines requires a precise technology as their feature size becomes smaller than 100nm. Although the acceleration of technology in conquering small dimensions is impressive, the realization of coupled ring resonators is easier and indeed several samples have been fabricated so far [103]. In next chapter our focus for optical beamforming will be on this type of ODLs. Another reason to pay more attention to coupled rings is the ease of tunability, for there are several methods to tune the time-delay of coupled rings.

Fabrication tolerances of coupled ring delay lines and sensitivity of the generated delay to coupling factors necessitate a robust beamforming algorithms. In case of using TO sensors to adjust the coupling factors of coupled rings, the algorithm must converge fast not to add a surplus internal delay. In next chapter we introduce a fast robust algorithm to adjust the coupling factors of coupled ring resonators.

Table 3.1: Comparison of four miniaturized optical delay lines.

Delay Line	Delay size ratio	Tunability	Bandwidth
Reflective Spiral	Moderate	Moderate	Large
Coupled Cavity	High	Low	Moderate
Parallel Rings	Moderate	Moderate	Moderate
Cascaded Rings	High	High	Low

Chapter 4

Zero-Knowledge Beamforming Algorithm

In this chapter the novel Zero-knowledge beamforming algorithm is defined [47], and its formulation is derived [124]. Next, some significant properties of this algorithm such as beamforming in motion [124], compensation for the imbalanced phase shifter loss [32], and direction-of-arrival (DOA) estimation [14, 125]are described. The remainder of this chapter introduces two optical beamforming algorithm for transmitter and receiver phased arrays, which use cascaded ring resonators as their delay element [126, 127].

There is a substantial body of research addressing the beamforming for phased array systems; however, efficient and low-complex algorithms are still needed to facilitate the utilization of phased arrays for commercial applications. An efficient beamforming algorithm is the one which compensates for the hardware inaccuracies, converges fast, reduces the steady state error, and does not add to complexity of the system significantly. In Section 1.1.4, four drawbacks of current beamforming algorithms were discussed. Moreover, in Section 2.1.3 we showed that many of the previous works on beamforming, or so called *optimum beamforming* methods, require the full knowledge of array correlation matrix. There are other algorithms that have targeted to minimize the mean received power while maintaining a nonzero fixed response in a specified direction (look direction), and place nulls in antenna patterns in the interference directions [63]– [130]. However beamforming for several applications such as mobile satellite communications, is not an interference-limited problem. In this case agility and fast convergence, robustness, and simple and low-cost implementation are the high priority tasks that must be accomplished by the algorithm.

In this chapter most of the simulations and theoretical analyses are performed for a 17-element receiver PAA. Because in next chapter the experimental results are presented for a 17-element phased array used to receive satellite signals. Also in this chapter we use the words source and satellite interchangeably. In Appendix B the satellite channel characteristics have been discussed. It is concluded that beamforming for a satellite receiver array is not an interference-limited problem. High-gain antennas used for satellite communications posses narrow beams and low sidelobe levels. The sharp spatial filtering of the satellite receiver antenna attenuates the undesired out-of-beam signals significantly. Nevertheless the beamforming algorithm proposed in this chapter can be used for a variety of applications as long as the desired signal is spatially distinguishable form in-band interferers. Hence the objective of beamforming is to *maximize* the received power or signal to noise ratio.

4.1 Zero-Knowledge Beamforming

We define Zero-knowledge beamforming as a constrained nonlinear optimization problem whose objective is to maximize the received power from a desired source. The only information about the DOA of the desired signal is that it is inside the antenna's field of view, which could be a wide region for a fan-beam antenna or a narrow region for a pencil-beam one. Despite some similarities in the form and formulation, this method is intrinsically different from the unconstrained LMS-based algorithms [38]. Unlike those algorithms, here the signal DOA and the phase-voltage characteristics of the phase shifters are unknown, thereby the algorithm directly adjusts the control voltages of the phase shifters to increase the received power level.

Fig. 4.1 shows the block diagram of a single receiver phased array antenna with N elements. After being amplified by LNAs the received signals $[s_1(t)\ s_2(t) \cdots s_N(t)]$ pass through the lossy phase shifters. The control voltages of these phase shifters are adjusted by the beamforming unit. All phase-shifted signals are combined by a power combiner, and then down-converted to an Intermediate Frequency (IF) by a mixer. The IF signal is amplified and filtered. A fraction of the IF signal enters a detector. This detector measures the instantaneous received power to provide the only available input for beamforming unit. The rise-time of this detector must be adequately fast to track the instantaneous variations of power level ($t_r = 1ns \sim 0.1\mu s$).

4.1.1 Voltage-Controlled Beamforming

As discussed in Section 2.2.3 and 2.3.1 both phase and amplitude of the array weights, w_k, depend on the control voltage of phase shifters. Hence, (2.19) can be rewritten as

$$w_k(v_k) = f(v_k).exp[j\psi(v_k)] \ . \tag{4.1}$$

Both f and ψ functions do not have exact mathematical expressions, and are found via measurements. Fig. 2.4 shows the *general behavior* of low-cost analog phase shifters. The phase function, $\psi(v)$, shown in Fig. 2.4(c) has a monotonic behavior, thus it can be approximated by a line. However, the amplitude function, $f(v)$, is nonlinear, thereby a high order polynomial ($n = 6, 7, \cdots$) must be used to approximate it. In the special case of uniform linear arrays, the received SNR in (2.16), when voltage-controlled phase shifters are used, is modified to

$$\rho = \frac{\sum_{l=1}^{N}\sum_{k=1}^{N} f(v_l)f(v_k)e^{j[\psi(v_l)-\psi(v_k)]}e^{j(l-k)u}}{\sigma_n^2 \sum_{k=1}^{N} f(v_k)^2} \tag{4.2}$$

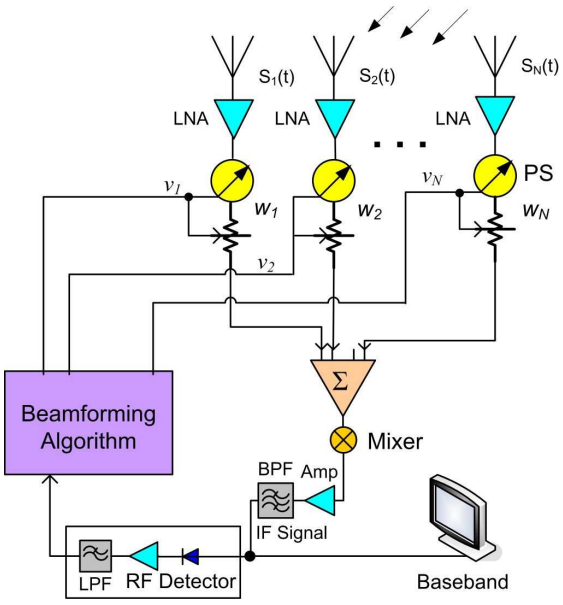

Figure 4.1: Block-diagram of a single channel receiver phased array antenna.

The above equation is a nonlinear function of control voltages. In general, the beamforming problem when practical phase shifters are used can be stated as a nonlinear optimization problem with the objective of maximizing the received power or SNR:

$$\begin{aligned} &maximize\ P = \mathbf{w}^H \mathbf{R} \mathbf{w}\ or\ \rho = \sigma_n^{-2} \frac{\mathbf{w}^H \mathbf{R}_S \mathbf{w}}{\mathbf{w}^H \mathbf{w}} \\ &subject\ to:\ \ w_k = f(v_k).\exp[j\psi(v_k)] \quad \forall k \end{aligned}$$

In the following, we propose a new approach to find the control voltages which maximize the received power.

4.1.2 Beamforming Algorithm

As long as the phase-voltage relation is monotonic and can be approximated by a linear function, the received power can be well approximated by a quadratic function around the quiescent point [63]. It is well known that the optimum solution for maximizing (or minimizing) a quadratic function can be found via an iterative process based on gradient estimation of the (cost) function w.r.t. the variables. As shown in Fig. 4.1 the only variables of Zero-knowledge beamforming problem are control voltages. So, to maximize the received power (SNR) an iterative gradient estimation method is needed to update them. In the rest of this section we find an interactive voltage update equation which is the core of the beamforming algorithm.

The criteria for selecting the algorithm parameters will be discussed in the Sections 4.2 and 4.3.

Voltage Update Equation

Let $\mathbf{v}(n) = [v_1(n)\ v_2(n)\ \cdots\ v_N(n)]$ denote the control voltages of N phase shifters at time instant n. Using steepest-descent method [131], control voltages are updated according to

$$\mathbf{v}(n+1) = \mathbf{v}(n) + 2\mu\nabla_{\mathbf{v}}P(n)\ , \tag{4.3}$$

where μ is an internal algorithm parameter called *step-size*. Also $\nabla_{\mathbf{v}}P(n)$ is the gradient of power w.r.t. $\mathbf{v}$. Since the exact calculation of the gradient is not practical it is replaced by an estimated vector:

$$\nabla_{\mathbf{v}}P(n)\ \simeq\ [\hat{g_1}(n)\ \hat{g_2}(n)\ \cdots\ \hat{g_N}(n)]\ , \tag{4.4}$$

where each component $\hat{g_k}(n)$ is the approximated partial derivative of $P(n)$ w.r.t. $v_k(n)$.

Gradient Approximation Methods

The total received power is a function of the control voltages, $\mathbf{v}$, so, it can be denoted as $P(\mathbf{v}) = P\left(v_1(n), \cdots, v_k(n), \cdots, v_N(n)\right)$. Several methods have been proposed to estimate the gradient of a multi-variable function. Among them the following three methods can be easily applied to a practical single receiver PAA system:

Method a) Sequential one-sided approximation: In this method only one perturbation is applied to estimate each component of $\nabla_{\mathbf{v}}P$, hence [47]:

$$\hat{g_k}(n) = \frac{P\left(v_1(n)\cdots, v_k(n) \pm \delta, \cdots\right) - P\left(v_1(n)\cdots, v_k(n), \cdots\right)}{\pm\delta}\ , \tag{4.5}$$

where δ, a small positive voltage called *perturbation*, is another internal algorithm parameter.

Method b) Sequential two-Sided approximation: in this method two perturbations with opposite signs are applied to determine the centered finite-difference approximation of each gradient component,

$$\hat{g_k}(n) = \frac{P\left(\cdots, v_k(n) + \delta, \cdots\right) - P\left(\cdots, v_k(n) - \delta, \cdots\right)}{2\delta} \tag{4.6}$$

This method has less power fluctuations and better steady state performance compared to Method *a* [47], however its execution time is almost twice.

Method c) Simultaneous perturbation approximation [55,132,133]: in this method all voltages are perturbed simultaneously. Let $\mathbf{D}$ be a random vector with N components, then the estimated gradient vector is given by

$$\nabla_{\mathbf{v}} P(n) = \frac{P(\mathbf{v} + c(n)\mathbf{D}) - P(\mathbf{v} - c(n)\mathbf{D})}{c(n)} \mathbf{D}^{-1} \tag{4.7}$$

where $c(n)$ plays the role of perturbation in (4.6). One method to generate vector $\mathbf{D}$ is to use a sequence of random numbers with Bernoulli distribution with probability of 0.5. By proper adjustment of the parameters, beamforming with this method might have the same performance as the sequential two-sided method [132]- [133]. As the number of phase shifters increases, sequential methods are prolonged while the speed of simultaneous method is not affected significantly. However, the algorithm usually requires more iterations to converge.
For a detailed comparison of these three methods please see [47] and [133].

In this work we use the sequential two-sided method to estimate the gradient of the received power. Thus the beamforming algorithm has only two internal parameters:*step-size* μ and *perturbation* δ. In the next section we show how proper selection of these two parameters can reduce the noise effect.

4.2 Effects of Receiver Noise on Gradient Estimation

In an ideal situation the output of power detector in Fig. 4.1 must be a DC signal. However, due to noise, multipath, interference from other active sources, and mobility of the platform the received power has a spread spectrum, and accordingly fluctuations in time domain. Since gradient estimation is sensitive to the measured power level it is mandatory to smooth these fluctuations before running the beamforming algorithm. Moreover, the appropriate selection of the algorithm parameters can suppress the undesired power variations. In this section the effect of noise on the estimated gradient and updated voltages of a *stationary* array is studied, and the guidelines to select the algorithm parameters are discussed. In next section the proper parameters for a *mobile* array are derived.

4.2.1 The Relations between Algorithm Parameters and Noise

Consider a Gaussian noise, $n_m(t)$ called measurement noise with zero mean and variance σ^2 added to the received power (Fig. 4.2(a)). The noisy estimate of the gradient in (4.6), denoted by $\widetilde{g}$, is

$$\widetilde{g_k} = \frac{[P(v_1, \cdots, v_k + \delta, \cdots) + n_{m1}] - [P(v_1, \cdots, v_k - \delta, \cdots) + n_{m2}]}{2\delta}$$
$$= \frac{P(v_1, \cdots, v_k + \delta, \cdots) - P(v_1, \cdots, v_k - \delta, \cdots)}{2\delta} + \frac{n_{m1} - n_{m2}}{2\delta} = \hat{g_k} + \widetilde{n}_g(t) \quad (4.8)$$

where n_{m1} and n_{m2} are two samples of $n_m(t)$. Additionally, $\widetilde{n}_g(t)$ called the gradient estimation noise is a zero mean Gaussian noise with the variance of $\sigma^2/2\delta^2$. Equation (4.6) proposes that by reducing perturbation, the accuracy of gradient estimation increases. However, for small values of δ, i.e. $\delta < \sigma/\sqrt{2}$, the gradient estimation noise becomes stronger than the measurement noise, $n_m(t)$. Thus small values of δ must be avoided. Fig. 4.3 shows the results of the beamforming for a planar array of 17 elements (the description of the array will be given in Section 5.1). It illustrates that for the same SNR and step-size values increasing δ improves the steady state performance of the algorithm. However, further increase of δ deteriorates the gradient approximation in (4.6), because the second derivative of power w.r.t. voltage cannot be ignored for a large δ.

If we replace $\hat{g_k}$ in the voltage update equation (4.3) with $\widetilde{g_k}$, the updated voltage becomes noisy. The noisy update voltage, $\widetilde{v_k}(n+1)$, is thus

$$\widetilde{v_k}(n+1) \;=\; v_k(n+1) \;+\; n_u(t) \quad (4.9)$$

In the above equation $\widetilde{v_k}(n+1)$ and $v_k(n+1)$ differ in a noise term denoted by $n_u(t)$ equal to $2\mu\widetilde{n}_g(t)$ (see Fig. 4.2(b)). Added to the phase shifter control voltage, this noise affects the received power level. Hence the noisy estimated gradient in (4.8) must be modified to

$$\widetilde{g_k} \;=\; \frac{P(v_1, \cdots, v_k + \delta + n_1, \cdots) - P(v_1, \cdots, v_k - \delta + n_2, \cdots)}{2\delta} + \widetilde{n}_g(t) \quad (4.10)$$

where n_1 and n_2 are two samples of $n_u(t)$. Denoting $P(v_1, \cdots, v_k \pm \delta + n_1, \cdots)$ by $P(v_k \pm \delta + n_u)$, we write the Taylor series expansion for the received power

$$P(v_k \pm \delta + n_u) = P(v_k) + P'(v_k)(\pm\delta + n_u) + \frac{1}{2!}P''(v_k)(\pm\delta + n_u)^2 + ... \quad (4.11)$$

Replacing (4.11) in (4.10), the noisy estimated gradient $\widetilde{g_k}$ is evaluated as

$$\widetilde{g_k} = \widetilde{n}_g(t) + P'(v_k)\left[1 + \frac{n_1 - n_2}{2\delta}\right] + \frac{1}{4}P''(v_k)[n_1 - n_2 + \frac{n_1^2 + n_2^2}{2}] \;+\; ... \quad (4.12)$$

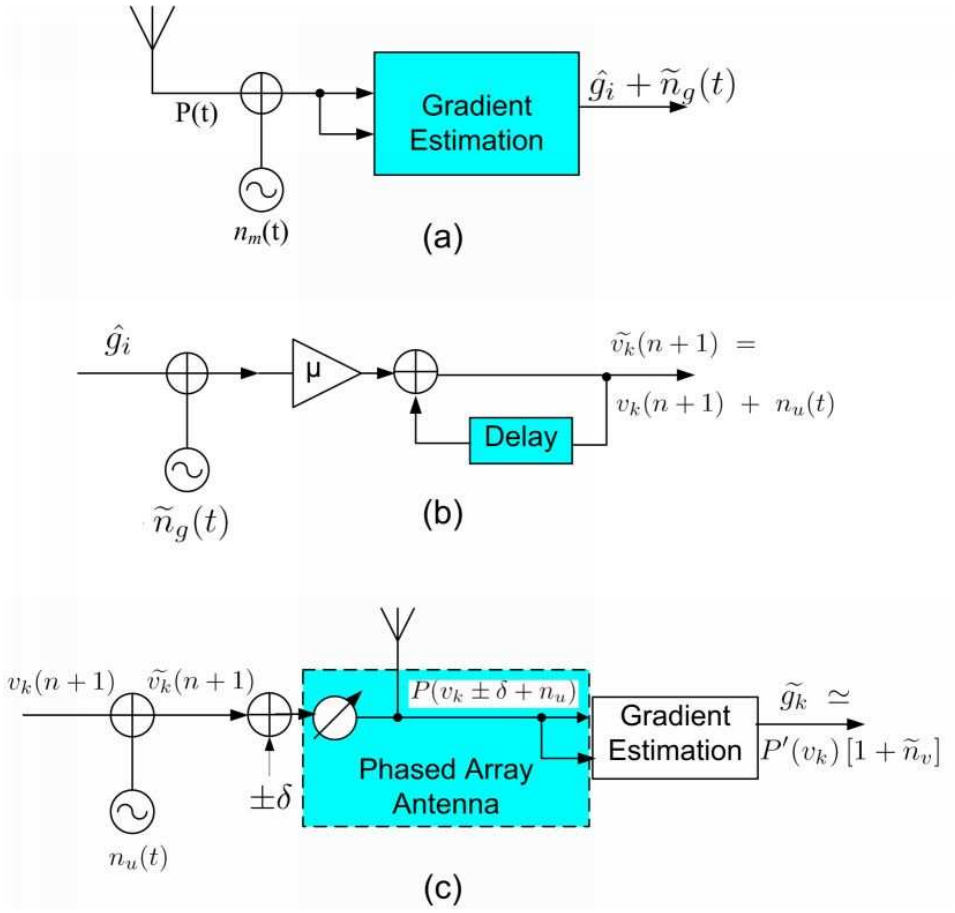

Figure 4.2: Noise model for beamforming algorithm. (a) Measurement noise. (b) Voltage update noise. (c) Gradient estimation noise.

It is a reasonable assumption that the second derivative diminishes as the algorithm reaches its steady state, so the last term in the above equation can be ignored. The noisy estimated gradient as seen in Fig. 4.2(c) is thus

$$\widetilde{g_k} \;\simeq\; P'(v_k)\,[1+\widetilde{n}_v] \;\; + \widetilde{n}_g(t),$$

where $\widetilde{n}_v$ denotes a zero mean Gaussian noise with the variance of $(\mu\sigma/\delta^2)^2$. For a fixed σ/δ^2 ratio, decreasing μ diminishes the effect of the voltage updating noise. Fig. 4.4 shows the results of two beamforming simulations for the 17-element array with SNR=20dB, $\delta = 0.61$, and two different step-sizes. This value of SNR reflects the measured SNR after power detector and low-pass filtering in Fig. 4.1 which belongs to a very narrow spectrum. It is seen that for the smaller μ the algorithm has converged to 85% of the maximum power, whereas for the larger μ the received power is not higher than 70%.

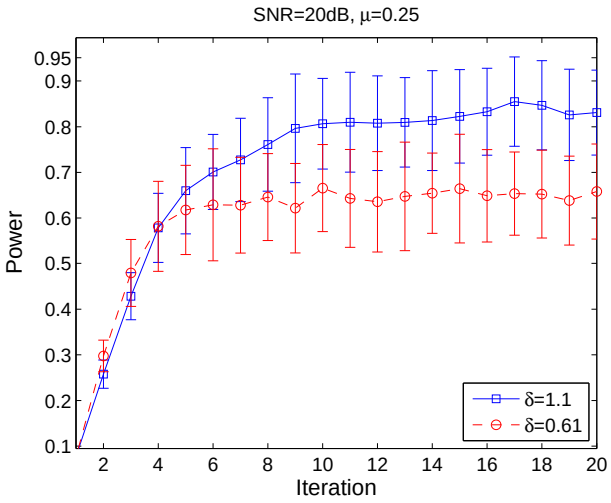

Figure 4.3: The effect of perturbation (δ) on the received power for SNR=20dB and $\mu = 0.25$. The algorithm has been run 50 times and the error-bars show the standard deviations.

4.2.2 Noise Filtering

Analog RC filters are low-cost choices to eliminate high frequency contents of the signal. However there is a large degree of flexibility in designing digital filters such as Elliptic, Sinc and Finite Impulse Response (FIR) filters [134]. Discussing the advantages and disadvantages of different digital filters is beyond the purpose of this work.

Fig. 4.5 illustrates the impact of filtering on the received power. Here, an 8-point FIR filter with Hamming coefficients is used. The algorithm parameters are set to $\mu = 0.05$, and $\delta = 1.1$, the proper values found in the previous section. It is seen that the performance of the algorithm for SNR=10dB with filtering is similar to the case where SNR is 20dB but without filtering. For an N-point low-pass FIR filter it can be shown that

$$SNR_F = SNR_0 \times 10 \log_{10} N \tag{4.13}$$

where SNR_0 and SNR_F are signal to noise ratios before and after filtering, respectively. However digital filtering slows the beamforming process as more samples are required to measure the power level. The ADC speed has a significant contribution in the total beamforming speed.

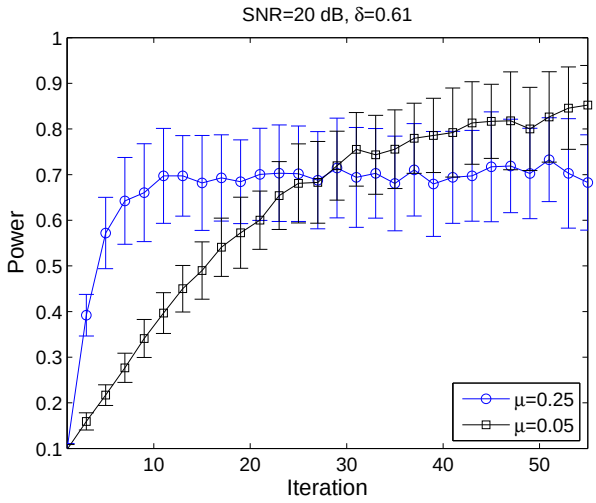

Figure 4.4: The effect of step-size (μ) on the received power for SNR=20dB and $\delta = 0.61$. The algorithm has been run 50 times and the errorbars show the standard deviations.

4.3 Beamforming in Motion

The limits found for step-size and perturbation in the previous section are valid for a stationary array, where the mean input power level is constant versus time. In that analysis, achieving a high steady state level was the main goal. Nevertheless, for a mobile array fast convergence of beamforming process is more important.

The received power by a linear array with N identical elements and ideal phase shifters (no insertion loss) is given by:

$$P(n) = \left| \sum_{k=1}^{N} \exp\left[-j\psi_k(n) + jk_0 x_k \sin\theta(n)\right] \right|^2 \tag{4.14}$$

where x_k and ψ_k respectively denote the position and the applied phase shift to the k^{th} element, and $\theta(n)$ is the source angle relative to array normal. For a stationary array, the phase of the received signal is constant because $\theta(n) = \theta_0$. Thus, beamforming algorithm adjusts all array weight, $\psi_k(n)$, to maximize the received power $P(n)$. It may take a few iterations to reach the steady states, where $P(n)$ converges to the proximity of N^2 and the phase-shift variations become zero, i.e.

$$\psi_k(n) \;\simeq\; k_0 x_k \sin\theta_0 \quad \forall k \tag{4.15}$$

Zero-knowledge algorithm calculates $\psi_k(n)$ weights based on the power measurements at the previous time instant $n-1$. Thus, for a mobile array, where $\theta(n)$ is varying, the algorithm always lags the target movements. Consequently, the phase

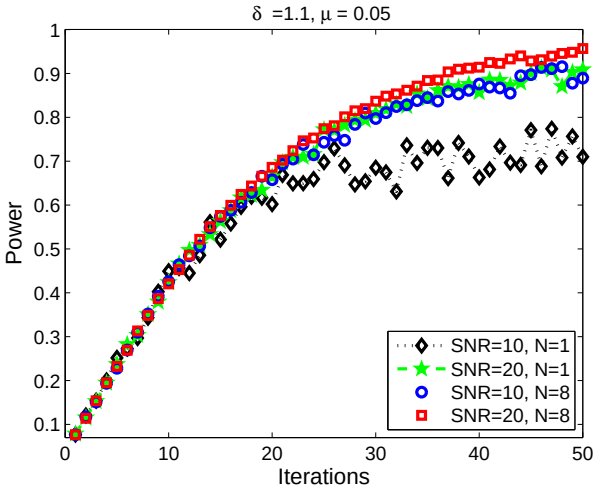

Figure 4.5: The impact of noise filtering on the received power for different SNR values at the array output. Each curve shows the mean value of 50 runs of the algorithm.

differences differ from zero which causes a power level drop. A *fast beamforming* algorithm is the one which minimizes this level drop. The convergence time or the execution time of the algorithm, ΔT must be adequately short to enable tracking of fast target movements without a significant level drop. In this case the target location at the time instant n can be approximated with a linear function of the angular velocity at $n-1$

$$\theta(n) \simeq \theta(n-1) + \dot{\theta}(n-1)\Delta T \tag{4.16}$$

If fast rate sensors with high sampling rates were available one could estimate the target location at the next iteration and adjust the weights, but there are two problems compelling us to look for a fast beamforming technique:

1. The convergence/execution time of the algorithm is usually several times faster then the sampling interval of the low-cost rate sensors, thus suspension of beamforming causes a large power drop or misses the target.

2. Zero-knowledge beamforming is a feedback aided method which assumes no *a priori* knowledge of the phase shifters, so the phases cannot be adjusted in advance to steer the beam to the predicted position.

4.3.1 Fast Beamforming Condition

To figure out how beamforming parameters must be chosen for fast convergence, consider a uniform N-element linear phased array. The necessary condition for fast

convergence in a mobile scenario is given by

$$|\psi_k(n+1) - k_0 x_k \sin\theta(n)| \;\ll\; 1 \tag{4.17}$$

The above relation implies that the array weights applied at $n+1$ must compensate for the received signal phases at n. If (4.17) is not satisfied the phase difference accumulates, and consequently the power level decreases due to the destructive interference. Assume array wights are directly updated based on a gradient estimation method

$$\psi_k(n+1) = \psi_k(n) + 2\mu_\psi \hat{g_k}(n) \tag{4.18}$$

Two power measurements are required to estimate the k^{th} component of the gradient vector, $\hat{g_k}(n)$,

$$\hat{g_k}(n) = \frac{P(\psi_1(n), \cdots, \psi_k(n) + \delta_\psi, \cdots) - P(\psi_1(n), \cdots, \psi_k(n) - \delta_\psi, \cdots)}{2\delta_\psi} \tag{4.19}$$

where δ_ψ is the perturbation in phase applied to estimate the gradient. It is assumed that the array motion during this process is negligible. The measured (received) power for gradient estimation can be expressed as

$$P(\psi_1, \cdots, \psi_k \pm \delta_\psi, \cdots) \;=\; |U_\pm \;+\; M|^2 \tag{4.20}$$

where

$$U_\pm \;=\; \exp(\mp j\delta_\psi).\exp[-j\psi_k(n) + jk_0 x_k \sin\theta(n)] \tag{4.21}$$

and

$$M \;=\; \sum_{m\neq k}^{N} \exp[-j\psi_m(n) + jk_0 x_m \sin\theta(n)] \tag{4.22}$$

So $P(\psi_1, \cdots, \psi_k \pm \delta_\psi, \cdots)$ is equal to

$$P(\psi_1, \cdots, \psi_k \pm \delta_\psi, \cdots) = (U_\pm \;+\; M).(U_\pm^* \;+\; M^*) \tag{4.23}$$

Substituting (4.23) in (4.19), after further simplification $\hat{g_k}(n)$ is calculated as

$$\hat{g_k}(n) = \frac{MU_+^* + M^*U_+ - MU_-^* - M^*U_-}{2\delta_\psi} \tag{4.24}$$

$$= \frac{M(U_+^* - U_-^*) + M^*(U_+ - U_-)}{2\delta_\psi} \tag{4.25}$$

Using (4.21) the above expression for $\hat{g_k}(n)$ can be rewritten as

$$\hat{g_k}(n) = \frac{M(\exp[j\psi_k(n) - jk_0 x_k \sin\theta(n)]) - M^*(\exp[-j\psi_k(n) + jk_0 x_k \sin\theta(n)])}{2\delta_\psi} \times(2j\sin\delta_\psi) \tag{4.26}$$

which can be simplified to

$$\hat{g_k}(n) \;=\; \frac{2\sin(\delta_\psi)}{\delta_\psi}\Im[X] \tag{4.27}$$

where $\Im[X]$ denotes the imaginary part of X defined as

$$X \;=\; M\exp\left[j\psi_k(n) - jk_0x_k\sin\theta(n)\right] \tag{4.28}$$

The fast convergence condition, given in (4.17), necessitates that $\psi_m(n) \approx k_0x_m sin\theta(n-1)$, so

$$\exp\left[-j\psi_m(n) + jk_0x_m\sin\theta(n)\right] \approx \exp\left[jk_0x_m\left(\sin\theta(n) - \sin\theta(n-1)\right)\right] \tag{4.29}$$

The location of the k^{th} element in a linear array is given by

$$x_k \;=\; [k - (N+1)/2]d. \tag{4.30}$$

Combining (4.29) and (4.30), we obtain

$$\exp\left[-j\psi_m(n) + jk_0x_m\sin\theta(n)\right] \approx \exp\left[j\gamma(n)\left(m - (N+1)/2\right)\right] \tag{4.31}$$

where

$$\gamma(n) \;=\; k_0d[\sin\theta(n) - \sin\theta(n-1)] \tag{4.32}$$

Using the above equation, M in (4.22) can be rewritten as

$$M \;=\; \sum_{m=1}^{N}\exp\left[j(m - \frac{N+1}{2})\gamma(n)\right] \;-\; \exp\left[j(k - \frac{N+1}{2})\gamma(n)\right] \tag{4.33}$$

Using (4.33), X in (4.28) can be found:

$$X \;=\; \exp\left[-jk\gamma(n)\right]\sum_{m=1}^{N}\exp[jm\gamma(n)] - 1 \tag{4.34}$$

The summation in (4.34) represents a geometric series, so it is equal to

$$\sum_{m=1}^{N}\exp[jm\gamma(n)] \;=\; \frac{\exp[j\gamma(n)] - \exp[j(N+1)\gamma(n)]}{1 - \exp[j\gamma(n)]} \tag{4.35}$$

Using (4.35) and trigonometric identities, X in (4.34) can be calculated as

$$X \;=\; \exp\left[j(\frac{N+1}{2} - k)\gamma(n)\right]\frac{\sin[N\gamma(n)/2]}{\sin[\gamma(n)/2]} - 1 \tag{4.36}$$

Thus, the imaginary part of X is

$$\Im[X] \;=\; \sin\left[(\frac{N+1}{2} - k)\gamma(n)\right]\frac{\sin[N\gamma(n)/2]}{\sin[\gamma(n)/2]} \tag{4.37}$$

Finally, the k^{th} component of the estimated gradient in (4.27) will be

$$\hat{g_k}(n) \;=\; 2\frac{\sin\delta_\psi}{\delta_\psi}\sin[(\frac{N+1}{2} - k)\gamma(n)]\frac{\sin[N\gamma(n)/2]}{\sin[\gamma(n)/2]} \tag{4.38}$$

4.3.2 Nonuniform Step-size

To satisfy the fast convergence condition for a linear array given in (4.17), the Zero-knowledge beamforming algorithm at time $n+1$ must compensate for the angular motions between $n-1$ and n, thus

$$\psi_k(n+1) - \psi_k(n) = k_0 x_k[\sin\theta(n) - \sin\theta(n-1)] \tag{4.39}$$

The left–side of (4.39) is the difference in the applied phase–shifts at n and $n-1$. From (4.18) it is concluded that

$$\psi_k(n+1) - \psi_k(n) = 2\mu_\psi \hat{g}_k(n) \tag{4.40}$$

Equating the right-sides of (4.39) and (4.40) we have

$$\mu_\psi\,[2\hat{g}_k(n)] = x_k\,\{k_0[\sin\theta(n) - \sin\theta(n-1)]\} \tag{4.41}$$

Replacing $\hat{g}_k(n)$ with (4.38) we find that for each k, the step-size μ_ψ in (4.41) must be proportional to the element location x_k to satisfy this equation. Thus

$$\begin{aligned} \mu_k = \left[\frac{\delta_\psi}{4\sin\delta_\psi}\frac{\sin(\gamma(n)/2)}{\sin[N\gamma(n)/2]}\right]\frac{\gamma(n)x_k/d}{\sin[(\frac{N+1}{2}-k)\gamma(n)]} \\ \gamma(n) = k_0 d(\sin\theta(n) - \sin\theta(n-1)) \end{aligned} \tag{4.42}$$

For relatively fast beamforming $\gamma(n)$ depends on the angular velocity and the execution time of the algorithm through the following relation

$$\gamma(n) = k_0 d\ \Delta T\dot{\theta}(n-1)\cos\theta(n-1) \tag{4.43}$$

Hence the following conclusions are extracted for a mobile array:

- μ_k depends on the element location, x_k.
- μ_k increases with the angular speed of the array.
- μ_k decreases if the beamforming speed increases.
- μ_k increases with the phase perturbation δ_ψ (because $\sin(\delta_\psi) \leq \delta_\psi$).

In the extreme case when $\dot{\theta} \to 0$ the step-size μ_k becomes independent of the element locations. We refer to this special case as uniform step-size situation ($\mu_k = \mu_0,\ \forall k$).

4.3.3 Advantage of Beamforming with Nonuniform Step-size

To study the merit of employing nonuniform step-size for beamforming, consider a mobile linear array of 12 elements with 5λ spacing. For many applications such as satellite communications, each element of the phased array is a high-gain sub-array. Thus, the sub-array size could be several wavelengths to meet the gain requirements (see Section 5.1). The array is rotated with a relative angular velocity of $\dot{\theta} = 40\sin(2\pi/5\ t)\ ^\circ/s$. This angular velocity simulates an accelerating fast maneuver during a short period of time. At $t = 0$ the array is located at $\theta(0) = 100^\circ$. The received SNR is 20dB, and $N_{FIR} = 8$. First, we assume the execution time of the algorithm (ΔT) is $10ms$. The curve R1 in Fig. 4.6(a) (the dashed line) shows the mean value of the received power for 100 runs of beamforming with uniform step-size. When the angular speed is relatively low ($0 \leq t \leq 0.25s$), the beamforming algorithm converges to 92% of the maximum power. However, as the time passes the power level drops to below 65%. In the curve R2 (the solid line) step-size depends on the element location. The mean power level improves by 3% compared to R1. In the curve R3 (dotted line) the step-size depends on both the element position and the angular speed. The overall performance of R3 is 5.1% better than that of R1. The curve R4 is similar to R3 but the algorithm is two times faster ($\Delta T = 5ms$). In this case the average power level is 16.4% better than R1.

These simulations reveal that using nonuniform step-size improves the beamforming performance of a mobile linear array. If the angular velocity of the array platform is known the improvement is enhanced. Also it was shown that increasing the beamforming speed has a significant effect on the received power. However, this requires a revision in the processor and hardware design. Thus, use of nonuniform step-size is a low-cost solution for a better performance. In Section 5.4 experimental results for beamforming in motion are presented.

4.4 Non-Co-phased (Noncoherent) Beamforming

In Section 2.3.1 it was shown that the imbalanced insertion loss is a drawback of low-cost analog phase shifters. In this section we show that Zero-knowledge beamforming perturbs phase-coherency to obtain a larger received power [32].

Based on the maximum array gain theorem when all elements are identical, coherent beamforming gives the maximum gain (power) [62]. Let $\phi_k(n)$ denote the

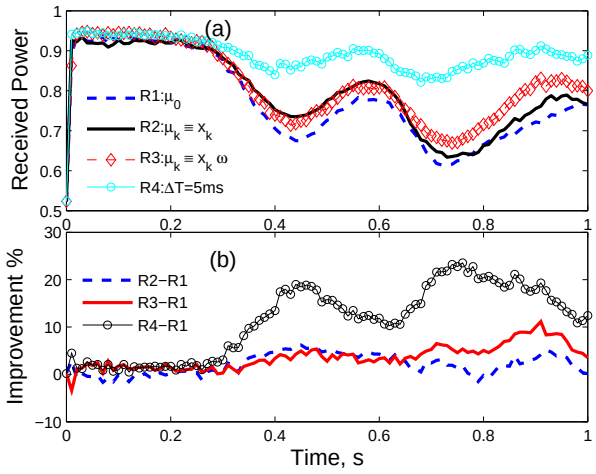

Figure 4.6: Comparison of beamforming with different step-size options for a mobile linear array. Each curve represents the mean value of 100 runs of the algorithm. R1: uniform time-invariant step-size $T_s = 10ms$, R2: nonuniform time–invariant step-size $T_s = 10ms$, R3: nonuniform time–variant $T_s = 10ms$, and R4: nonuniform time–variant step-size with $T_s = 5ms$ (a) Normalized received power versus time, (b) Improvement percentage.

phase of the received signal by the k^{th} element, then for *coherent* beamforming the received power is

$$\begin{aligned} P_{Coh}(n) &= P(\phi_1(n), \cdots, \phi_N(n)) \\ &= \left| \sum_{k=1}^{N} f(\phi_k(n)) \right|^2 \end{aligned} \tag{4.44}$$

Provided that phase shifters are lossless ($f(\phi_k(n)) = 1$), the coherent power is equal to N^2. However, when phase shifters suffer from imbalanced IL, coherent beamforming does not necessarily yields the maximum power. Suppose the coherency condition is violated, thus for each element of the array, the applied phase shift will be

$$\psi_k(n) = \phi_k(n) + \xi_k(n) \tag{4.45}$$

where $\xi_k(n)$ is the added noncoherency. The noncoherent or non-co-phased received power is then

$$\begin{aligned} P_{Non}(n) &= P(\phi_1(n) + \xi_1(n), \cdots, \phi_N(n) + \xi_N(n)) \\ &= \left| \sum_{k=1}^{N} f(\phi_k(n) + \xi_k(n)) e^{-j\xi_k(n)} \right|^2 \end{aligned} \tag{4.46}$$

Fig. 4.7 compares the results of coherent and noncoherent beamforming for the 17-element array when the satellite is located at $(\theta, \phi) = (18°, 18°)$ and the array

is stationary. First, the required coherent phase shifts were calculated and the phase shifters were adjusted to generate these values. The received power for these initial values was 53% of P_{max}. Next, the Zero-knowledge beamforming algorithm was run for 75 iterations to update the control voltages of the phase shifters. The characteristics of all phase shifters are identical to the one shown in Fig. 2.4. The algorithm parameters were set to $\mu = 0.1$, $\delta = 0.3$ and SNR=32dB[1]. Fig. 4.7(a) shows that at the end of beamforming the received power has increased by 16.5%. Fig. 4.7(b), and (c) compare the phases and insertion loss of all phase shifters before and after beamforming. It is evident that the insertion loss of the phase shifters has significantly reduced after beamforming, with the price of perturbing the coherency.

Hence, Zero-knowledge beamforming algorithm is a non-co-phased (non-coherent) method. It increases the total received power when phase shifters suffer from imbalanced insertion loss. This is a great step toward a low-cost phased array.

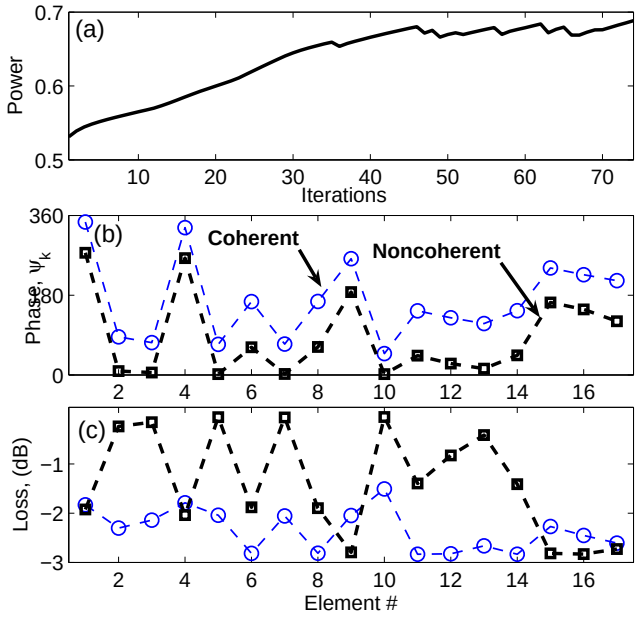

Figure 4.7: Co-phased and non-co-phased beamforming results for the 17-element phased array when the satellite is at $(\theta, \phi) = (18°, 18°)$ relative to normal. (a) Learning curve of the normalized power for 75 iterations, (b) Coherent and Noncoherent phase shifts, and (c) insertion loss for all phase shifters.

[1]As it will be shown in Chapter 5 the experimental measurements reveal that the received SNR by the 17-element phased array from a broadcasting satellite is around 31–32dB

4.5 Direction of Arrival Estimation

A mobile phased array system needs a stabilization loop to compensate for the platform motions and keep the array locked on the desired source/target. The low-cost inertial sensors such as MEMS gyro suffer from high rate–drift and strong noise. These defects can deflect the antenna heading from the desired direction. Moreover, some slow angular motions of the mobile platform are even hidden in the sensor noise. As a result, the stabilizing loop takes no action against such disturbances. Gradually, the array is deflected and a complete signal outage may occur.

In this section a novel Direction of Arrival (DOA) estimation algorithm is developed to eliminate the effects of the sensor irregularities [14, 125]. Fig. 4.8 displays the functional block-diagram of the proposed DOA estimation algorithm. Zero-knowledge beamforming finds the voltages that maximize the received power. The DOA estimation unit uses these voltages, the measured power and a database to find the signal DOA. Then it fine-tunes the antenna direction if deviated from the desired source through sending proper Left/Right command to motor. The algorithm takes advantage of the exclusive property of the PAA to steer the beam electronically. Mechanical adjusting methods such as conical scanning require to rotate the antenna permanently. Hence, they cause fluctuations (and power drop) in the received signal level and reduce the durability of motor [135]– [136]. Despite such mechanical methods, this DOA estimation technique does not move the array. Thus it saves the motor and battery life and does not add to the system cost and complexity.

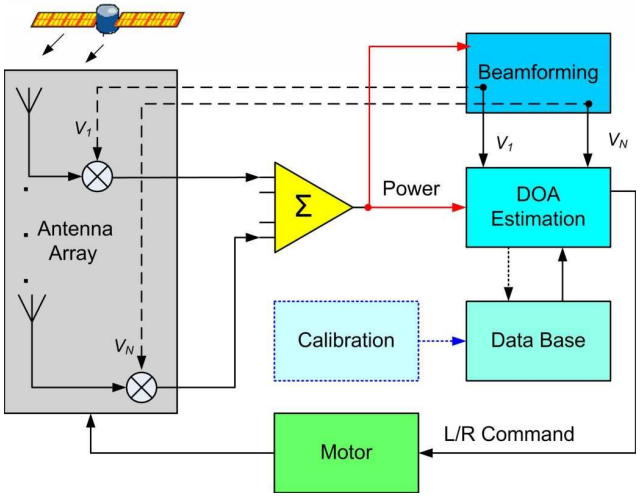

Figure 4.8: Functional block-diagram of the DOA estimation algorithm.

4.5.1 Theory

Fig. 4.9 shows a simplified array of three elements. If incoming wave-front makes angle θ with array normal, there is a phase lag between the antenna elements given by (2.18)

$$\phi_1 - \phi_2 = \phi_2 - \phi_3 = 2\pi \frac{d \sin\theta}{\lambda}$$

If all phase shifters were identical and there was a linear relation between their phase and control voltage ($V = K_0\phi$) then

$$V_1 - V_2 = 2\pi K_0 \frac{d \sin\theta}{\lambda} \tag{4.47}$$

Equation (4.47) indicates that the source DOA can be found by comparing the adjacent voltages, thus

$$\theta \;=\; \sin^{-1}\left[\frac{\lambda \Delta V}{2\pi K_0 d}\right] \tag{4.48}$$

where $\Delta V = V_1 - V_2 = V_2 - V_3$. However, as discussed in Section 2.3 the assumptions of having identical phase shifters and linear phase-voltage relation are not valid practically. Thus knowing the voltage differences is not sufficient to find the signal DOA. One way to overcome the fabrication tolerances of the phase shifters is to find a reference voltage for each phase shifter. The reference voltages are those corresponding to a perfect beam pointing such that the geometrical axis of the antenna array is accurately directed towards the satellite. Hence, instead of comparing the absolute value of control voltages, one can compare their differences with their references, $\Delta V_i = V_i - V_{REF,i}$. In next part a training test to find these reference voltages is proposed. A satellite receiver phased array is taken as an example to explain the test procedure.

4.5.2 Training Test

For a satellite receiver phased array, a simple training test can be run during the last step of the satellite acquisition phase to find the reference voltages. The mission of the acquisition phase is to bring the phased array to the close vicinity of the desired satellite. This test can be integrated in the initial calibration process shown in Fig. 4.8. During this test, PAA is rotated mechanically around the satellite direction in fine angular steps. The electronic beamforming is performed for each mechanical step. The received power level and the final control voltages of each step are recorded. At the end of this calibration process, the voltages resulted in the highest power level are reported as the reference voltages to the DOA algorithm, thus

$$V_{REF,i} = V_i(\theta_0)|_{P(\theta_0)=P_{max}} \tag{4.49}$$

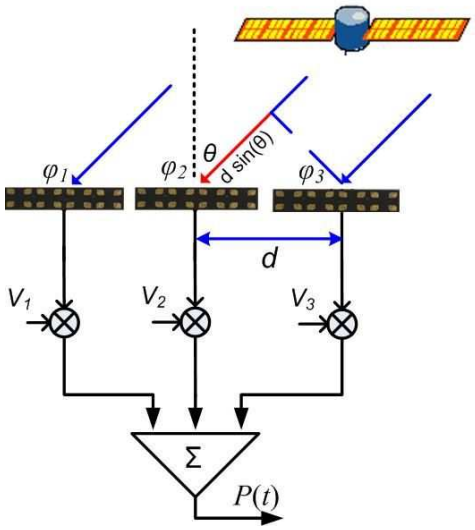

Figure 4.9: Simplified model of a phased array antenna with 3 elements.

Fig. 4.10 shows the experimental result of a training test applied to 3 elements of the 17-element phase array antenna described in Section 5.1. The control voltage of the middle element, V_{mid}, is fixed (at 6.1 volt in this case). After the approximate position of the satellite was announced a local search is performed to find the exact position of the satellite. First, the array is turned in CCW direction to -2.1° of the approximate satellite position. Then it is rotated in 15 CW angular steps to scan 4.2° in azimuth. For each step the beamforming algorithm is run for 50 iterations and the final voltages are recorded. The beamforming process repeats 50 times to reduce the noise effect, so at last 50 sets of final voltages will be available for each antenna position. The received power peaks at $\theta = 0°$, so the values of V_1 and V_3 at this position are picked for the reference voltages $V_{REF,1}$ and $V_{REF,3}$. Since the phase shifters are not identical the cross-point voltage is different from V_{mid}. The slope of V_1 is negative in accordance to (4.47)–(4.48). The reverse is true for V_3.

4.5.3 Decision Rules

Having found the reference voltages, the difference voltages (ΔV_i) are formed and compared to a voltage margin V_{Mar} to find the relative DOA. A voltage margin is necessary because of the existence of noise and disturbance during beamforming process. Based on the results shown in Fig. 4.10, the following rules can be extracted for the three-element array (Fig. 4.9):

1. The source (satellite) is on the right side of the array normal if

$$\begin{cases} \Delta V_1 > V_{Mar} \\ \Delta V_3 < -V_{Mar} \end{cases} \tag{4.50}$$

2. The source is on the left side of the array normal if

$$\begin{cases} \Delta V_1 < -V_{Mar} \\ \Delta V_3 > V_{Mar} \end{cases} \tag{4.51}$$

3. Otherwise, the source is located along the array normal.

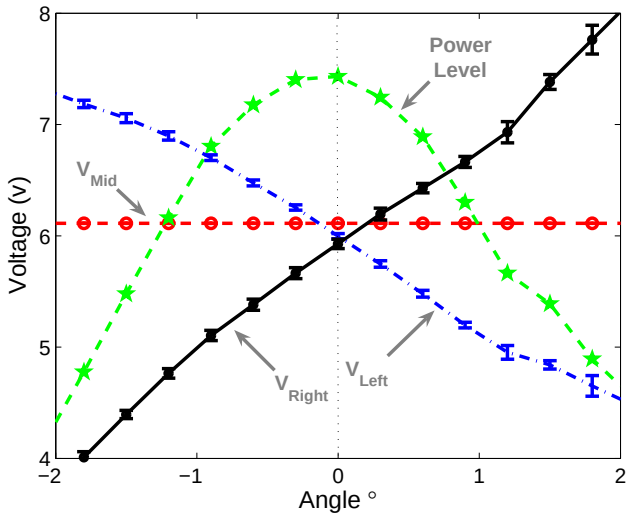

Figure 4.10: The power level and final voltages of the calibration process.

4.5.4 Implementation of DOA Estimation Algorithm

The above rules constitute the core of the DOA estimation algorithm. After running the training test the reference voltage of each element and the maximum received power, P_{max}, are stored in the database shown in Fig. 4.8. When phased array is in service, the received power level, P(t), is continuously monitored. If it drops below a threshold, i.e. P(t) $< \gamma P_{max}$ and $0.9 < \gamma < 1$, the beamforming algorithm starts to update the voltages. This threshold is determined by the quality of the baseband signal. If the power level increases after beamforming, the DOA algorithm will start comparing the current voltages with the references to determines whether the satellite is on the left side or the right side of the array normal. Next, the proper command (L/R CMD) will be send to motor. A lower bound for the voltage margin in (4.50) and (4.51) is $V_{Mar} \simeq 2\sigma_n$, where σ_n is the standard deviation of the received noise at the array output. If during the beamforming process the measured output power exceeds the recorded value for P_{max}, i.e. $P(t) > P_{max}$, the database will be updated and the current voltages replace the reference voltages.

From Fig. 4.10, it is seen that the angular distance between the array normal and the satellite increases with the difference between V_{Left} and V_{right}. We can also approximate the slope of the training curves. Hence the proposed algorithm not only estimates the direction of the radiating source, but it can measure the angular deflection form the array normal with a certain accuracy.

This algorithm has been successfully implemented in the Ku-band satellite receiver phased array system as a part of its hybrid tracking loop [14]. The experimental results will be presented in Section 5.5.

4.6 Optical Beamforming Algorithms

In this section two beamforming algorithms are developed for transmitter and receiver phased arrays. The simulation results will be presented in next section. Any of the parallel or cascaded ring resonator delay lines discussed in Sections 3.4 and 3.5 can be used with these algorithms. However in this work PRR and DRR delay lines are respectively used for the transmitter and receiver phased arrays.
The coupling coefficients between rings and waveguide are chosen as the algorithm variables. It is assumed that the relation between temperature and coupling factor is known, so the coupling factors can be adjusted to the desired values. Each algorithm starts with the initial conditions for coupling factors and continues to update them based on a gradient estimation method. This process is repeated until one of the termination conditions of the algorithm is satisfied. The practicality of these algorithms will be discussed in Section 4.8.

4.6.1 Optical Beamforming Algorithm for Transmitter Phased Array

Fig. 4.11 demonstrates the proposed optical beamforming network for a transmitter PAA [126]. The RF signal (information) modulates an optical carrier whose wavelength can be determined by the beamforming algorithm. Fullwave analysis of parallel rings reveals that the coupling factor and delay depend on wavelength. In lack of a multi-wavelength laser a single monochromatic laser can be used for all delay lines with the price of less flexibility in adjusting the coupling factors. The optical signal propagates through PRR. Beamforming algorithm adjusts the coupling factors through changing the bias of the TO phase-shifters. A photodiode (PD) per channel demodulates the RF signal and delivers it to the Directional Coupler (DC). A fraction of the delayed signal is used for time-delay measurement and the rest is amplified and transmitted by the antenna. One way to measure the

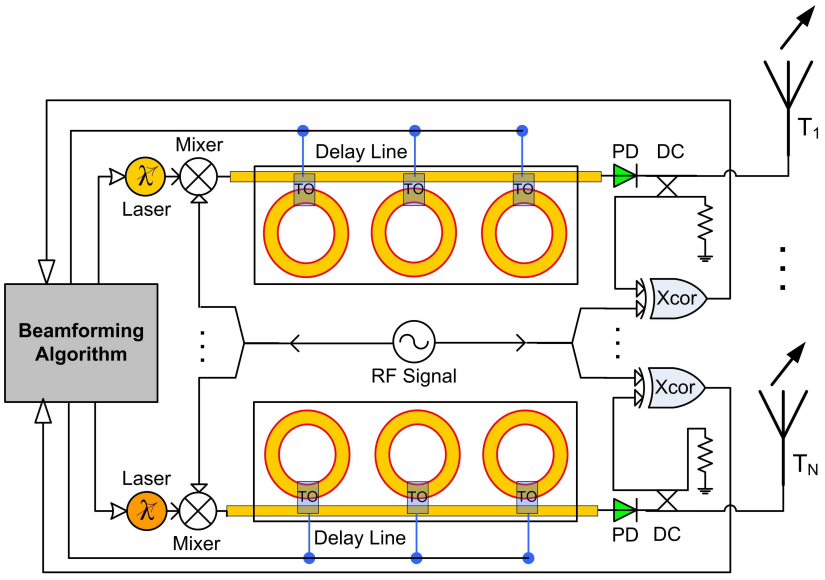

Figure 4.11: Block-diagram of a transmitter phased array with PRR delay lines incorporated in its optical beamforming network.

time-delay is to find the cross correlation of the delayed signal and the modulating RF signal [137]. If $x_1(t) = s(t) + n_1(t)$ denote the modulating signal plus noise, the delayed signal after DC is

$$x_2(t) = ks(t - \tau_d) + n_2(t) \tag{4.52}$$

where $k < 1$ is a constant, and $s(t)$, $n_1(t)$ and $n_2(t)$ are jointly stationary and uncorrelated random processes. The cross correlation of $x_1(t)$ and $x_2(t)$ is given by

$$R_{x_1,x_2}(\tau) = kR_{ss}(\tau - \tau_d) \tag{4.53}$$

where $R_{ss}(\tau)$ is the autocorrelation of signal $s(t)$. Hence the peak value of the cross-correlation function occurs at $\tau = \tau_d$ which is proportional to a delayed replica of$R_{ss}(\tau)$.

Least Mean Square (LMS) Algorithm for Updating Coupling Factors

Let $\overrightarrow{T_0} = [T_{01}\ T_{02}\ ...\ T_{0N}]$ denote the required time delays to steer the transmitter array beam to a desired direction. We assume that all rings in each PRR delay line are identical and their coupling factors are the same, to obtain the maximum bandwidth. Hence, for each PRR in Fig. 4.11 there is just one variable to be optimized, henceforth called *coupling variable*.
Let $\overrightarrow{\kappa(n)} = [\kappa_1\ \kappa_2\ ...\ \kappa_N]$, and $\overrightarrow{\tau_M}(n) = [\tau_{M1}\ \tau_{M2}\ ...\ \tau_{MN}]$ denote the coupling

variables and the generated time-delays of all delay lines, respectively. The beamforming algorithm starts with an initial value for the coupling variables, $\overrightarrow{\kappa(0)}$, and updates them according to

$$\overrightarrow{\kappa}(n) = \overrightarrow{\kappa}(n-1) + \mu(n)\hat{G}(n)\xi(n-1) \tag{4.54}$$

where $\mu(n)$ is the step-size, $\xi(n-1)$ is the residual error at the end of the last iteration,

$$\xi(n-1) \;=\; \overrightarrow{T_0} \;-\; \overrightarrow{\tau_M}(n-1)\;, \tag{4.55}$$

and $\hat{G}(n)$ is the estimated gradient vector of the delay vector ($\overrightarrow{\tau_M}$) w.r.t. the coupling variables:

$$\begin{aligned} \hat{G}(n) &\approx \nabla_{\overrightarrow{\kappa}}(\overrightarrow{\tau_M}) \\ \hat{G}(n) &= [\hat{g}_1(n)\ \hat{g}_2(n)\ ...\ \hat{g}_N(n)]. \end{aligned} \tag{4.56}$$

Each component of $\hat{G}(n)$ is calculated using a centered finite difference approximation (Method b in Section 4.1.2), for example

$$\hat{g}_j(n) = \frac{\tau_{Mj}(\kappa_j + \delta) - \tau_{Mj}(\kappa_j - \delta)}{2\delta} \tag{4.57}$$

In practice the beamforming algorithm must apply two different biases for each TO phase shifter of the j^{th} PRR while other PRRs are not perturbed, to calculate $\hat{g}_j(n)$.

Measurement Noise

For each delay line, τ_{Mj} is the sum of the total delay (3.7) and a zero-mean Gaussian noise, n_G, which models the measurement error and other sources of inaccuracy

$$\tau_{Mj}(\kappa_j) = T_W + M\tau_1(\kappa_j) + n_G\ . \tag{4.58}$$

Termination Conditions

At the end of each iteration, the residual error for each delay line is calculated using (4.55). The norm of $\xi(n)$ is compared with a margin, ϵ, and if it was smaller or equal, i.e. $||\xi(n)|| \leq \epsilon$, the algorithm terminates. If the algorithm runs for a maximum number of iterations, ($N_{I_{max}}$), and the termination condition does not satisfy, the history of all generated time-delays for all iterations $1 \leq n \leq N_{I_{max}}$ is reviewed. The closest value to the desired delay is reported as the delay and the corresponding coupling factor is applied to PRR.

step-size

The general trend of LMS gradient approximation algorithms depends on the step-size behavior [64]. For example if $\mu(n)$ is positive, the time delay gradient approaches a local maximum point or $\tau_M(n)$ has an increasing trend. Since for all required time delays, the algorithm starts with the same initial condition, i.e. $\overrightarrow{\kappa}(0)$, the initial residual error, $\xi(0)$, is used to adjust the magnitude of the step-size. At each iteration the step-size is calculated according to

$$\mu(n) = \mu_0 \ \frac{\alpha^n}{||\xi(0)||} \ , \ \xi(0) = \overrightarrow{T_0} \ - \ \overrightarrow{\tau_M}[\overrightarrow{\kappa}(0)] \tag{4.59}$$

where μ_0 is a positive constant and α is a real number smaller than but close to unity (for example $0.97 \leq \alpha \leq 0.99$), which controls the convergence rate.

4.6.2 Beamforming for Receiver Phased Array Antennas

Fig. 4.12 depicts the proposed beamforming network for a single receiver PAA. The receiver system shown in Fig. 4.11 consists of N antenna elements and delay lines. After RF amplification, the received signal by each element modulates the optical carrier whose wavelength can be adjusted by the beamforming algorithm if a multi-wavelength laser is available. The optically modulated signal experiences a time delay as it passes through the DRR delay line. All delayed signals are demodulated by fast photodiodes and combined by a power combiner. The total received power is the only feedback available to the beamforming algorithm to adjust the coupling factors (and carrier wavelengthes).

Statement of the Beamforming Problem

When ODLs are used to adjust the array weights of a receiver array, the wight vector can be expressed as

$$\mathbf{w}(t) = [e^{j2\pi f_0 \tau_1} \ e^{j2\pi f_0 \tau_2} \cdots e^{j2\pi f_0 \tau_N}] \tag{4.60}$$

where τ_i is the time delay generated by the i^{th} delay line. The total received power by the array is given in (2.7)

Optical beamforming for a receiver array can be stated as a constrained optimization problem with the objective of maximizing the total received power by the array. If achieving the maximally flat group delay is the constrain, then the

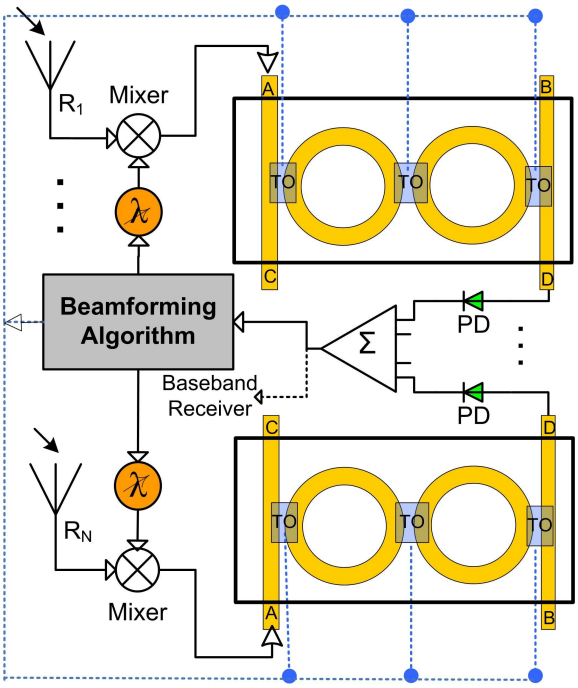

Figure 4.12: Simplified block diagram of a single receiver phased array antenna with optical beamformer. Filters and amplifiers have not been shown.

beamforming problem can be stated as:

$$\begin{aligned} &maximize \;\; P(\tau_1, \tau_2, \cdots, \tau_N) \\ &subject\ to: \;\; \kappa_{min} < \kappa_b < \kappa_{max} \;\; for\ each\ delay\ line \\ &\qquad\qquad \kappa_r = 1 - t_r \; in \; (3.18) \; for\ each\ delay\ line \end{aligned} \tag{4.61}$$

Hence, κ_b of each delay line is taken as a beamforming variable, and the corresponding κ_r is calculated using maximally flat condition given in (3.18). Sensitivity analysis (Section 3.5.3) determines the limits of κ_b.

Description of the Algorithm

If $\overrightarrow{\kappa_b} = [\kappa_{b1}\ \kappa_{b2} \cdots \kappa_{bN}]$ denotes the coupling variables of all delay lines, the update equation for $\overrightarrow{\kappa_b}$, for a receiver array, is given by

$$\overrightarrow{\kappa_b}(n+1) = \overrightarrow{\kappa_b}(n) + \mu_b \nabla_b P(n) \tag{4.62}$$

where $\nabla_b P$ is gradient of the total received power w.r.t. the coupling vector $\overrightarrow{\kappa_b}$. Each component of $\nabla_b P$, i.e. $\partial P / \partial \kappa_{bj}$, is calculated in three steps. First, κ_{bj} is slightly perturbed by adding a positive/negative perturbation to generate new

time-delays, τ_j^+ / τ_j^-. Next, τ_j^+ and τ_j^- are separately applied to the j^{th} array element and the total received power is measured for each one. Finally, the two power measurements are used to estimate $\partial P/\partial \kappa_{bj}$

$$\frac{\partial P}{\partial \kappa_{bj}} = \frac{P(\tau_1, \cdots, \tau_j^+, \cdots, \tau_N) - P(\tau_1, \cdots, \tau_j^-, \cdots, \tau_N)}{2\delta}$$
$$\tau_j^+ = \tau_d(\kappa_{bj} + \delta) \quad , \quad \tau_j^- = \tau_d(\kappa_{bj} - \delta)$$

When either the received power reaches a *termination threshold*, e.g. 98% of the maximum expected power, or the number of iterations exceeds a maximum value, N_{Imax}, the algorithm terminates. In the latter case a decision similar to Section 4.6.1 is made.

Modeling Noise and Inaccuracies

Three types of noise and error, which affect the optical beamforming for a receiver phased array, namely receiver, delay measurement and quantization noise, have been considered here.

Receiver Noise: It can be modeled by adding a zero-mean Gaussian noise to the array output in (2.6), hence the noisy estimate of the array output is used for power measurements, i.e.

$$\hat{y} = \mathbf{w}^H \mathbf{X}(t) + n_R(t)$$
$$P(t) = \hat{y}^H \hat{y}.$$

Delay Measurement Noise: To consider the unpredicted errors or shortcomings in modeling the delay line, a zero-mean Gaussian noise, n_d is added to the time delay calculated from (3.14)–(3.15)

$$\hat{\tau_d} = \tau_d(1 \ + \ n_d). \tag{4.63}$$

Quantization Noise: The beamforming algorithm communicates with delay lines and power combiner through digital to analog convertors (DAC). Each DAC adds a quantization noise, denoted by n_Q, to the input/output data

$$\hat{\kappa}_{bn} = \kappa_{bn} + n_Q.$$

Table 4.1 indicates that the quantization noise of a DAC with 8 bits or more is almost negligible.

Table 4.1: Quantization noise versus the number of bits in DAC

DAC bits	5	6	7	8	12
σ_{n_Q} (ps)	3.74	1.93	0.96	0.48	0.03

4.7 Optical Beamforming Simulation Results

In this section the results of the proposed beamforming algorithms are presented. Each algorithm is applied to a 5-element linear PAA with half RF-wavelength spacing. Three measures namely normalized *array gain*, minimum optical *bandwidth* and required *number of iteration* for convergence of the algorithm are used to evaluate the performance of each algorithm.

4.7.1 Transmitter Phased Array

The LMS beamforming algorithm explained in Section 4.6.1 is applied to a linear phased array radiating at 30GHz with (N=5) and 5mm spacing. Each elements is connected to a 3 ring PRR with $R = 134\mu m$ and the refractive index of $n = 3.46$. One resonant wavelength of this structure is $\lambda_0 = 1.55\mu m$, and the Free Spectral Range (FSR), defined as FSR=$c/2\pi nR$, is more than 100GHz. The objective is to steer the beam from $\theta = -45^\circ$ to 45° relative to the array normal.

The initial value for all coupling factors is 0.8. The algorithm is repeated 100 times for each steering angle and each time restarts with the same initial conditions. The standard deviation of n_G in (4.58) is set equal to $T_r/10$, where $T_r = 2\pi Rn/\lambda$ is the round-trip delay. The required delays for each direction $\overrightarrow{T_0}[\theta]$ are calculated from the well-known antenna relations and given to the algorithm as the references in (4.55). The algorithm continues to update the coupling factors based on (4.54)–(4.57) until one of the termination conditions is satisfied ($N_{Imax} = 50$ or $||\xi|| \leq \epsilon = \overrightarrow{T_0}[\theta]/100$). To steer the beam from $\theta = -45^\circ$ to 45°, the required time delay for all elements ranges from T_0=-47ps to 47ps. To accommodate the negative time-delays a constant delay is added as a bias to all desired time-delays such that the minimum time delay exceeds the intrinsic delay of PRR. Thus the required bias delay is

$$T_{bias} = \frac{d}{c}(N-1)\sin(\theta_{max}) + \frac{n_{eff}}{c}[2M(\pi+1)R + (M-1)\Delta x]$$

where θ_{max} and Δx respectively denote the maximum steering angle and the extra distance between the neighboring rings. In the current simulation the bias delay was set to $85ps$.

Array Gain

Fig. 4.13(a) shows the normalized array gain, defined as the power P in (2.7) divided by N^2, versus steering angle. The array gain is always above 99% close to the ideal value which occurs for the exact time delays in the absence of noise. For larger steering angles the required time delay increases. Since the error margin is 1% of the desired delay, consequently the absolute error increases, which explains the slight negative slope in Fig. 4.13(a).

Convergence Speed and Bandwidth

Fig. 4.13(b) and (c) show the bandwidth and the required number of iterations. As Fig 4.13(b) illustrates, the minimum bandwidth is 39GHz, which is 38% of the ring's FSR and occurs for the maximum time delay. The minimum bandwidth depends on θ_{max} and could be several times larger than the RF bandwidth of a 30GHz transmitter array. Fig. 4.13(c) illustrates that the required number of iterations for convergence and its corresponding standard deviation increase for small time delays. The average number of iterations for $\theta = -45^\circ$ in 100 runs of the program is 8 ± 2.7, whereas for $\theta = -10.6^\circ$ this number is 2.66 ± 0.55 which means most probably the algorithm converges after the third iteration. The overall average of iterations for generating a time delay in the range of 38–132ps is only 5.44. It implies that this algorithm is very fast and can be implemented with the conventional slow TO sensors in a practical system ($t_r \sim 1ms$).

4.7.2 Receiver Phased Array

The beamforming algorithm described in Section 4.6.2 is applied to a 5-element linear phased array receiver with the center frequency of f_0=20GHz. For all signal directions the algorithm starts with the same initial conditions implying that no *a priori* knowledge of the signal direction is assumed. SNR at the array output is 15dB, and the standard deviation of the delay measurement noise n_d is 1% of the generated time delay. Also 8-bit DAC is assumed for this simulation. The termination threshold is set to 98% of the maximum power and the maximum number of beamforming iterations is $N_{Imax} = 50$. The algorithm is run 100 times per signal direction.

Fig. 4.14(a) depicts the minimum, maxim, mean value and standard deviation of the normalized array gain for different signal directions. For isotropic elements

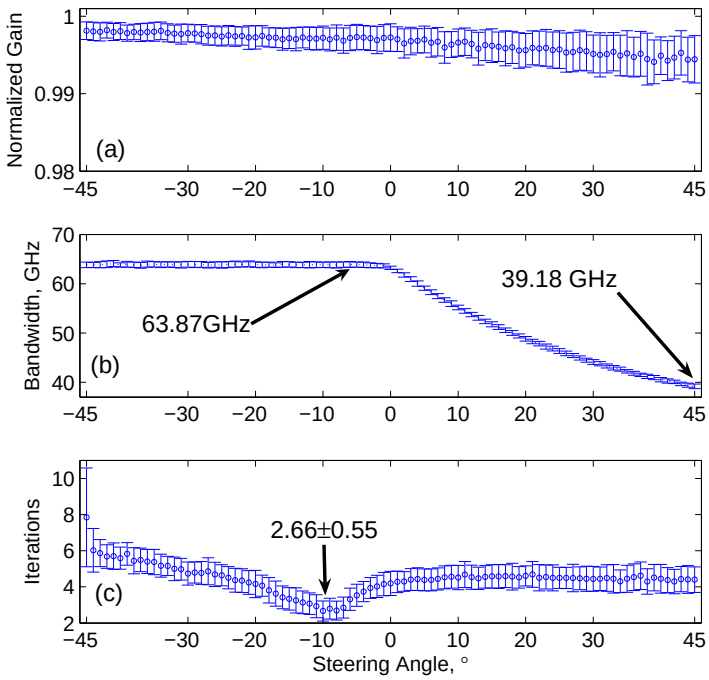

Figure 4.13: Statistical analysis of 100 runs of the beamforming algorithm for a transmitter phased array. a) Normalized array gain, (b) bandwidth, and (c) the required iterations for convergence versus steering angle.

with unity input power, the normalized array gain is defined as $G_N(\theta) = P(\theta)/N_E^2$, where N_E is the number of array elements and P is calculated from (2.7). In Fig. 4.14(a) G_N never drops below 98%, which implies that for all 100 runs of the algorithm, the received signal after beamforming has reached the termination threshold.

Fig. 4.14(b) shows the minimum optical bandwidth among the five delay lines. Bandwidth is defined as the frequency range centered at the resonant frequency, over which the time delay is above 85% of the peak delay. The minimum bandwidth is 14.7GHz. Further analysis shows the possibility of boosting the bandwidth by 1GHz (almost 7%) with the price of 2.5% drop in the received power level. Finally, Fig. 4.14(c) shows that the required number of iterations is far below the maximum value ($N_{Imax} = 50$). The overall average required iterations per delay line is less than 3 indicating the fast convergence speed of the proposed algorithm.

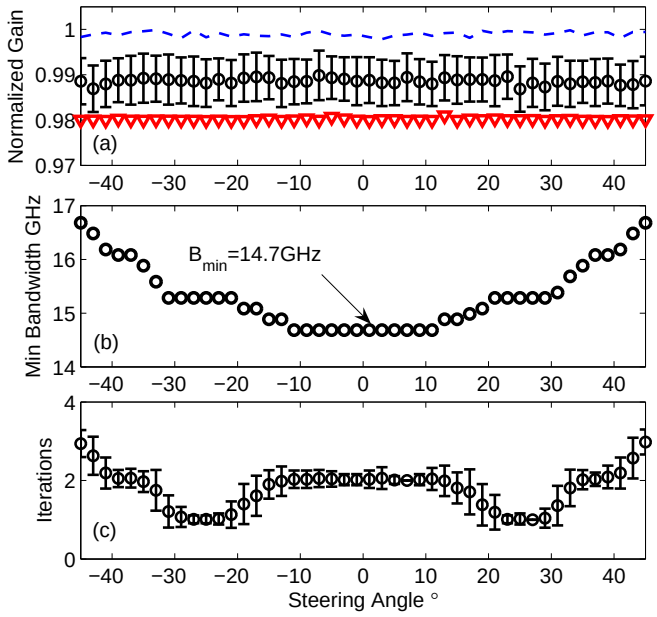

Figure 4.14: Statistical analysis of 100 runs of the beamforming algorithm for a receiver phased array. (a) Normalized array gain, (b) minimum bandwidth, and (c) the required iterations for convergence, versus steering angle.

4.8 Practical Issues of Proposed Optical Beamforming Techniques

4.8.1 Range of the Required Temperature

Fig. 4.15(a) shows the final coupling variables (κ_b) of each DRR in Section 4.7.2 (Fig. 4.14). To steer the beam from $-40°$ to $+40°$, the variation of coupling factors ranges from 0.08×10^{-2} for DRR_3 to 2.72×10^{-2} for DRR_5. It is desired to find the required temperature range of the TO phase shifters.

Varying the temperature changes the refractive index which consequently affects the coupling factors. Fig. 4.15(c) shows the coupling region between a ring and a waveguide ($R = 3.4\mu m$ and n_{eff}=3). The FDTD method is used to study the effect of refractive index variation on the coupling. A Gaussian-beam pulse at the resonant frequency enters point A. The coupling factor is defined as the ratio of the power at point C and point A. Fig. 4.15(b) shows that to change the coupling factor by 2.72% a 3.15% variation in the refractive index is required. To translate this change into a realizable temperature variation the thermo-optic coefficient of

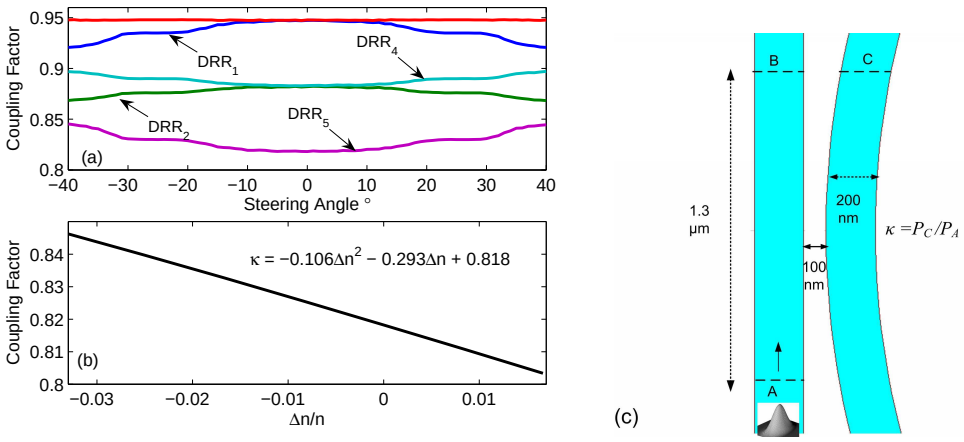

Figure 4.15: (a) Final coupling factors of five DRRs. (b) Variation of coupling factor with the refractive index. (c) The coupler between ring and waveguide.

the material must be high. For example, for polymethylmethacrylate (PMMA) polymer (n=1.48 at $\lambda = 1.3\mu m$) it is around as $-1.8 \times 10^{-4}C^{-1}$ [104], hence 170° shift in temperature is required. For rubbery polymers such as Urethane acrylate dn/dT is $-4.2 \times 10^{-4}C^{-1}$, hence 75° temperature shift is required. A simple way to decrease the range of temperature variation is to increase the number of rings in each delay line. Furthermore, there are other methods to adjust the coupling factor. In [138] a MEMS actuator has been used to change the coupling coefficient of a vertically coupled ring resonator.

4.8.2 Ring Size and Dimensional Tolerances

Fortunately the proposed optical beamforming algorithms depend on the gradient of group delay versus coupling rather than the absolute value of the delay. This is an important property making the algorithms robust and insensitive to fabrication tolerances or ambient variations. Although three types of noise have been considered in Section 4.6.2, a common practical issue is the fabrication tolerance of ring resonators. Fig. 4.16 shows the results of beamforming for the same array discussed in Section 4.7.2, when 1% fabrication tolerance has been considered for the radius of all 10 rings in the beamforming network ($133.3\mu m \leq R \leq 134.7\mu m$). Compared to Fig. 4.14, the mean array gain has dropped by 2.5%, and the mean required iterations for convergence has raised to 4. Also the minimum bandwidth has dropped by 1.2GHz. These range of variations are acceptable for a practical system.

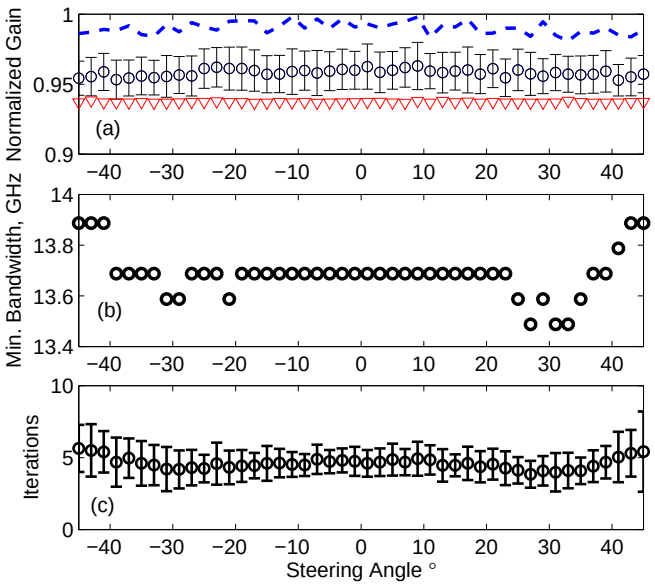

Figure 4.16: The effect of the ring size tolerance on the performance of beamforming for a receiver array.

4.9 Conclusions

Zero-knowledge beamforming algorithm is a fast and robust gradient-based method to steer the array beam toward a desired source. For Microwave applications, this beamforming algorithm adjusts the control voltages of the phase shifters based on the instantaneous power measurements. Since this algorithm does not depend on the phase shifter characteristics and signal DOA, an expensive laborious calibration procedure is eliminated. Moreover, this algorithm is a feedback aided method so it can adapt to ambient changes.

Zero-knowledge beamforming technique overcomes an intrinsic drawback of the commercial analog phase-shifters, the imbalanced insertion loss. The algorithm partially sacrifices the phase-coherency to reduce the insertion loss at the quiescent point of the phase shifters. This important characteristic of the algorithm can be expressed as the non-co-phased beamforming. We illustrated that noncoherent beamforming can increase the received power of the 17-element array level by more than 15%.

For a stationary scenario, a small step-size and fairly large perturbation help to diminish the noise impairments, however in a mobile scenario the fast convergence condition relates step-size to perturbation and predicts that for each element an

individual step size is required, which is proportional to the relative location of that elements. Simulation results show that a nonuniform step-size results in a higher power level and faster convergence.

This algorithm can serve as the core of a DOA estimation algorithm to find the relative direction of the desired source. Furthermore, simulations show that for MMW wireless applications this algorithm has a significant performance if shadowing blocks the LOS signal.

In the remainder of this chapter, two beamforming techniques -based on the properties of Zero-knowledge algorithm- for transmitter and receiver phased arrays were developed and compatible beamforming network architectures were proposed. It was shown that both algorithms converge very fast so they can be implemented with slow thermo-optic phase shifters with a reasonable range of temperature variations. Furthermore, the minimum optical bandwidth of the ODLs adjusted by the algorithm is several times larger than the required RF (base-band) bandwidth. The optical beamforming techniques are insensitive to fabrication tolerances or variable environmental conditions.

The experimental results presented in next chapter verify some of the important properties of Zero-knowledge beamforming algorithm.

Chapter 5

Experimental Results

In this chapter the experimental results of Zero-knowledge beamforming algorithm are presented. A 34–element Ku-band low-cost phased array antenna (17 elements per polarization) was designed and developed at the University of Waterloo and Intelwaves Technologies Ltd. (Waterloo, ON, Canada). This low-profile system was intended to be mounted on vehicles to receive the digital broadcasting satellite channels in North America. The algorithm developed in this work was used as the core of the beamforming unit of this phased array system.

5.1 Satellite Receiver Phased Array Antenna

This section briefly describes the hardware and operational modes of the Ku-band phased array system. The characteristics of the main components of the system, i.e. antenna, LNA, and phase shifter, as well as the implementation of the beamforming algorithm are discussed here. More information about this system is given in [13].

5.1.1 Overall System Description

Fig. 5.1 and 5.2 show the photograph and block-diagram of the fabricated stair-planar, single-receiver phased array system. This low-profile mobile array antenna ($h < 6cm$) consists of ten rows. The first five front rows support Left Hand Circular Polarization (LHCP), and the five back rows support Right Hand Circular Polarization (RHCP). Each row includes three or four radiating modules in the form of 2×8 or 2×16 microstrip sub-arrays. Three of the 17 sub-arrays allocated to each polarization are 2×8 and the rest are 2×16 sub-arrays. Hence, totally 496 microstrip patch elements receive each polarization. The sub-arrays are mounted on panels. Two stepper motors rotate these panels from 20° to 70° in elevation and from 0° to 360° in azimuth plane.

The sub-arrays are connected to LNAs via transition stages, and to the Phase Shifter/Power Combiner (PS/PC) box via cables. All phase-shifted signals of the same polarization are combined using multi stages of Wilkinson power combiner. The combined signal is amplified and then down-converted by a Low Noise Block (LNB). The down-converted signal is further processed by Digital Video Broadcasting (DVB) board to extract the satellite ID number, and sent to the baseband receiver inside the vehicle through a rotary joint. Each satellite has a unique ID. A power detector implemented in the DVB board filters and measures the received signal power. An Analog to Digital Convertor (ADC) circuit samples the measured power and sends the samples to the main processor executing the beamforming

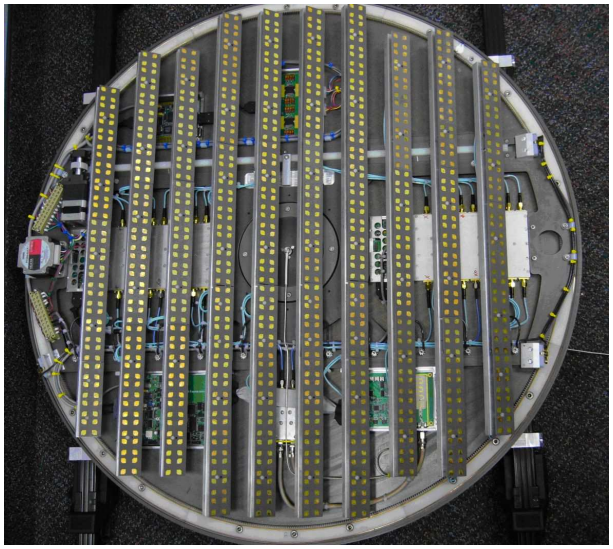

Figure 5.1: Fabricated Ku-band phased array system with 34 sub-arrays.

algorithm.

The hardware boards shown in Fig. 5.2 include main control board and several auxiliary boards such as Digital to Analog Converter (DAC), gyro board, motor control and driver boards. A compact and light mechanical platform, consisted of rotating and stationary parts is designed to hold the phased array system. The stationary part is attached to the roof of the vehicle through roof bars. All above mentioned electronic boards are integrated in the rotating part of the platform. The overall system design parameters have been summarized in Table 5.1.

5.1.2 Operational Modes

The mobile satellite receiver phased array system has three operational modes: Acquisition, Local Search, and Tracking. In the following, each mode is briefly explained.

Acquisition

After the system is switched on, Acquisition mode or Homing is activated. In this mode, system finds satellite without any prior information about its direction. Using two stepper motors, the mechanical search is performed in both azimuth

Table 5.1: Low profile phased array system parameters

Frequency	12.2-12.7 GHz
Polarization	Dual Circular
Gain	31.5 dB (per polarization)
Axial Ratio	$< 1.8dB$
Sub-Array Size	11.2, 22.3 cm
Spatial Coverage	$0^\circ - 360^\circ$ (Azimuth) $20^\circ - 70^\circ$ (Elevation)
Tracking Speed	$60^\circ s^{-1}$ (Azimuth)
System Height	6 cm
System Diameter	86 cm
System Weight	12 Kg

and elevation. Simultaneously, Zero-knowledge beamforming algorithm adjusts the phase shifters. When the received power exceeds a threshold, the control system extracts satellite ID and compares it with the desired satellite ID. As the received signal power depends on the environmental conditions and the vehicle position, the power threshold is set adaptively [13]. If the detected satellite ID was different from the desired one the Acquisition mode continues.

Local Search

Local Search is activated at the end of the Acquisition mode, or when a temporary signal outage occurs. The mission of this mode is to find the accurate direction of the satellite. The DOA estimation method, described in Section 4.5, in cooperation with the beamforming algorithm finds the satellite location.

Tracking

This mode maintains the satellite direction by compensating for the platform motions. A novel stabilization loop has been devised, which tracks the desired satellite for vehicle angular velocity and acceleration up to $60^\circ/s$ and $85^\circ/s^2$ respectively [14].

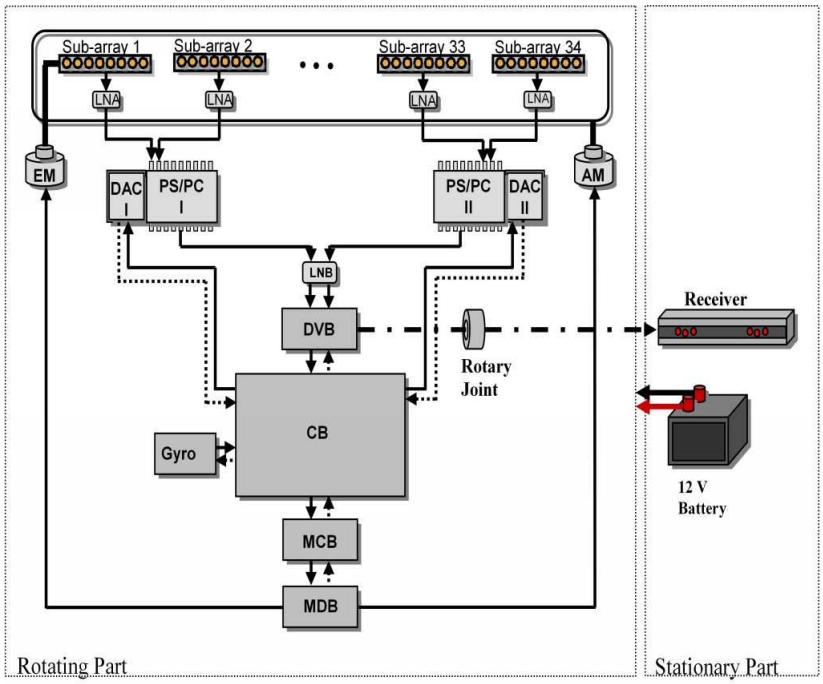

Figure 5.2: Block-diagram of the fabricated phased array system. AM: Azimuth Motor, CB: Control Board, DAC: Digital to Analog Converter, DVB: Digital Video Broadcast. EM: Elevation Motor, LNA: Low Noise Amplifier, LNB: Low Noise Block, MCB: Motor Control Board, MDB: Motor Drive Board, PS/PC: Phase Shifter/Power Combiner.

5.1.3 Components

Main hardware components of this system, including sub-arrays, LNA and phase shifter are described here. Phase shifters and power combiners of each polarization were integrated in a box and were connected via cables to LNAs and sub-arrays.

Sub-arrays

Fig. 5.3 shows the fabricated 2×16 sub-array, whose size is $22cm \times 3cm$. The length of 2×8 sub-array is $11cm$. Each microstrip patch has a gain of 6.7dBi and an axial ratio[1] of less than 3.5dB over the 4% relative bandwidth. The patch has a VSWR of 1.4:1 on the 50Ω line over the operating frequency. To improve the axial ratio further, four patch elements have been arrayed with sequential rotation of 0°, 90°, 180°, and 270° [139]. This spatial rotation must be compensated for by a corresponding electrical phase shift to retain circular polarization and achieve an

[1]Axial ratio is defined as the difference between the horizontal and vertical polarization components. For a pure circular polarization the axial ratio must be 1 (0dB).

axial ratio better than that of a single element. Having an axial ratio less than 1dB over the signal bandwidth is satisfactory. The designed four-element patch array is used as a building block for the formation of 2×8 and 2×16 sub-arrays.

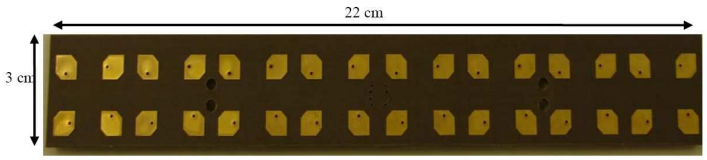

Figure 5.3: The 2×16 microstrip patch antenna used at the front end of the Ku-band phased array system.

Fig. 5.4 depicts the measured radiation patterns of the sub-arrays (followed by connectors) in the principal azimuth and elevation planes at 12.45GHz. The maximum measured circular polarization gain of the 2×16 and 2×8 sub-arrays are respectively 19.45dBi and 17.6dBi. The loss added by the surface mounted connector is estimated to be 0.5dB at this frequency range. Therefore, the actual gains are 20dBi and 18.1dBi for the 2×16 and 2×8 sub-arrays, respectively. The beamwidths of the 2×16 and 2×8 sub-arrays are severally 5° and 10° in azimuth plane and 39° and 41° in elevation plane.

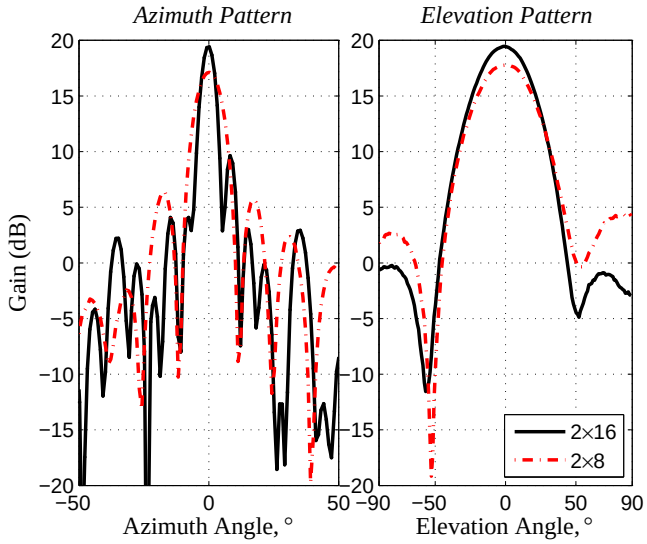

Figure 5.4: Measured radiation patterns of both sub-arrays.

Low Noise Amplifier

A high-gain and low-noise amplifier must follow each sub-array antenna immediately to reduce the overall noise figure of the phased array receiver. LNA design at this frequency band is a rather standard process, so only the measurement results are presented here.
The fabricated LNA was tested using network analyzer (Agilent 8722ES) and noise figure analyzer (Agilent N8975A). The measured parameters are shown in Fig. 5.5. The gain of the LNA is about 25dB with input and output return losses better than -10dB over the band of operation. The noise figure is also less than 0.8dB.

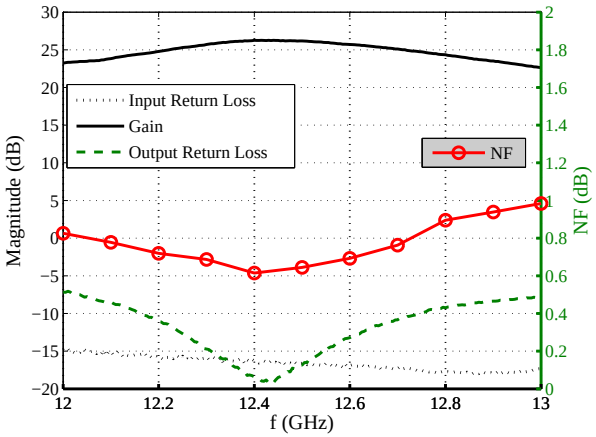

Figure 5.5: Measured gain and noise figure of the fabricated Ku-band LNA.

Phase Shifter

The measured characteristics of the designed reflective type phase shifter was presented in Section 2.2.3 (see Fig. 2.4). The control voltage of the phase shifters varies from 0 to 10v. Almost 8v variation in the control voltage causes one cycle of the phase shift.

5.1.4 Functional Block-diagram of the Beamforming Algorithm

Fig. 5.6 demonstrates how the beamforming algorithm is implemented in the phased array system. The beamforming function starts by perturbing the control voltage of the 1^{st} phase shifter from its current value. After each perturbation all phase shifters are updated. The processor refreshes the digital to analog converters, which

determine the bias voltages of phase shifters. Thus, the radiation pattern (array factor) of the phased array antenna is updated and a new power measurement is required. The output of the RF power detector is sampled with the rate of 40KHz. To diminish the effect of noise 8 to 30 samples undergo a digital low pass Hamming filter [134]. The number of samples depends on the intensity of noise. This number significantly affects the beamforming speed [133], because the processor is much faster than ADC (the processor speed in this system is 200 MIPs). The weighted average of these samples is reported as the measured power. The voltage perturbation and power measurement process repeats 32 times ($N^* = 32$), if the two sided gradient estimation method was used, because the voltage of one of the phase shifters is always fixed. The processor calculates the estimated gradient vector and finds the updated voltage vector, $\mathbf{v}(n+1)$. All phase shifters are updated with the new calculated voltages and the received power is measured after digital filtering. Now one iteration of the algorithm is complete, so the final measured power is recorded as the output of beamforming. In parallel, DVB board processes the received signal. If the power level is adequately high it can extract the satellite ID. Nevertheless, the beamforming algorithm continues to increase the received power level to obtain the required SNR for high quality video reception. In the following sections, the experimental results are presented.

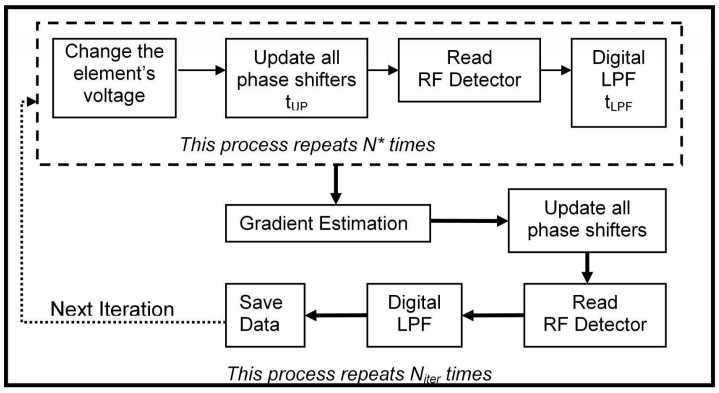

Figure 5.6: Functional block-diagram of the beamforming algorithm.

5.2 Variation of Algorithm Parameters

Two series of tests were conducted to investigate: 1)how variation of the algorithm parameters affect the convergence and steady state (s.s.) performance of the beamforming, and 2)find the proper values for each parameter. The two-sided gradient estimation method was used in these beamforming tests. First, the step-size (μ)

was fixed at 0.5 and the perturbation (δ) was varied from 0.125 to 2. The phased array was initially rotated toward the satellite. Fig. 5.7 shows the measured received power versus time for some of these tests. Each graph represents the average of 50 repetitions of the beamforming test, and the errorbars represent the statistical standard deviation of the experiments. Each test starts from the same initial condition, and includes 50 beamforming iterations. As δ increases from 0.125 to 1 the s.s. error decreases. However for further increase of δ, the algorithm becomes unstable and starts to oscillate. The large errorbars for $\delta = 0.5$ is because during the 50 repetition of the beamforming process for this test, some of the results imitates the behavior of $\delta = 0.125$ test(large s.s. error) and the rest were similar to that of $\delta = 0.85$ test. In other words, $\delta = 0.5$ test shows a transition.

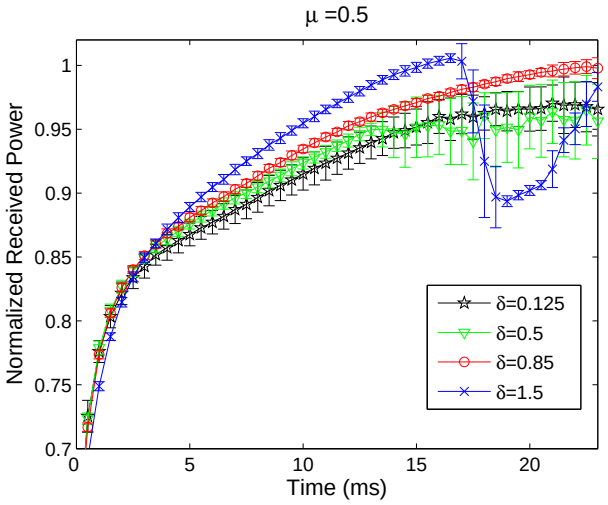

Figure 5.7: Experimental results of the beamforming algorithm for $\mu = 0.5$.

Next, δ was fixed at 1 and μ was varied from 0.1 to 1.5. Fig. 5.8 shows that for larger step-sizes the convergence of the measured power speeds up, however the errorbars for $\mu = 0.5$ at the steady state are slightly smaller than that of $\mu = 1$. The behavior of beamforming algorithm versus step-size and perturbation is in good agreement with the simulations presented in Section 4.2.1. Most of those simulations were performed for SNR=20dB, however during the above field tests the received baseband SNR at the array output (after the power detector) was better than 30dB. Furthermore, it must be mentioned that the power detector used in the DVB board of the Ku-band phased array system was a logarithmic amplifier preceded by a bandpass filter (950-1200MHz), while in simulations only a narrowband (single frequency) array was modeled. Finally, these two sets of experiments for stationary array propose the proper value of the parameters to be $0.75 \leq \delta \leq 1$ and $0.4 \leq \mu \leq 0.9$.

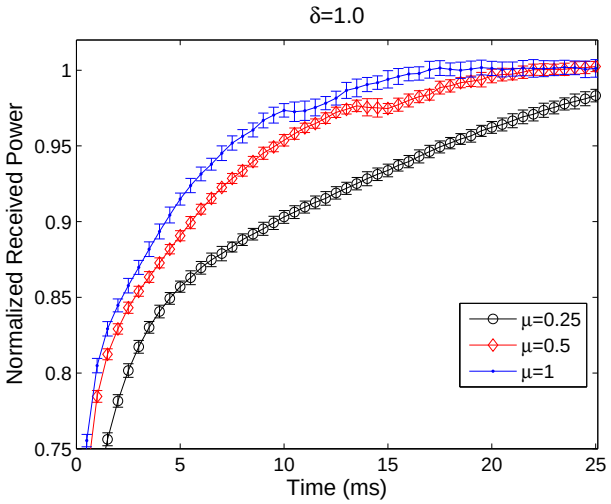

Figure 5.8: Experimental results of the beamforming algorithm for $\delta = 1$.

5.3 Spectral Measurements

The carrier frequency of the DBS satellites in North America ranges from 12.2-12.7GHz resulting in a bandwidth of 500MHz. This range has been equally divided among 32 transponders (16 for each polarization). An important test to measure the performance of the beamforming algorithm is to investigates its behavior over the whole frequency region.

Initially, the Acquisition and Local Search modes were performed to find the best location of the satellite providing the highest received power. To investigate how the proper selection of the beamforming parameters affects the spectral response of the array, two tests were designed. For the first test the algorithm parameters were set to $\mu_1 = 0.1$ and $\delta_1 = 0.5$. From the discussions in Section 4.2, we already know that this set of parameters causes a slow convergence. The received SNR (after power detector) at the time of the test (Jul. 19, 2007, Waterloo, ON) was measured to be around 31dB. Agilent E4405B spectrum analyzer was used to measure the spectral response of the array. For each spectral measurement, the average of 200 successive frames were taken to smooth the instantaneous fluctuations. The three curves in Fig. 5.9 show snapshots of the IF spectrum of the received LHCP signal at the initial conditions I_0, after the first iteration I_1, and after 10 iterations I_{10} of the Zero-knowledge beamforming. Only the first five satellite transponders have been shown in this figure to provide distinguishable graphs. In the second test the algorithm parameters were set to $\mu_2 = 4\mu_1$ and $\delta_2 = 2\delta_1$ to achieve a fast convergence. Fig. 5.10 depicts I_0, I_1 and I_{10} for this test. The reference level, frequency span and scales of both figures are the same and respectively equal to

-51.66dBm, 150MHz, and (15MHz, 1dBm). In Fig. 5.10 a large gap is observed between I_0 and I_1, implying that even one iteration of the algorithm increases the received power significantly. Also the spectrum of I_{10} for the second test is between 1.2 to 2.5dB higher than that of the first test for all transponders. These spectral measurements show the satisfactory broadband performance of the algorithm and how the proper selection of μ and δ, results in a faster convergence.

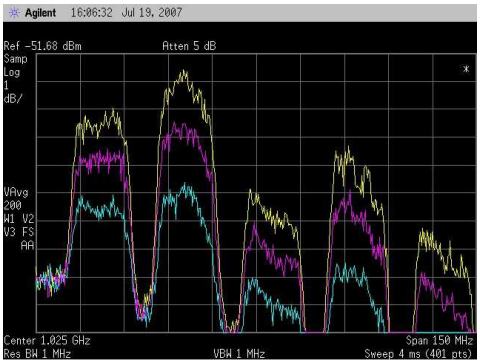

Figure 5.9: Spectrum of the received signal for slow convergence of the beamforming. The three curves from bottom to top represent I_0, I_1 and I_{10}.

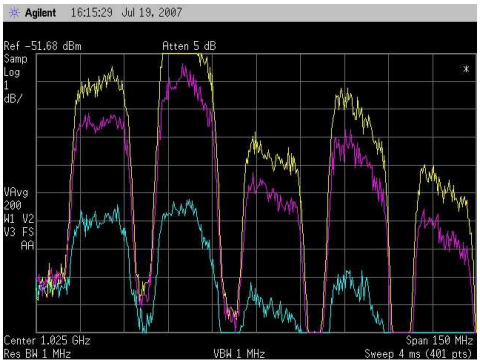

Figure 5.10: Spectrum of the received signal for fast convergence of the beamforming.

5.4 Beamforming in Motion

This section provides the experimental results for Section 4.3.

5.4.1 Merit of Nonuniform Step-size

In this experiment the results of beamforming with uniform and nonuniform step-sizes are compared. Both tests started with the same initial conditions, i.e. $\mathbf{v}_0 = 6v$. The uniform step-size was fixed at $\mu = 0.25$ and for the nonuniform case the step-size was varied proportional to the element location such that the mean value of the step-size vector remained equal to 0.25. Let r_k denote the location of element k, then μ_k is given by

$$\mu_k = 0.126 + 0.45 r_k$$
$$r_k = \sqrt{x_k^2 + y_k^2} \quad and \quad \overline{[\mu_k]} = 0.25$$

For each case the beamforming algorithm was repeated 50 times. Fig. 5.11 shows the mean value of the normalized received power. The average received power after 50 iterations was 6% higher when the nonuniform step-size was used, which verifies the simulation results in Section 4.3.3.

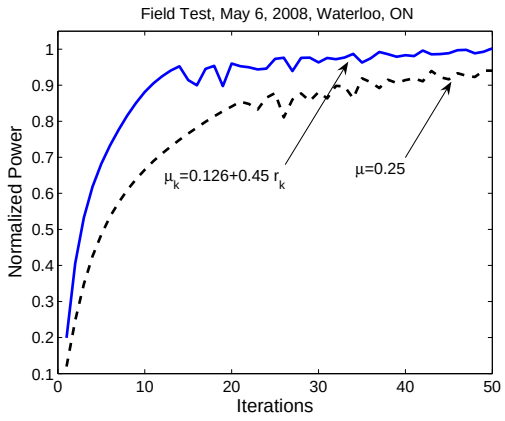

Figure 5.11: Experimental results for beamforming with the uniform and nonuniform step-sizes.

5.4.2 Three Platform Maneuvers

To study the Zero-knowledge beamforming behavior for a mobile platform, two rate sensors were mounted on a van vehicle and multiple road tests were performed to collect measured data [2]. Three of these maneuvers are analyzed in this section. A phased array simulator was developed in MATLAB to study the behavior of beamforming algorithm for different road tests. The phased array simulator includes measured radiation patterns of the sub-arrays, exact geometry of the array,

[2]These tests were conducted at Winegard Co., Burlington, IA, USA with a van vehicle.

and measured models of LNAa, cables, phase shifters, power combiners and digital subsystems.

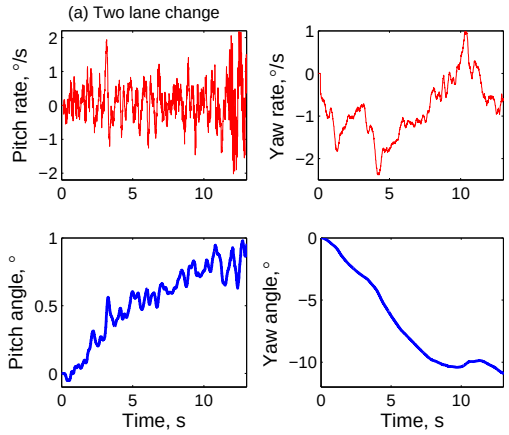

Figure 5.12: Pitch rate, yaw rate, pitch angle and yaw angle of two lane changes.

First vehicle maneuver consisted of two successive lane changes. Fig. 5.12 demonstrates the pitch rate, yaw rate, pitch angle and yaw angle of the van during this maneuver. The yaw angle is consistently decreasing which indicates that the van has been turning left. The pitch angle does not change significantly which implies that the road slope was almost constant.

The second test comprised of 28s drive on a rough road. Fig. 5.13 shows that both pitch and yaw angles have been changing significantly and their rates were higher than that of Fig. 5.12, especially the pitch rate.

The third test consisted of making a sharp S-turn on a regular road which took 15s and the maximum change in yaw angle was around 160° as shown in Fig. 5.14. The sampling rate of the rate sensors in all tests was 100Hz. The stabilization loop of the phased array system compensates for the large angular vehicle displacements with an intrinsic delay which is much larger than the beamforming delay.

Using the phased array simulator, the beamforming algorithm was executed for each maneuver. The execution time of each beamforming iteration was set to 10ms. The SNR after power detector was 31.2dB and 8-point Hamming digital filtering was applied to the measured power. Fig. 5.15 shows the results of beamforming for each maneuver. For the double lane change and driving on a rough surface the algorithm was performing very well and the signal level never dropped below 90%; however, for the sharp S-turn maneuver the received signal faded several times and even dropped to below 52% but after a short fading period the beamforming algorithm was able to recover the power level. Comparing Fig. 5.14 and Fig. 5.15(c)

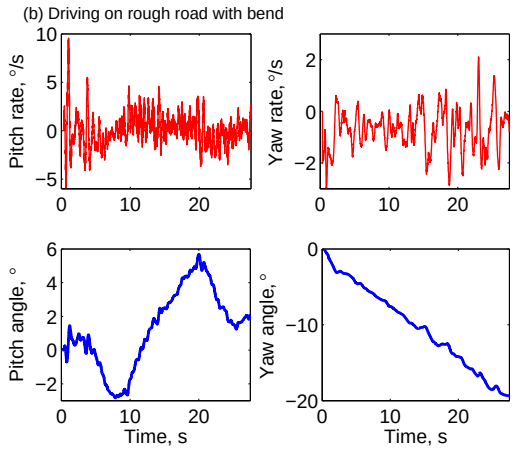

Figure 5.13: Pitch rate, yaw rate, pitch angle and yaw angle of driving on a rough road.

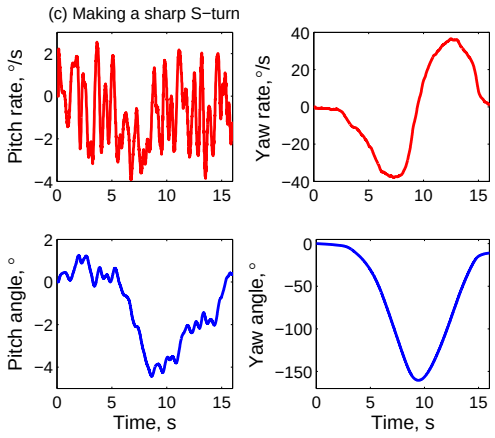

Figure 5.14: Pitch rate, yaw rate, pitch angle and yaw angle of a sharp S-turn.

one can find that the maximum error occurred at $t = 6.97s$ and $t = 12.36s$ when the yaw rate reached its extreme points. Moreover, when the absolute angular rate exceeds $20°/s$ the error raises, which implies that the hardware and processor speed must be increased to achieve a better performance. Indeed, the execution time of each beamforming iteration in the current system could be as fast as $5ms$. A video clip in Appendix C demonstrates when beamforming and mechanical stabilization loop operate at their highest speed, the received signal is not interrupted even for the maneuvers faster than the one shown in Fig. 5.14.

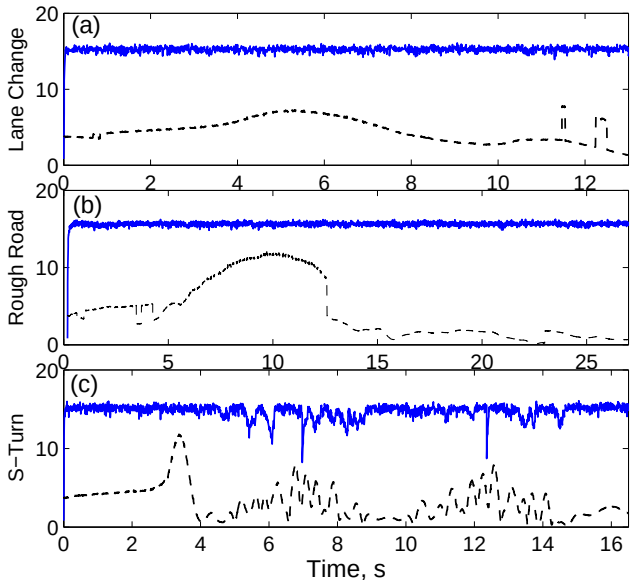

Figure 5.15: Beamforming results for three maneuvers. The vertical axis shows the received power. The dashed lines show the received power by a fixed beam normal to the array.

5.5 Experimental Results of the DOA Estimation Algorithm

Five out of the 17 sub-arrays (for each polarization) shown in Fig. 5.1 are approximately located on the symmetry axis and the variation of the required phase-shift is negligible for them, so at most 12 rules similar to (4.50) and (4.51) in Section 4.3.3, can be defined for this system. Defining more rules lowers the error probability in the DOA estimation. In the developed phased array system, d = 223mm, and λ=24mm. So, if satellite shifts 1° away from the array normal, the phase difference between the adjacent elements becomes $\Delta\phi = \pm 58.4°$.

Fig. 5.16 shows the results of an off-board test, where the array was stationary. The test procedure is as follows. Once the satellite was found (end of the Local Search mode) and the reference voltages were stored in the database shown in Fig. 4.8, the array was moved randomly to a position to the left of the satellite denoted by $\theta = 0°$ in Fig. 5.16. The L/R command was disabled for the test purpose, so the array was manually rotated to the right side in steps of 0.3°. The beamforming algorithm was run for 10 iterations at each angular position. Next the DOA algorithms announced the relative direction of the satellite. This process was repeated 100 times to find the error probability.

As shown in Fig. 5.16 the DOA algorithm announced the satellite position (labeled as middle) at $\theta = 2.1°$ relative to the start position. Accordingly at the same position the received power peaked. The array was rotated for a few more steps to check the performance of the algorithm when the array was on the right side of the satellite. For all positions, the performance of the DOA estimation algorithm was completely satisfactory.

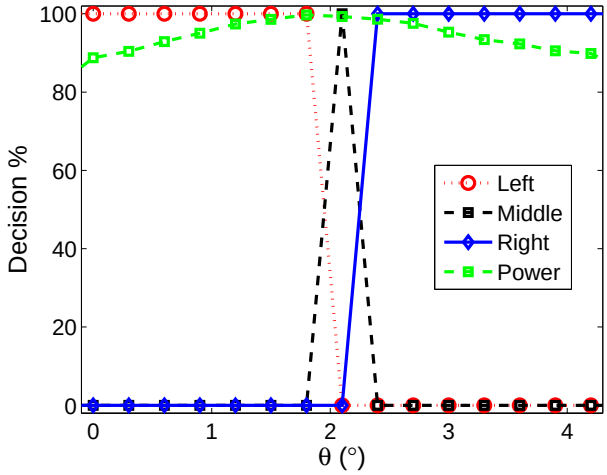

Figure 5.16: The experimental results of the DOA estimation algorithm.

Chapter 6

Conclusion and Future work

6.1 Contributions and Conclusions

This section presents a summary of the contributions of each chapter of this thesis. A list of the publications originated from this work has been given in Appendix D.

In Chapter 2, the practical considerations of analog phase shifters were discussed. Studying the effect of the imbalanced phase shifter loss on coherent beamforming gain and array efficiency is one of the contributions of Chapter 2. It was shown that the imbalanced phase shifter loss can degrade the array efficiency of a 2-element phased array up to 44%. Moreover, it was discussed that the fabrication tolerance is a serious design issue. Thus, a robust and non-model-based algorithm is required to find the desired phase shifts.

A fundamental limit of analog phase shifters is their narrow-band response. Although use of optical delay lines is a well-known solution to beam squint, current optical delay lines are mostly bulky and impossible to be integrated in a chip. In Chapter 3, four types of miniaturized optical delay lines, which can be integrated with other optical subsystems to obtain a compact integrated optical array, were analyzed. Meandering photonic crystal delay lines are ultra-wideband devices ($B \sim$ 1THz), which can mold the propagation of light at sharp corners. A novel structure, called Reflective Spiral Line, was introduced with a slowing factor of 22 and moderate delay-tunability. Coupled photonic crystal cavities even generate longer delays for the same device size. For the purpose of beamforming, tunability of delay line is crucial. Instead of using bulky lossy switches with fiber delay lines, coupled ring resonators can be utilized to change the generated delay continuously. Another contribution of this work was introducing the maximally flat group delay condition, and sensitivity analysis of the cascaded ring resonators. The output of this analysis is a relation between coupling coefficients and the proper bounds for them.

In Chapter 4, a novel beamforming algorithm, called Zero-knowledge beamforming was introduced. Noise analysis was used to determine the (limits of) algorithm parameters. Another contribution of this thesis lies in introducing the *fast convergence* condition for mobile phased arrays. This condition suggests to allocate a separate step-size to each array element proportional to its position in the array. It was shown that the proposed beamforming algorithm can partially compensate for the imbalanced insertion loss of the low-cost analog phase shifters. It perturbs the phase-conjugate condition to increase the received power. Up to 1.7dB growth in the gain of a 12-element array can be obtained using this algorithm [32]. Another interesting property of Zero-knowledge beamforming algorithm is the estimation of

the signal DOA. Thus, it can compensate for the inaccuracies of the low-cost rate sensors employed in the mechanical control loop of a mobile phased array system. Furthermore, the proposed beamforming technique has the potential of switching the array beam to the direction of the strongest multi-path component if the LOS link has been obscured.
This algorithm can constitute the core of two optical beamforming techniques used for transmitter and receiver phased array antennas. These techniques adjust the coupling coefficients of the coupled ring resonator delay lines to steer the antenna beam to a desired direction or receive signals from a desired target with unknown DOA. These techniques are insensitive to the fabrication errors of ring resonators.

Zero-knowledge beamforming algorithm described in Chapter 4 has been successfully implemented in a low-cost phased array system, which is a mobile Ku-band satellite receiver with 34 sub-arrays. The experimental results presented in Chapter 5, are in good agreement with the theoretical and simulation results.

6.2 Future Research Directions

There are several opportunities for the future research and continuation of this work, such as:

1) The beamforming algorithm developed in this thesis was applied to a single receiver phased array system. Nevertheless, many communication applications require a two-way link (both uplink and downlink). For example, mobile data transmission requires to receive signals from single or multiple nodes and transmit information to other nodes. Extension of this work to beamforming for a two-way phased array is an important objective. Investigation of beamforming for reconfigurable or retro-directive arrays has already started [127].

2) Zero-knowledge algorithm which was initially developed for receiving broadcast satellite signals, works properly if the sources are well separated (not to be in the main beam at the same time). However, to use this algorithm for the ubiquitous wireless networks, the interference-nulling ability must be incorporated in the algorithm. This will certainly add to the complexity of the algorithm and may require auxiliary hardware, but increases the range of applications significantly, because the performance of multiuser wireless networks is limited by interference.

3) Zero-knowledge algorithm is promising to have a significant performance in wireless MMW channel, when shadowing obscures the LOS signal. Implement-

ing the beamforming algorithm at MMW to verify its performance could be an important research task.

4) Comparing the result of the Zero-knowledge algorithm with the optimization tool-boxes, such as LOQO [140], is necessary to evaluate the real performance of this algorithm. To make a fair comparison, the phase shifter characteristics (loss and phase versus voltage) must be modeled with high-order polynomials. Moreover, the 3D radiation pattern of the antenna elements must be incorporated in the optimization problem.

5) The miniaturized optical delay lines discussed in Chapter 3 have significant advantages over the conventional delay lines in terms of bandwidth and compactness. Fabrication and characterization of the designed photonic crystal delay lines is necessary to verify their advantages. Such delay lines can be used for a variety of applications such as signal processing, buffering, filter design, etc. Furthermore, ring resonator delay lines are amongst the best options for optical beamforming of broadband phased arrays. In Section 4.7 two optical beamforming algorithms were developed based on the properties of coupled ring resonators. An experimental set-up must be developed to experimentally verify the performance of these algorithm.

APPENDICES

Appendix A

Noise Figure Calculation

A.1 Overall Noise Figure Clculation

Fig. A.1(a) illustrates the equivalent noise model of the phased array receiver. The total received noise, n_0 at the combining point [69] is

$$n_0 = \sum_{k=1}^{M} n_k \ , \tag{A.1}$$

where M is the number of branches, and n_k, the total noise of each branch, is given by

$$n_k = \frac{kT_eB\ g}{L_fL_dL_k} + \frac{kT_0B(L_f-1)g}{L_fL_dL_k} + \frac{kT_0B(NF-1)g}{L_dL_k} + \frac{kT_0B(L_d-1)}{L_dL_k} + \frac{kT_0B(L_k-1)}{L_k} \tag{A.2}$$

where B is the noise bandwidth, T_e is the antenna equivalent noise temperature, T_0 is the room temperature, $k = 1.38 \times 10^{-23} J/K$ is the Boltzmann constant, and g and NF denote the gain and noise figure of the LNA. Also L_f, L_d, and L_k denote the front-end loss from antenna to LNA, downstream loss from LNA to phase shifter and the variable attenuation of each channel respectively. Parameter L_k is directly related to the phase shifter characteristic at the operational frequency, and the beamforming algorithm. The antenna equivalent noise temperature is related to the sky noise temperature (T_i), which is usually smaller than the room temperature, and the antenna efficiency (η) [141],

$$T_e \ = \ \eta T_i \ + \ (1-\eta)T_0 \ . \tag{A.3}$$

Assuming all antennas and LNAs are identical, the overall noise temperature of the phased array system is given by [69]:

$$T = T_e + T_0 \left(L_fNF - 1 - \frac{L_f}{g} + \frac{N}{\sum_{k=1}^{N} 1/L_k} \frac{L_f}{g} L_d \right) \ . \tag{A.4}$$

Hence, the total noise figure, is

$$NF_{Tot}|_{dB} \ = \ 10 \log_{10} T/T_0 \ . \tag{A.5}$$

If the LNA gain is sufficiently high ($g \gg 1$), the system noise temperature simplifies to

$$T \ \simeq \ \eta T_i + T_0 \left(L_fNF - \eta \right) \tag{A.6}$$

Equation (A.4) reveals that antenna efficiency, front-end loss (L_f), LNA noise figure (NF) and LNA gain (g) have the most contribution in determining the total

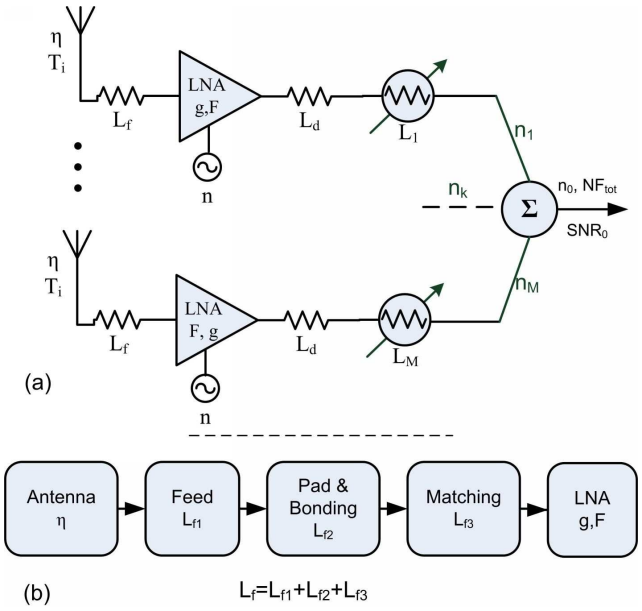

Figure A.1: (a) The equivalent noise model of a single receiver phased array antenna. (b) The dominant contributing factors to the total NF of the system.

noise figure of the system. Hence the key issues in designing a low noise receiver are to design an efficient antenna, reduce the front-end loss from the antenna to LNA, reduce the NF of the LNA and increase its gain. Fig. A.1(b) illustrates the contributing factors to the total NF of the system. The front-end loss consists of three components: antenna feed loss L_{f1}, pad/bonding parasitics and loss L_{f2}, input matching loss L_{f3}.

A.2 SNR at the Array Output

The received SNR at the array output (combination point), SNR_0 is

$$SNR_0 = SNR_I \frac{G_e(\overrightarrow{\mathbf{r}}) \times G_B(\overrightarrow{\mathbf{r}})}{NF} \tag{A.7}$$

where $\overrightarrow{\mathbf{r}}$ denotes the received signal direction, $G_e(\overrightarrow{\mathbf{r}})$ is the gain of the antenna element and $G_B(\overrightarrow{\mathbf{r}})$ is the beamforming gain (array factor). NF is calculated from (A.5). Finally SNR_I is the SNR received by an isotropic antenna, which is related to the transmitter's $EIRP$ in the direction of receiver antenna, total path loss from transmitter antenna to the receiver $L_P(\overrightarrow{\mathbf{r}})$, and the background noise (kT_0B):

$$SNR_I = \frac{EIRP_T(\overrightarrow{\mathbf{r}})L_P(\overrightarrow{\mathbf{r}})}{kT_0B} \tag{A.8}$$

The goal of the beamforming algorithm is to increase G_B to provide the required SNR_0 determined by BER constrains. The ideal limit of G_B is equal to the number of array elements, however as we will show, the variable insertion loss of the phase shifter reduces the beamforming gain.

Appendix B

Broadcasting Satellite Signal Channel

Fig.B.1 illustrates a simple propagation model for mobile satellite receivers. High-gain antennas used for satellite communications posses narrow beams and low sidelobe levels. A considerable amount of research and experiment has been

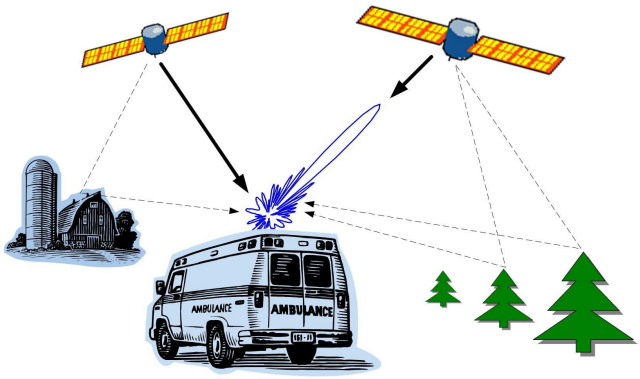

Figure B.1: Propagation model for a mobile satellite receiver array.

performed on obtaining the basic channel characteristics of mobile satellite systems at different microwave frequencies [142] - [148]. Propagation measurements indicate that in transmission between a satellites and a moving vehicle a significant fraction of the total energy arrives at the receiver by way of the direct path [147]. Table 1 in [144] lists some of the proposed models for narrowband satellite channels. Most of these models use a Rice or Nakagami distribution for the multipath fading and a lognormal distribution for the line-of-sight (LOS) component which is subject to shadowing. The lognormal distribution for the LOS component (z) is given by:

$$p(z) = \frac{1}{\sqrt{2\pi d_0 z}} exp\left[(-ln(z) - \mu_L)^2/2d_0\right] \tag{B.1}$$

where d_0 and μ_L are the variance and mean, respectively [142]. Such models have two drawbacks: The effect of the receiver antenna pattern and the antenna elevation angle have not been addressed. In the following, we discuss these two issues and show that beamforming for the satellite receiver arrays is not an interference or multipath limited problem,. Indeed, maximizing the received power should be the main purpose of beamforming rather then interference nulling or mutipath control.

Effects of Array Pattern on Multipath

Consider 2 antennas with 2 different patterns shown in Fig. B.2. Both antennas have the same maximum gain (20dB). Antenna 1 has a broad beamwidth while antenna 2 has a narrow beamwidth with a much lower sidelobe level. Consider a 2D scenario where each antenna is mounted normal to the ground and there are 1000

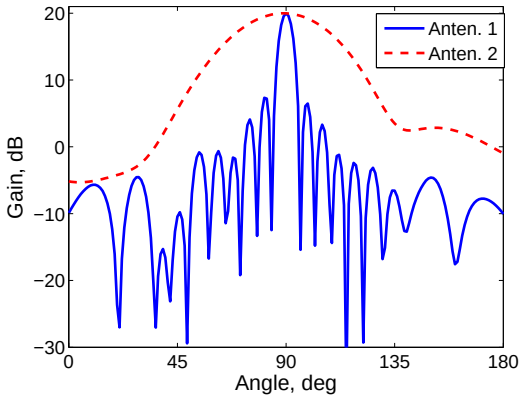

Figure B.2: 2D radiation patterns of two antennas. These patterns are the vertical and horizontal cross sections of the 3D radiation pattern of the subarrays shown in Fig. 5.3.

scatterers distributed from $0 - 45^{\circ}$ in elevation. The power reflection coefficient of scatterer, ρ_k has a uniform distribution between 0 and 0.01. Scatterers are distributed uniformly in the region and the phase of the received signal, Φ_k, has a uniform distribution over $(0\ 2\pi)$. The total received power from scatterers is

$$P_{Scat} = \left| \sum_{k=1}^{N_{Scat}} G(\theta_k)\rho_k exp(j\Phi_k) \right| \tag{B.2}$$

where $G(\theta_k)$ is the gain of the antenna (Fig. B.2) in the direction of scatterer. Fig. B.3(a) demonstrates the PDF of the total scattering power received by 2 different antennas for 10^5 random samples. It is seen that the distrbution of the scattering power is almost Rayleigh and the mean value of the received signal by antenna 2 which has a broader beam is almost 5 times larger than that of the antenna 1. The mean value of the received scattering power by antenna 1 is 3 order of magnitudes smaller than the satellite power.

The effect of elevation angle on Multipath

Equation (B.2) can be easily extended to 3D configurations:

$$P_{Scat} = \left| \sum_{k=1}^{N_{Scat}} G(\theta_k, \phi_k)\rho_k exp(j\Phi_k) \right| \tag{B.3}$$

In this case we consider the 3D radiation pattern of the 2×16 sub-array in Fig. 5.3 derived by accurate HFSS simulations. Indeed Fig. B.2 shows the vertical and horizontal cuts of this 3D pattern. Generally, antennas designed for satellite receivers

such as Dish antenna and microstrip arrays have a narrow beam because they must have a high directivity [149, 150]. On the other hand terrestrial multipath mostly distributed in low elevation angles while for North America the elevation angle of the GEO satellite receivers changes from a minimum of 30° at Edmonton to a maximum of 70° at Miami.

Fig. B.3(b) illustrates the probability distribution of the received scattering power form 1000 objects for different antenna elevation angles. Scaterres have bean distributed uniformly in azimuth (from $0 - 360°$) and in elevation (from $0 - 20°$). Hence $\Delta\theta$ in Fig. B.3(b) represents the angular distance between the beam axis and the scatterer with the highest elevation ($\theta = 20°$). It is evident the for $\Delta\theta \geq 20°$ the mean value of P_{Scat} is constant and only 0.05% of the satellite power.

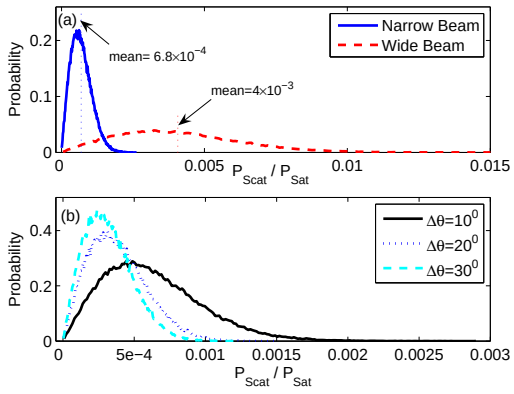

Figure B.3: Probability Distribution Function of the total scattering power. (a) When 2D patterns of Fig. B.2 have been used.(b) When 3D radiation pattern has been used. Each curve represents a different antenna elevation angle.

Co-Channel Interference

A list of satellites in geosynchronous orbit is given in [151] which indicates that there is at least one satellite in each 2°. However these satellites have different carrier frequencies and applications or providers. For example DircTV satellites which are Ku-band broadcasting satellites covering North America are located at $119.0°W$, $110.0°W$, and $101.2°W$ so for an observer on equator the relative angle between two adjacent satellites is around 9°. Since the array beamwidth in azimuth is only a few degrees (3° in our case), due to the required high array gain, once the array has been steered to the desired satellite the co-channel interference is significantly attenuated by the array radiation pattern. Moreover each broadcasting satellite has a *unique* DVB-ID which is detected by the DVB board in the receiver, thus the

undesired signals will not be decoded. Thus co-channel interference is not a severe threat for satellite receivers.

Input Noise

In satellite communication, the input noise depends on the elevation angle. For lower elevation angles the received noise is higher [152]. Also the fluctuations of the amplitude caused by scattering and out of band interference signals can be modeled as noise.

Appendix C

Multimedia Files

This appendix is a video file of an experimental test of the Ku-band satellite receiver phased array antenna developed at the University of Waterloo and Intelwaves Technologies Ltd.

Appendix D

Publications from Thesis

Patent

- 1- A Hybrid Satellite Tracking Control System for Low Profile Phased-Array Antennas, Patented in Canada/USA, File No. 60/92,4856 filed June 2007

Journal Papers

1. **M. Fakharzadeh**, O.M. Ramahi , S. Safavi-Naeini and S.K. Chaudhuri, "Design and Analysis of Ultra-Miniaturized Meandering Photonic Crystals Delay Lines", IEEE Trans. on Advanced Packaging, Volum31, No.2, May 2008, Page(s): 311 - 319.

2. **M. Fakharzadeh**, P. Mousavi , S. Safavi-Naeini, and S.H. Jamali "The Effects of Imbalanced Phase Shifters Loss on Phased Array Gain", IEEE Antennas and Wireless Propagation Lett., Volume 7, 2008, Page(s): 192-196.

3. **M. Fakharzadeh**, S. Safavi-Naeini, S.K. Chaudhuri, and O.M. Ramahi, "Miniaturized Photonic Crystal Delay Lines for Beamformnig of Phased Array Systems", Medit. J. on Electronics and communications, Volume 2, No. 4, October 2006.

4. P. Mousavi, **M. Fakharzadeh**, S.H. Jamali, K. Narimani, M. Hossu, H. Bolandhemmat, and S. Safavi-Naeini "A Low-Cost Low Profile Phased Array System for Mobile Satellite Reception Using Zero-Knowledge Beam-forming Algorithm", In press, IEEE Trans. Antennas and Propagation.

5. H. Bolandhemmat, **M. Fakharzadeh**, P. Mousavi, S. H. Jamali, and S. Safavi-Naeini, "Active Stabilization of Vehicle-Mounted Phased-Array Antennas", In press, IEEE Trans. Vehicular Technology.

6. **M. Fakharzadeh**, S. H. Jamali, P. Mousavi, and S. Safavi-Naeini "Fast Beamforming for Single Receiver Phased Arrays used in Mobile Satellite Communication ", Submitted to IEEE Trans. Antennas and Propagation.

Conference Papers

1. **M. Fakharzadeh**, O.M. Ramahi, S. Safavi-Naeini, S.K. Chaudhuri, "Application of the Reflective Spiral Photonic Crystal Delay Line in Beamforming for Phased Array Antennas", (Student Paper Contest Finalist), Proc. of the 2006 IEEE Int. Symp. Antennas Propagat., Albuquerque, NM, USA, Pages: 2279-2282.

2. **M. Fakharzadeh**, O.M. Ramahi, S. Safavi-Naeini, S.K. Chaudhuri, "Miniaturized Optical Delay Lines Using Photonic Crystals" (MTT Travel grant award) Proc. of IEEE Int. Microwave Symp. (IMS 2006), San Francisco, USA. Pages: 10-13.

3. **M. Fakharzadeh**, S. Safavi-Naeini and S.K. Chaudhuri, "Meandering Photonic Crystal Delay Lines", SPIE Photonic West 2007, San Jose, CA, USA.

4. **M. Fakharzadeh**, S. Safavi-Naeini, and Sujeet K. Chaudhuri, Optical Beamforming Network for Retro-directive Array Antennas, Proc. SPIE Vol. 7099, 70991E (Aug. 12, 2008), Pages 1-11.

5. **M. Fakharzadeh**, S. Safavi-Naeini, S.H. Jamali, P. Mousavi and K. Narimani "Accurate Limited Angle Tracking with a Phase Array Antenna Using Zero-Knowledge Beamforming", Proc. of 2007 IEEE Int. Symp. Antennas Propagat., Honolulu, HI, USA, Pages: 1104-1107.

6. **M. Fakharzadeh**, O. M. Ramahi, S. K. Chaudhuri and S. Safavi-Naeini, "A Photonic Crystal Delay Line with Two Time Delays ", Proc. of the 36th European Microwave Conference, Manchester, UK, Sep 10-13, 2006. Pages: 1383-1386.

7. **M. Fakharzadeh**, S.H. Jamali, S. Safavi-Naeini and P. Mousavi, "A Fast Calibration Algorithm for Phased Array Antennas Based on a Modified Perturbation Method", Proc. 2006 IEEE Int. Symp. Antennas Propagat., Albuquerque, NM, USA, Pages: 3343-3346.

8. **M. Fakharzadeh**, S.H. Jamali, S. Safavi-Naeini, P. Mousavi, and K. Narimani. "Fast Stochastic Beamforming for Mobile Phased Array Antennas", Proc. of 2007 IEEE Int. Symp. Antennas and Propagat., Honolulu, Hawaii, USA, Pages: 19451948.

9. **M. Fakharzadeh**, S. Safavi-Naeini, S.H. Jamali, P. Mousavi, "Zero-Knowledge Beamforming of Phased Array Antennas Based on Simultaneous Perturbation Gradient Approximation", Proc. of the 2006 IEEE Int. Symp. Antennas Propagat., Albuquerque, NM, USA, Pages: 537-540.

10. **M. Fakharzadeh**, S. Safavi-Naeini, S.K. Chaudhuri, "Miniaturized Optical Delay Lines," (Best Paper Award), ICUE 2006, University of Waterloo, May 13-14, 2006.

11. **M. Fakharzadeh**, S. Safavi-Naeini, "Using photonic bandgap materials to design wideband phased array antennas", Proc. of IST 2005 (International Symposium on Telecommunications), Vol. 1, Shiraz, Iran, Sep 10-12, 2005 pages: 417- 422.

12. **M. Fakharzadeh**, S.H. Jamali, K. Narimani, P. Mousavi and S. Safavi-Naeini, Zero-Knowledge Beamforming for Mobile Satellite Phased Array Antenna, presented in the 68th IEEE Vehicular Technology Conference (VTC 2008), Calgary, AB, Canada

13. **M. Fakharzadeh**, P. Mousavi , S. H. Jamali, and S. Safavi-Naeini, Compensation of the Imbalance Phase Shifter Loss Effects by Non-coherent Beamforming , Presented in the 2008 IEEE Int. Symp. Antennas Propagat., San Diego, CA, USA.

14. M. Hossu, S. H. Jamali, P. Mousavi, K. Narimani, **M. Fakharzadeh**, and S. Safavi-Naeini, Microwave Beamforming Using Analog Signal Processing, Presented in the 2008 IEEE Int. Symp. Antennas Propagat., San Diego, CA, USA.

15. **M. Fakharzadeh**, S.K. Chaudhuri, S. Safavi-Naeini, Optical Beamforming with Tunable Ring Resonators, Presented in the 2008 IEEE Int. Symp. Antennas Propagat., San Diego, CA, USA.

References

[1] F. Reggia, E.G. Spencer, R.D. Hatcher, and J.E. Tompkins, "Ferrod radiator system," *Proc. IRE*, vol. 45, no. 3, pp. 344–352, March 1957.

[2] W. V. Aulock, "Properties of phased arrays," *Proc. IRE*, vol. 48, no. 10, pp. 1715–1727, Oct. 1960.

[3] G. Kefalas, "A phased-array ground terminal for satellite communications," *IEEE Trans. Commun.*, vol. 13, no. 4, pp. 512–525, Dec. 1965.

[4] Soon Young Eom, *et. al*, "Design and test of a mobile antenna system with triband operation for broadband satellite communications and dbs reception," *IEEE Trans. Antennas Propagat.*, vol. 55, no. 11, pp. 3123–3133, Nov. 2007.

[5] J.C. Liberti, and T.S. Rappaport, "Analytical results for capacity improvements in cdma," *IEEE Trans. Veh. Technol.*, vol. 43, no. 3- Part 1-2, pp. 680–690, Aug. 1994.

[6] A.O. Boukalov, and S.-G. Haggman, "System aspects of smart-antenna technology in cellular wireless communications-an overview," *IEEE Trans. Microw. Theory Tech.*, vol. 48, no. 6, pp. 919–929, June 2000.

[7] R.K. Raney, A.P. Luscombe, E.J. Langham, and S. Ahmed, "Radarsat [sar imaging]," *Proc. of IEEE*, vol. 79, no. 6, pp. 839–849, June 1991.

[8] K.H. Lai, I.D. Longstaff and G.D. Callaghan, "Super-fast scanning technique for phased array weather radar applications," *IEE Proc. Radar, Sonar and Navigation*, vol. 151, no. 5, pp. 271–279, Oct. 2004.

[9] W.A.Coles, R.G. Frehlich, and M. Kojima, "Design of a 74-MHz antenna for radio astronomy," *Proc. of IEEE*, vol. 82, no. 5, pp. 697–704, May 1994.

[10] K. F. Molz, "The an/fps-85 satellite tracking phased array radar," *IEEE Trans. Aerospace*, vol. 2, no. 2, pp. 135–138, April 1964.

[11] Sergio Sabatini, and Marco Tarantino, *Multifunction Array Radar: System Design and Analysis*. Artech House Radar Library, 1994.

[12] C. Pell, "Phased-array radars," *IEE Review*, vol. 34, no. 9, pp. 363–367, Oct 1988.

[13] P. Mousavi, M. Fakharzadeh, S.H. Jamali, K. Narimani, M. Hossu, and H. Bolandhemmat, and G. Rafi, and S. Safavi-Naeini, "A low-cost ultra low profile phased array system for mobile satellite reception using Zero-knowledge beamforming algorithm," *IEEE Trans. Antennas Propagat.*, in Press.

[14] H. Bolandhemmat, M. Fakharzadeh, P. Mousavi, S. H. Jamali, and S. Safavi-Naeini, "Active stabilization of vehicle-mounted phased-array antennas," *IEEE Trans. Veh. Technol.*, in Press.

[15] P.J. Kahrilas, "Hapdaran operational phased array radar," *Proc. of IEEE*, vol. 56, no. 11, pp. 1967–1975, Nov. 1968.

[16] K. Ohata, et al., "Sixty-GHz-band ultra-miniature monolithic T/R modules for multimedia wireless communication systems," *IEEE Trans. Microw. Theory Tech.*, vol. 44, no. 12, pp. 2354–2360, Dec 1996.

[17] S. Reynolds, et al., "A silicon 60GHz receiver and transmitter chipset for broadband communications," vol. 41, no. 12, pp. 2820–2830, Dec 2006.

[18] Sten E. Gunnarsson, et. al, "60 GHz single-chip front-end MMICs and systems for multi-Gb/s wireless communication," vol. 42, no. 5, pp. 1143–1157, May 2007.

[19] T. Mitomo, et. al, "A 60-GHz CMOS receiver front-end with frequency synthesizer," vol. 43, no. 4, pp. 1030–1037, April 2008.

[20] A. Babakhani, et al., "A 77-GHz phased-array transceiver with on-chip antennas in silicon: Receiver and antennas," vol. 41, no. 12, pp. 2795–2806, Dec. 2006.

[21] B. Razavi, "Gadgets gab at 60 GHz," *IEEE Spectrum*, vol. 45, no. 2, pp. 46–58, Feb. 2008.

[22] P. Smulders, "Exploiting the 60 GHz band for local wireless multimedia access: prospects and future directions," *Communications Magazine, IEEE*, vol. 40, no. 1, pp. 140–147, Jan 2002.

[23] C. Park and T. Rappaport, "Short-range wireless communications for next-generation networks: UWB, 60 GHz millimeter-wave WPAN, and ZigBee," *IEEE Wireless Commun.*, vol. 14, no. 4, pp. 70–78, Aug. 2007.

[24] "Wirelesshd specification version 1.0 overview," 2007. [Online]. Available: http://www.wirelesshd.org/WirelessHD-Full-Overview-071009.pdf

[25] I. Immoreev, "Active transmitting phased antenna arrays," *IEEE Trans. Aerosp. Electron. Syst.*, vol. 41, no. 2, pp. 407–420, Apr. 2005.

[26] R. J. Mailloux, "Phased array theory and technology," *Proc. of IEEE*, vol. 70, no. 3, pp. 246–302, Mar. 1982.

[27] H. Hashemi, X. Guan, A. Komijani, and A. Hajimiri, "A 24-GHz SiGe Phased-Array ReceiverLO Phase-Shifting Approach," *IEEE Trans. Microw. Theory Tech.*, vol. 53, no. 2, pp. 614 – 626, 2005, feb.

[28] A. Hajimiri, H. Hashemi, A. Natarajan, X. Guan, and A. Komijani, "Integrated phased array systems in silicon," *pieee*, vol. 93, no. 9, pp. 1637–1655, Sept. 2005.

[29] B.C. Kane, L.A. Geis, M.A. Wyatt, D.G. Copeland, and J.A. Mogensen, "Smart phased array SoCs: A novel application for advanced SiGe HBT BiCMOS technology," *Proc. of IEEE*, vol. 93, no. 9, pp. 1656–1668, Sept. 2005.

[30] K.-J. Koh and G. Rebeiz, "An X- and Ku-band 8-element linear phased array receiver in 0.18-*muhboxm* SiGe BiCMOS technology," *IEEE J. Solid-State Circuits*, vol. 43, no. 6, pp. 1360–1371, June 2008.

[31] R. Sorace, "Phased array calibration," *IEEE Trans. Antennas Propagat.*, vol. 49, no. 48, pp. 517–525, Apr. 2001.

[32] M. Fakharzadeh, P. Mousavi, S. Safavi-Naeini, and S.H. Jamali, "The effects of imbalanced phase shifters loss on phased array gain," *IEEE Antenna Wireless Propagat. Lett.*, vol. 7, pp. 192–196, 2008.

[33] I. Frigyes and A. Seeds, "Optically generated true-time delay in phased-array antennas," *IEEE Trans. Microw. Theory Tech.*, vol. 43, no. 9, pp. 2378–2386, Sept 1995.

[34] H. Zmuda and E. N. Toughlian, *Photonic Aspects of Modern Radar*. Artech House, 1994.

[35] A. Kumar, *Antenna Design with Fiber Optics*. Artech House, 1996.

[36] Y. Bresler, V. Reddy, and T. Kailath, "Optimum beamforming for coherent signal and interferences," *IEEE Trans. Signal Process.*, vol. 36, no. 6, pp. 833–843, June 1988.

[37] R. Miura, T. Tanaka, I. Chiba, A. Horie, and Y. Karasawa, "Beamforming experiment with a dbf multibeam antenna in a mobile satellite environment," *IEEE Trans. Antennas Propagat.*, vol. 45, no. 4, pp. 707–714, Apr 1997.

[38] L. Godara and A. Cantoni, "Analysis of constrained LMS algorithm with application to adaptive beamforming using perturbation sequences," *IEEE Trans. Antennas Propagat.*, vol. 34, no. 3, pp. 368–379, Mar. 1986.

[39] L. C. Godara, "Application of antenna arrays to mobile communications, part II: beam-forming and direction of arrival considerations," *Proc. of IEEE*, vol. 85, no. 8, pp. 1195–1254, Aug. 1997.

[40] B. Carlson, "Covariance matrix estimation errors and diagonal loading in adaptive arrays," *IEEE Trans. Aerosp. Electron. Syst.*, vol. 24, no. 4, pp. 397–401, Jul. 1988.

[41] I. M. B.G. Wahlberg and I. Webster, "Experimental and theoretical comparison of some algorithms for beamforming in single receiver adaptive arrays," *IEEE Trans. Antennas Propagat.*, vol. 39, no. 1, pp. 21–28, 1991.

[42] D. Feldman and L. Griffiths, "A projection approach for robust adaptive beamforming," *IEEE Trans. Signal Process.*, vol. 42, no. 4, pp. 867–876, Apr. 1994.

[43] R. O. Schmidt, "Multiple emitter location and signal parameters estimation," *IEEE Trans. Antennas Propagat.*, vol. 34, no. 3, pp. 276–280, Mar. 1986.

[44] R. Roy and T. Kailath, "ESPRIT - Estimation of signal parameters via rotational invariance techniques," *IEEE Trans. Acoust., Speech, Signal Processing*, vol. 37, no. 7, pp. 984–995, July 19899.

[45] A. Swindlehurst and T. Kailath, "A performance analysis of subspace-based methods in the presence of model errors: Part 1-The MUSIC algorithm," *IEEE Trans. Signal Process.*, vol. 40, no. 7, pp. 1758–1774, July 1992.

[46] ——, "A performance analysis of subspace-based methods in the presence of model errors: Part II-Multidimensional algorithms," *IEEE Trans. Signal Process.*, vol. 41, no. 9, pp. 2882–2890, Sept. 1993.

[47] M. Fakharzadeh, S. Safavi-Naeini, S.H. Jamali and P. Mousavi, "Zero-knowledge beamforming of phased array antennas based on simultaneous perturbation gradient approximation ," in *IEEE Int. Symp. Antennas Propagat.*, Albuquerque, NM, July 2006, pp. 537–540.

[48] M. Fakharzadeh, S.H. Jamali, S. Safavi-Naeini, P. Mousavi, "A fast calibration algorithm for phased array antennas based on a modified perturbation method," in *IEEE Int. Symp. Antennas Propagat.*, Albuquerque, NM, July 2006, pp. 3343–3346.

[49] M. Fakharzadeh, S.H. Jamali, K. Narimani, P. Mousavi and S. Safavi-Naeini, "Zero-Knowledge Beamforming for Mobile Satellite Phased Array Antenna," in *68th IEEE Veh. Technol. Conf. (VTC 2008)*, Calgary, AB, Canada, Sept. 2008.

[50] S. Hayward, "Effects of motion on adaptive arrays," *IEE Proc. Radar, Sonar Navig.*, vol. 144, no. 1, pp. 15–20, Feb. 1997.

[51] P.V. Brennan, "Low cost phased array antenna for land-mobile satcom applications," *IEE Proceedings-H*, vol. 138, no. 2, pp. 131–136, Apr. 1991.

[52] J.I. Alonso, *et. al*, "Low cost electronically steered antenna and receiver system for mobile satellite communications," *IEEE Trans. Microw. Theory Tech.*, vol. 44, no. 12, pp. 2438–2449, 1996.

[53] J.B.L. Rao, and G.V. Trunk, and D.P. Patel, "Two low-cost phased arrays," *IEEE Trans. Aero. Electron. Sys.*, vol. 12, no. 6, pp. 39–44, Jun 1997.

[54] S. Denno and T. Ohira, "Modified constant modulus algorithm for digital signal processing adaptive antennas with microwave analog beamforming," *Antennas and Propagation, IEEE Transactions on*, vol. 50, no. 6, pp. 850–857, Jun. 2002.

[55] T. O. Chen Sun, Akifumi Hirata and N. C. Karmakar, "Fast beamforming of electronically steerable parasitic array radiator antennas: theory and experiment," *IEEE Trans. Antennas Propagat.*, vol. 52, no. 7, pp. 1819–1832, Jul. 2004.

[56] B. W. D. G. C.T.P. Song, A. Mak and R. D. Murch, "Compact low cost dual polarized adaptive planar phased array for wlan," *IEEE Trans. Antennas Propagat.*, vol. 53, no. 8, pp. 2406–2416, Aug. 2005.

[57] Robert J. Mailloux, *Phased Array Antenna Handbook- Chapter 1*, 2nd ed. Artech House, 2005.

[58] Robert E. Collin, *Antennas and Radiowave Propagation.* McGraw-Hill, 1985.

[59] S. Raman, N. Barker, and G. Rebeiz, "A w-band dielectric-lens-based integrated monopulse radar receiver," *IEEE Trans. Microw. Theory Tech.*, vol. 46, no. 12, pp. 2308–2316, Dec. 1998.

[60] M. Fakharzadeh, M.R. Nezhad-Ahmadi, B. Biglarbegian, J. Ahmadi-Shokouh, H. Mirzaei, and S. Safavi-Naeini, "CMOS Phased Array Transceiver Technology for 60GHz Wireless ApplicationsSystem Analysis," *Submitted to IEEE Trans. Antennas and Propagat.*, July 2008.

[61] J.-H. Lee and K.-P. Cheng, "Adaptive Array Beamforming with Robust Capabilities Under Random Phase Perturbations," *IEEE Trans. Signal Process.*, vol. 53, no. 1, pp. 365–371, Jan. 2005.

[62] A. Bhattacharyya, *Phased array antenna: Floquet Analysis, Synthesis, BFNs and Active Array Systemss.* Wiley, 2006.

[63] B. Widrow and J. McCool, "A comparison of adaptive algorithms based on the methods of steepest descent and random search ," *IEEE Trans. Antennas Propagat.*, vol. 24, no. 5, pp. 615 – 637, Sept. 1976.

[64] S. Haykin and B. Widrow, *Least-mean-square Adaptive Filters.* Wiley-IEEE, 2003.

[65] J. D. C. M. M. M. Morton, J. P. Comeau and J. Papapolymerou, "Sources of Phase Error and Design Considerations for Silicon-Based Monolithic High-Pass/Low-Pass Microwave Phase Shifters," *IEEE Trans. Microw. Theory Tech.*, vol. 54, no. 12, pp. 4032–4040, Dec. 2006.

[66] S. Alalusi and R. Brodersen, "A 60GHz Phased Array in CMOS," in *Proc. of the 2006 IEEE Custom Integrated Circuits Conf.*, Sept. 2006, pp. 393–396.

[67] Byung-Wook Min, and Gabriel M. Rebeiz, "Ka-Band BiCMOS 4-Bit Phase Shifter with Integrated LNA for Phased Array T/R Modules," in *IEEE/MTT-S Int. Microwave Symp.*, June 2007, pp. 479–482.

[68] R. V. Garver, "Broad-band diode phase shifters," *IEEE Trans. Microw. Theory Tech.*, vol. 20, no. 5, pp. 314–323, May 1972.

[69] J.J. LEE, "G/T and Noise Figure of Active Array Antennas," *IEEE Trans. Antennas Propagat.*, vol. 41, no. 2, pp. 241–244, Feb. 1993.

[70] Y. U. H. Hayashi, M. Muraguchi and T. Enoki, "A High-Q Broad-Band Active Inductor and Its Application to a Low-Loss Analog Phase Shifter," *IEEE Trans. Microw. Theory Tech.*, vol. 44, no. 12, pp. 2369–2374, Dec. 1996.

[71] J.A. Higgins, H. Xin, A. Sailer, and M. Rosker, "Ka-Band Waveguide Phase Shifter Using Tunable Electromagnetic Crystal Sidewalls," *IEEE Trans. Microw. Theory Tech.*, vol. 51, no. 4, pp. 1281–1288, Apr. 2003.

[72] J. A. T. Ji, H. Yoon and V. Varada, "Ku-Band Antenna Array Feed Distribution Network With Ferroelectric Phase Shifters on Silicon," *IEEE Trans. Microw. Theory Tech.*, vol. 54, no. 3, pp. 1131–1138, Mar. 2006.

[73] A. Nagra and R. York, "Distributed Analog Phase Shifters with Low Insertion Loss," *IEEE Trans. Microw. Theory Tech.*, vol. 47, no. 9, pp. 1705–1711, Sept. 1999.

[74] H. Hayashi, T. Nakagawa, and K. Araki, "A Miniaturized MMIC Analog Phase Shifter Using Two Quarter-Wave-Length Transmission Lines," *IEEE Trans. Microw. Theory Tech.*, vol. 50, no. 1, pp. 150–154, Jan. 2002.

[75] L.-H. Lu and Y.-T. Liao, "A 4-GHz Phase Shifter MMIC in 0.18-μm CMOS," *IEEE MWL*, vol. 15, pp. 694–696, Oct. 2005.

[76] R.C. Johnson, and H. Jasik, *Antenna Engineering Handbook*. McGraw-Hill, 1993.

[77] M. Fakharzadeh, S.H. Jamali, P. Mousavi, and S. Safavi-Naeini, "Imbalance phase shifter loss compensation by non-coherent beamforming," in *IEEE Int. Symp. Antennas Propagat.*, San Diego, CA, July 2008.

[78] Rodney S. Tucker, Pei-Cheng Ku, and Constance J. Chang-Hasnain, "Slow-light optical buffers: capabilities and fundamental limitations," *J. Lightw. Technol.*, vol. 23, no. 12, pp. 4046–4066, Dec. 2005.

[79] J. Capmany, J. Cascon, J.L. Martin, S. Sales, D. Pastor, and J. Marti, "Synthesis of fiber-optic delay line filters," *J. Lightw. Technol.*, vol. 13, no. 10, pp. 2003–2012, Oct. 1995.

[80] R. A. Minasian, "Photonic signal processing of microwave signals," *IEEE Trans. Microw. Theory Tech.*, vol. 54, no. 2, pp. 832–846, Feb. 2006, part 2.

[81] J.E. Bowers, S.A. Newton, and H.J. Shaw, "Fibre-optic variable delay lines," *Electron. Lett.*, vol. 18, no. 23, pp. 999–1000, Nov. 1982.

[82] Gary A. Ball, W.H. Glenn, and W.W. Morey, "Programmable fiber optic delay line," vol. 6, no. 6, pp. 741–743, June 1994.

[83] J. S. H.R. Rideout and J. Yao, "A True Time Delay Beamforming System Incorporating a Wavelength Tunable Optical Phase-Lock Loop," *J. Lightw. Technol.*, vol. 25, no. 7, pp. 1761–1770, July 2007.

[84] A. Yariv, Y. Xu, R. K. Lee, and A. Scherer, "Coupled resonator optical waveguides a proposal and analysis," *Optics Lett.*, vol. 24, no. 11, pp. 711–713, June 1999.

[85] D. W. C. Chang, D. Altman and D. Albares, "Noncoherent radar moving target indicator using fiber optic delay lines," *IEEE Trans. Circuits Syst.*, vol. 26, pp. 1132 – 1135, 1979.

[86] B. Ortega, J. Cruz, J. Capmany, M. Andres, and D. Pastor, "Analysis of a microwave time delay line based on a perturbed uniform fiber Bragg grating operating at constant wavelength," *J. Lightw. Technol.*, vol. 18, pp. 430–436, 2000.

[87] W. Ng, A. A. Watson, G. L. Tangonan, J. J. Lee, and I. L. Newberg, "The first demonstration of an optically steered phased array antenna using true-time-delay," *IEEE J. Lightwave Tech.*, vol. 9, no. 9, pp. 1124–1131, 1991.

[88] M. Fakharzadeh, S. Safavi-Naeini, S.K. Chaudhuri and O.M. Ramahi, "Miniaturized Photonic Crystal Delay Lines for Beamformnig of Phased Array Systems," *Medit. J. on Electronics and communications*, vol. 2, no. 4, Oct. 2006.

[89] S. Nishikawa, S. Lan, N. Ikeda, Y. Sugimoto, H. Ishikawa, and K. Asakawa, "Optical characterization of photonic crystal delay lines based on one-dimensional coupled defects," *Optics Lett.*, vol. 27, pp. 2079–2081, 2002.

[90] J. M. Lourtioz, *Photonic Crystals Towards Nanoscale Photonic Devices*. Springer, 2005.

[91] Y. Jiang, B. Howley, Z. Shi, Q. Zhou, R. Chen, M. Chen, G. Brost, and C. Lee, "Dispersion-enhanced photonic crystal fiber array for a true time delay structured X-Band phased array antenna," vol. 17, pp. 187–189, 2005.

[92] Z. Wang and S. Fan, "Dispersion characteristics of coupled-resonator optical waveguides," *Optics Lett.*, vol. 30, no. 18, pp. 2406–2408, September 2005.

[93] S. Lan, S. Nishikawa, and O. Wada, "Design of impurity band-based photonic crystal waveguides and delay lines for ultrashort optical pulses," *J. Appl. Phys.*, vol. 90, pp. 4321–4327, 2001.

[94] J. Liu, B. Shi, D. Zhao, and X. Wang, "Optical delay in defective photonic bandgap structures," *J. Opt. A: Pure Appl. Opt.*, vol. 4, pp. 636–639, 2002.

[95] M.L. Povinelli, S.G. Johnson, and J.D. Joannopoulos, "Slow-light, band-edge waveguides for tunable time delays," *Optics Express*, vol. 13, no. 18, pp. 7145–7159, Sept. 2005.

[96] M. Fakharzadeh, O.M. Ramahi, S.K. Chaudhuri, and S. Safavi-Naeini, "A photonic crystal delay line with two time delays," in *Proc. 36th European Microwave Conf.*, Manchester, UK, Sept. 2006, pp. 1383 – 1386.

[97] M. Fakharzadeh, O. Ramahi, S. Chaudhuri, and S. Safavi-Naeini,, "Miniaturized optical delay lines using photonic crystals," in *Proc.IEEE Int. Microw. Symp.*, San Francisco, CA, USA, June 2006, pp. 10–13.

[98] M. Fakharzadeh, O. M. Ramahi, S. Safavi, and S.K. Chaudhuri, "Design and analysis of ultra-miniaturized meandering photonic crystals delay lines," *IEEE Trans. Adv. Packag.*, vol. 31, no. 2, pp. 311–319, May 2008.

[99] M. Fakharzadeh, O.M. Ramahi, S. Safavi-Naeini, and S.K. Chaudhuri, "Application of the Reflective Spiral photonic crystal delay line in beamforming for phased array antennas ," in *IEEE Int. Symp. Antennas Propagat.*, Albuquerque, NM, July 2006, pp. 2279–2282.

[100] A. Melloni, F. Morichetti, F. Persia, C. Canavesi, R. Siano, and M. Martinelli, "Optical processing with slow wave structures: Properties and applications," *2006 International Conference on Transparent Optical Networks*, vol. 2, pp. 199–202, 2006.

[101] P. Matthews, M. Frankel, and R. Esman, "A wide-band fiber-optic true-time-steered array receiver capable of multiple independent simultaneous beams," vol. 10, pp. 722–724, May 1998.

[102] M.S. Rasras, and *et. al* , "Integrated resonance-enhanced variable optical delay lines," *IEEE Photonics Tech. Lett.*, vol. 17, pp. 834–836, 2005.

[103] e. L. Zhuang, "Phased array receive antenna steering system using a ring resonator-based optical beamforming network and filter-based optical SSB-SC modulation," in *IEEE Microwave Photonics*, Oct. 2007, pp. 88–91.

[104] Y. Y. Shunichi Yamagata and Y. Kokubun, "Wide-range tunable microring resonator filter by thermo-Optic effect in polymer waveguideupled," *Japanese J. Appl. Phys.*, vol. 43, no. 8B, pp. 5766–5770, 2004.

[105] I. Kobayashi and K. Kuroda, "Step-type optical delay line using silica-based planar light-wave circuit (PLC) technology," *IEEE Trans. Inst. Meaus.*, vol. 49, no. 4, pp. 762–765, Aug. 2000.

[106] J. M. Lourtioz, *Photonic Crystals Towards Nanoscale Photonic Devices*. Springer, 2005.

[107] S.G. Johnson, P.R. Villeneuve, S. Fan, and J.D. Joannopoulos, "Linear waveguides in photonic-crystal slabs," *Phys. Rev.B*, vol. 62, no. 12, pp. 8212 – 8222, Sept. 2000.

[108] A. Mekis, J. C. Chen, S. Fan, P. R. Villeneuve, and J. D. Joannopoulos, "High transmission through sharp bends in photonic crystal waveguides," *Phys. Rev. Lett.*, vol. 77, no. 18, pp. 3787–3790, Oct 1996.

[109] J.D. Joannopoulos, R.D. Meade, and J.N. Winn, *Photonic crystals: molding the flow of light*. Princeton University Press, 1995.

[110] Z. Wang, and S. Fan, "Optical circulators in two-dimensional magneto-optical photonic crystals," *Optic. Lett.*, vol. 30, pp. 1989–1991, 2005.

[111] D. Smith, R. Dalichaouch, N. Kroll, S. Schultz, S. McCall, and P. Platzman, "Photonic band structure and defects in one and two dimensions," *JOSAB*, vol. 10, pp. 314–321, 1993.

[112] S. Fan, J. Winn, A. D. J. Chen, R. Meade, and J. Joannopoulos,, "Guided and Defect Modes in Periodic Dielectric Waveguides," *JOSAB*, vol. 12, pp. 1267 – 1272, 1995.

[113] J. Poon, J. Scheuer, Y. Xu, and A. Yariv,, "Designing coupled-resonator optical waveguide delay lines," *JOSAB*, vol. 21, pp. 1665–1673, 2004.

[114] C. Madsen and J. Zhao, *Optical Filter Design and Analysis: A Signal Processing Approach*. New York: Wiley, 1999.

[115] J. Poon, J. Scheuer, S. Mookherjea, G. Paloczi, Y. Huang, and A. Yariv, "Matrix analysis of microring coupled-resonator optical waveguides," *Optics Express*, vol. 12, pp. 90–103, 2004.

[116] P. R. R. C. G. Cusmai, F. Morichetti and A. Melloni, "Circuit-oriented modelling of ring-resonators," *Optical and Quantum Electronics*, vol. 37, pp. 343–358, 2005.

[117] A. Taflove and S. C. Hagness, *Computational Electrodynamics: The Finite-difference Time-domain Method*. Artech House, 2000.

[118] O. Schwelb, "Transmission, Group Delay, and Dispersion in Single-Ring Optical Resonators and Add/Drop Filters - A Tutorial Overview," *J. Lightw. Technol.*, vol. 22, no. 5, pp. 1380–1394, May 2004.

[119] H. H. J. F. B.E. Little, S.T. Chu and J.-P. Laine, "Microring resonator channel dropping filters," *J. Lightw. Technol.*, vol. 15, no. 6, pp. 998–1005, March 1997.

[120] J. Poon, L. Zhu, G. DeRose, and A. Yariv, "Polymer microring coupled-resonator optical waveguides," *J. Lightw. Technol.*, vol. 24, pp. 1843–1849, 2006.

[121] V. . Van, "Circuit-based method for synthesizing serially coupled microring filters," *J. Lightw. Technol.*, vol. 24, pp. 2912–2919, July 2006.

[122] R. T. R. Orta, P. Savi and D. Trinchero, "Synthesis of multiple-ring-resonator filters for optical systems," *IEEE Photonics Technology Letters*, vol. 7, pp. 1447–1449, Dec. 1995.

[123] T. Kato and Y. Kokubun, "Optimum coupling coefficients in second-order series-coupled ring resonator for nonblocking wavelength channel switch," *J. Lightw. Technol.*, vol. 24, pp. 991–999, 2006.

[124] M. Fakharzadeh, S.H. Jamali, P. Mousavi, and S. Safavi-Naeini, "Fast beamforming for single receiver phased arrays used in mobile satellite communications," *Submitted to IEEE Trans. Antenna Propagat.*, June 2008.

[125] M. Fakharzadeh, S. Safavi-Naeini, S.H. Jamali, P. Mousavi, and K. Narimani, "Accurate limited angle tracking with a phase array antenna using zero-knowledge beamforming," in *IEEE Int. Symp. Antennas Propagat.*, Honolulu, HI, June 2007, pp. 1104–1107.

[126] M. Fakharzadeh, S.K. Chaudhuri, and S. Safavi-Naeini, "Optical beamforming with tunable ring resonators," in *IEEE Int. Symp. Antennas Propagat.*, San Diego, CA, July 2008.

[127] M. Fakharzadeh, S. Safavi-Naeini, and Sujeet K. Chaudhuri, "Optical beamforming network for retro-directive array antennas," *Proc. SPIE*, vol. 7099, pp. 70 991E, 1–11, Aug. 2008.

[128] R. Davis, "Phase-only LMS and perturbation adaptive algorithms," *IEEE Trans. Aero. Electron. Sys.*, vol. 34, no. 1, pp. 169–178, 1998.

[129] A. Cantoni, "Application of orthogonal perturbation sequences to adaptive beamforming," *IEEE Trans. Antennas Propagat.*, vol. 28, no. 2, pp. 191–202, 1980.

[130] L. Godara, "Improved LMS Algorithm for Adaptive Beamforming," *IEEE Trans. Antennas Propagat.*, vol. 38, no. 10, pp. 1631–1635, Oct. 1990.

[131] S. Haykin, *Adaptive Filter Theory*, 4th ed. Prentice Hall, 2002.

[132] J. C. Spall, "Implementation of the simultaneous perturbation algorithm for stochastic optimization," *IEEE Trans. Aerosp. Electron. Syst.*, vol. 34, no. 3, pp. 817–823, Jul. 1998.

[133] M. Fakharzadeh, S.H. Jamali, P. Mousavi, K. Narimani, and S. Safavi-Naeini, "Fast stochastic beamforming for mobile phased array antennas," in *IEEE Int. Symp. Antennas Propagat.*, Honolulu, HI, June 2007, pp. 1945–1948.

[134] Alan V. Oppenheim, Ronald W. Schafer, and John R. Buck, *Discrete-time signal processing*, 2nd ed. Prentice-Hall, 1999.

[135] A. C. Densmore and V. Jamnejad, "A satellite-tracking k- and ka-band mobile vehicle antenna system," *IEEE Trans. Veh. Technol.*, vol. 42, no. 4, pp. 502–513, Nov 1993.

[136] M. A. J. Hirokawa and N. Goto, "A single layer slotted leaky waveguide array antenna for mobile reception of direct broadcast from satellite," *IEEE Trans. Veh. Technol.*, vol. 44, no. 4, pp. 749–755, Nov 1995.

[137] C. Knapp and G. Carter, "The generalized correlation method for estimation of time delay," *IEEE Trans. Acoustics, Speech, and Signal Process.*, vol. 24, pp. 320–327, 1976.

[138] N. K. Go Sekiguchi and Y. Kokubun, "Coupling efficiency control of vertically coupled microring resonator filter by microactuator," vol. 18, no. 20, pp. 2141–2143, Oct. 15 2006.

[139] P.S. Hall, *Book Chapter: Review of techniques for dual and circularly polarized microstrip antenna*, D. M. Pozar, and D. H. Schaubert, Ed. IEEE Press, 1995, in Microstrip Antennas: The Analysis and Design of Microstrip Antennas and Arrays.

[140] R. J. Vanderbei, "Loqo user's manual-version 4.05," *Princeton University*, 2008. [Online]. Available: http://www.princeton.edu/ rvdb/tex/loqo/ loqo405.pdf

[141] David M. Pozar, *Microwave Engineering*, 3rd ed. Wiley, 2005.

[142] C. Loo, "A statistical model for a land mobile satellite link," *IEEE Trans. Veh. Technol.*, vol. 34, no. 1, pp. 122–127, 1985.

[143] G. Corazza and F. Vatalaro, "A statistical-model for land mobile satellite channels and its application to non-geostationary orbit system," *IEEE Trans. Veh. Technol.*, vol. 34, no. x, pp. 738–742, 1994.

[144] A. Abdi, *et al.*, "A new simple model for land mobile satellite channels: first- and second-order statistics," *IEEE Trans. Wireless Commun.*, vol. 2, no. x, pp. 519–528, May 2003.

[145] E. Lutz, D. Cygan, M. Dippold, F. Dolainsky, and W. Papke, "The land mobile satellite communication channel-recording, statistics and channel model," *IEEE Trans. Veh. Technol.*, vol. 40, no. 2, pp. 375–386, May 1991.

[146] G. Butt, "Narrowband channel statistics from multiband propagation measurements applicable to high elevation angle land-mobile satellite systems," *IEEE J. Select. Areas Commun.*, vol. 10, no. 8, pp. 1219–1226, Oct. 1992.

[147] B. Vucetic and J. Du, "Channel Modeling and Simulation in Satellite Mobile Communication Systems," *IEEE J. Select. Areas Commun.*, vol. 10, no. 8, pp. 1209–1218, Oct. 1992.

[148] C. Oestges and D. Vanhoenacker-Janvier, "Propagation modeling and system strategies in Mobile-Satellite Urban Scenarios," *IEEE Trans. Veh. Technol.*, vol. 50, no. 2, pp. 422–429, Mar. 2001.

[149] A. Zaghloul, Y. Hwang, R. Sorbello, and F. Assal, "Advances in multibeam communications satellite antennas," *Proc. of IEEE*, vol. 78, no. 7, pp. 1214–1232, July 1990.

[150] Y. Hwang, "Satellite antennas," *Proc. of IEEE*, vol. 80, no. 1, pp. 183–193, Jan. 1992.

[151] "List of satellites in geosynchronous orbit," *Wikipedia*, Jan. 2008. [Online]. Available: http://en.wikipedia.org/wiki/List-of-satellites-in-geosynchronous-orbit

[152] M. Richharia, *Satellite Communication Systems*, 2nd ed. New York : McGraw-Hill, 1999.

[153] D. Tse, and P. Viswanath, *Fundamentals of Wireless Communication.* Cambridge University Press, 2005.

[154] E. Semouchkina, W. Cao, and R. Mittra, "Modeling of microwave ring resonators using the finite-difference time-domain method (fdtd)," *Microwave and Optical Technology Letters*, vol. 24, pp. 392–396, 2000.